STUDY OF THE PHYSICS OF DROPLET IMPINGEMENT COOLING

A Dissertation

by

GUILLERMO ENRIQUE SORIANO

Submitted to the Office of Graduate Studies of
Texas A&M University
in partial fulfillment of the requirements for the degree of

DOCTOR OF PHILOSOPHY

May 2011

Major Subject: Mechanical Engineering

STUDY OF THE PHYSICS OF
DROPLET IMPINGEMENT COOLING

A Dissertation

by

GUILLERMO ENRIQUE SORIANO

Submitted to the Office of Graduate Studies of
Texas A&M University
in partial fulfillment of the requirements for the degree of

DOCTOR OF PHILOSOPHY

Approved by:

Chair of Committee,	Jorge Alvarado
Committee Members,	Yassin A. Hassan
	Debjyoti Banerjee
	Sai Lau
Head of Department,	Dennis O'Neal

May 2011

Major Subject: Mechanical Engineering

ABSTRACT

Study of the Physics of
Droplet Impingement Cooling. (May 2011)
Guillermo Enrique Soriano, B.S., Escuela Superior Politecnica del Litoral;
M.S., Georgia Institute of Technology
Chair of Advisory Committee: Dr. Jorge Alvarado

Spray cooling is one of the most promising technologies in applications which require large heat removal capacity in very small areas. Previous experimental studies have suggested that one of the main mechanisms of heat removal in spray cooling is forced convection with strong mixing due to droplet impingement. These mechanisms have not been completely understood mainly due to the large number of physical variables, and the inability to modulate and control variables such as droplet frequency and droplet size. Our approach consists of minimizing the number of experimental variables by controlling variables such as droplet direction, velocity and diameter.

A study of heat transfer for single and multiple droplet impingements using HFE-7100 as the cooling fluid under constant heat flux conditions is presented. Monosized single and multiple droplet trains were produced using a piezoelectric droplet generator with the ability to adjust droplet frequency, diameter, velocity, and spacing between adjacent droplets. In this study, heaters consisting of a layer of Indium Tin Oxide (ITO) as heating element, and ZnSe substrates were used. Surface temperature at the liquid-solid interface was measured using Infrared Thermography. Heat transfer behavior was characterized and critical heat flux was measured. Film thickness was measured using a non-invasive optical technique inside the crown formation

produced by the impinging droplets. Hydrodynamic phenomena at the droplet impact zone was studied using high speed imaging. Impact regimes of the impinging droplets were identified, and their effect on heat transfer performance were discussed. The results and effects of droplet frequency, droplet diameter, droplet velocity, and fluid flow rate on heat flux behavior, critical heat flux, and film morphology were elucidated.

The study showed that forced heat convection is the main heat transfer mechanism inside the crown formation formed by droplet impingement and impact regimes play an important role on heat transfer behavior. In addition, this study found that spacing among adjacent droplets is the most important factor for multiple droplet stream heat transfer behavior. The knowledge generated through the study provides tools and know-how necessary for the design and development of enhanced spray cooling systems.

NOMENCLATURE

A	Area
d	Diameter
D	Digital count infrared camera
$Dens$	Density
f	Frequency
h	Heat transfer coefficient
h_{fg}	Latent heat of vaporization
I	Current
k	Thermal conductivity
L	Distance between droplets
$\dot{m}''$	Mass flux rate
n	Refractive index
Nu	Nusselt number $((hd)/k_f)$
Oh	Ohnesorge number $(\mu/\sqrt{\rho\sigma d})$
P	Power
q	Heat
q''	Heat flux
q''_c	Critical heat flux
Q''	Volumetric flow rate
Re	Reynolds number $((\rho v d)/\mu)$
s	Droplet spacing
S	Jet spacing
St	Strouhal number $((fd)/v)$

t	Liquid film thickness
T	Temperature
u	Uncertainty
V	Voltage
v	Velocity
W	Irradiance
We	Weber number $((\rho v^2 d)/\sigma)$
β	Droplet spreading ratio
σ	Surface tension
α	Absorptivity
ε	Emissivity
$\underline{\rho}$	Reflectivity
μ	Dynamic viscosity
ρ	Density
θ	Critical angle
τ	Transmissivity

Subscripts:

avg	Average
atm	Atmosphere
c	Impact zone crown
d	Droplet
diff	Difference
eq	Equivalent
htr	Heater
in	Input
j	Jet
l	Liquid
loss	Losses
ref	Reference
o	Initial
obj	Object
s	Solid
sub	Substrate
surr	Surroundings
tot	Total
v	vapor

TABLE OF CONTENTS

CHAPTER Page

LIST OF TABLES

LIST OF FIGURES

FIGURE Page

FIGURE Page

FIGURE Page

CHAPTER I

INTRODUCTION

The goal of this project is to gain a better understanding of the physics of heat transfer due to droplet impingement on a surface when subject to constant heat flux at the solid-liquid interface. Understanding the effect of droplet impingement on heated surfaces apply to applications such as spray cooling which is routinely used in miniaturized packaging electronic systems in which the power dissipation demands require a direct liquid methodology.

The knowledge generated through the study will be used to understand the effect of droplet impingement on spray cooling phenomena. The experimental results and analysis will help in the design of better spray and droplet cooling systems.

A. Motivation

Thermal management of electronic equipment remains one of the most enduring technical challenges of the world today [1]. Modern electronic packages are complex systems which exhibit multifunctionality, miniaturization, and make use of modern materials which result in high thermal loads. Moreover, the intricate configuration of electronic packages leads to highly concentrated and non-uniform thermal loads from sources such as microprocessors, and memory devices.

In the last three decades, consumer have been demanding fast and reliable electronic systems and components which have put considerably pressure on the way electronics systems should be designed and fabricated. Moore [2] predicted an ex-

---

The journal model is *IEEE Transactions on Components and Packaging Technologies*.

ponential increase in the number of transistors that could be packaged on a die as could be seen on Figure 1. The ability of the electronic industry to comply with Moore's prediction alongside with die size reduction have created thermal challenges that still need to be solved. The International Technology Roadmap for Semiconductors ($ITRS - 2009$) predicts a dissipation of $260W/cm^2$ from electronic packages by 2011 [3] including digital packages such as microprocessors but also on radiofrequency (RF), optoelectronics and microelectromechanical (MEMS) modules. ITRS also projected a maximum junction temperature of 100 ℃ in high-performance and cost effective devices; 125 ℃ in low-cost, handheld devices; and 175 ℃ in devices working in harsh environments in order to comply with performance and reliability needs.

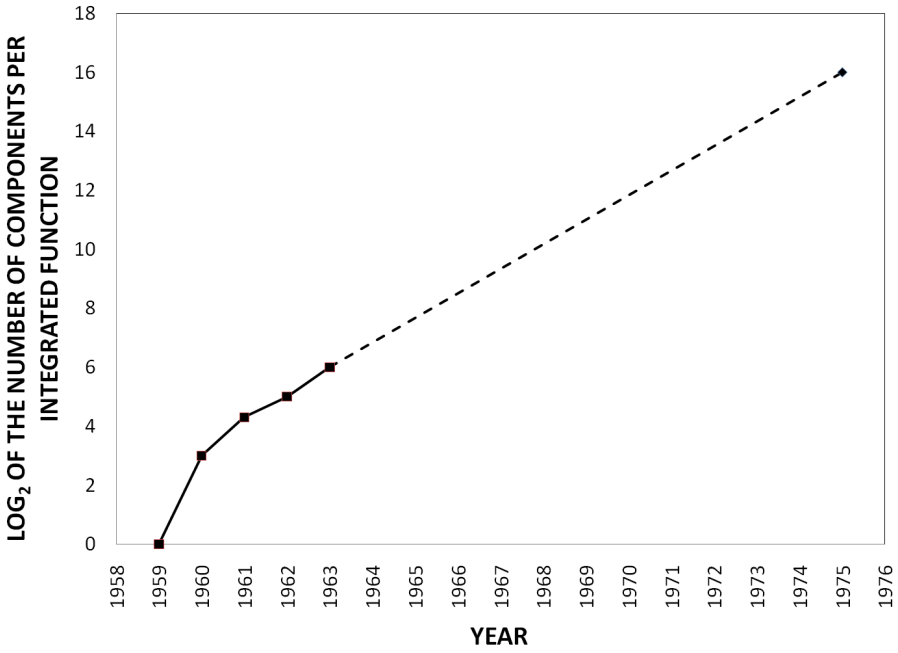

Fig. 1.: Transistor count as a function of year from [2]

Selection of thermal management technologies used on these future electronic modules are key to their proper functioning. Thermal management systems are expected to dissipate thermal loads as high as $1,000\ W/cm^2$ for some of these electronic packaging systems. Passive systems such as heat spreaders, extended surfaces and heat pipes relying on natural or forced convection of air are able to handle heat flux values to only approximately 5 to 20 W/cm^2 making them inadequate for these applications (see Figure 2).

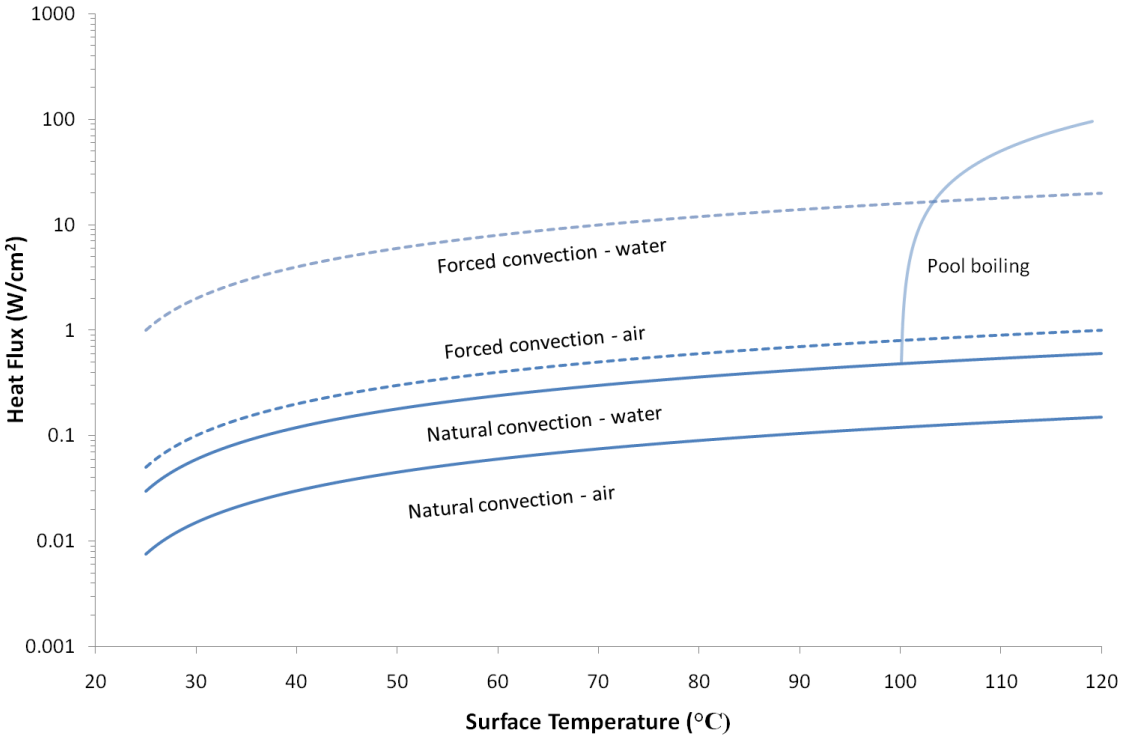

Fig. 2.: Comparison of common cooling techniques

From Figure 2, it is evident that active systems involving a phase change process are clear alternatives to manage the required thermal loads. Among the options

to achieve higher heat flux rates which are currently subject of active research, we include: spray cooling, jet cooling, single and multipledroplet cooling, vapor compression refrigeration, and thermosyphons. All of these options can achieve heat fluxes several times higher than saturated pool boiling. However, the physical mechanisms of these thermal management techniques are still not well understood due to the vast number of physical variables that should be considered.

B. Objectives

Despite of the attractive features of spray cooling, there has been a debate about the uniformity of heat removal and surface temperature distribution on spray and droplet cooling. Moreover, there have been a number of studies with conflicting findings that have made the study of spray cooling even harder. Very little research has been done on the spatial and temporal evolution of thin liquid film which is formed when droplets impinged a heat surface. Additionally, only low resolution localized heat transfer and surface temperature data have been reported to date. There is a need to understand the interaction between impinged droplets and surface cooling by conducting experiments with high spatial and temporal resolution of spray cooling heat transfer process to understand how physical parameters such as film thickness, film evolution, and nano-scale features impact the overall heat transfer process.

Aiming to fill the gaps of knowledge in the physics of cooling due to droplet impingement on a surface; a series of well controlled experiments were performed using a dielectric fluid suitable for electronics cooling applications (HFE-7100) with the following objectives:

- To study the droplet impact zone morphology for single and multiple trains of droplets. This required characterizing impact zone size, film thickness at the

impact zone under different conditions. Additionally, interaction of multiple streams were studied.

- To study the effects of coherent droplet impingement on surface temperature with enough spatial resolution to characterize spatial and temporal behavior inside and outside of the impact zone for single and multiple trains of droplets.

- To measure critical heat flux (CHF) over a range of experimental conditions.

- To quantify the effects of droplet variables such as droplet diameter, velocity and frequency (expressed with the corresponding dimensionless numbers) in the case of single train of droplets; and droplet spacing in the case of multiple trains of droplets. The effect of these parameters on surface temperature inside the impact zone as well as on critical heat flux (CHF) will be presented.

- To identify the main heat transfer mechanisms in the droplet impact zone.

C. Organization of this Work

Chapter II provides a detailed literature review of the current state-of-the-art in cooling techniques related to the main subject of the dissertation. The Chapter comprises reviews on work performed on jet cooling, spray cooling and droplet cooling. A review on the hydrodynamic and heat transfer aspects of single droplet cooling is also provided. Finally, the gaps in the current state- of-the-knowledge in the field are identified and presented.

Chapter III describes the experimental set-up used to perform heat transfer and visualization experiments. The experimental set-up is described in detail including an explanation of the calibration procedures followed to minimize uncertainty in the results. Experimental uncertainty for all the measurements is also presented.

Chapter IV comprises the most relevant experimental results including measurement of critical heat flux, surface temperature, and film thickness measurements for single and multiple droplet streams. Finally the major heat transfer mechanisms at the point of droplet impact are identified and discussed.

Chapter V gives a summary of the body of work with the major conclusions highlighted. Recommendations on future work are also included.

CHAPTER II

LITERATURE REVIEW

Thermal management techniques such as jet cooling, spray cooling, and droplet impingement have the ability to dissipate high heat fluxes [4, 5, 6, 7, 8, 9] when compared to single phase cooling methods or pool boiling with the advantage of eliminating the effects of solid-solid thermal interface resistances between the electronic package and the cooling fluid. A review of each of the above mentioned cooling schemes is presented in this Chapter. Research articles on individual droplet cooling are discussed in this Chapter, as well as spray and droplet impingement cooling. A review of studies about the relationship between a single train of impinged droplets and heat transfer at the solid-liquid interface is also presented. Finally, gaps and contradictions of the current state-of-the-knowledge are also identified.

A. Jet Cooling Review

The focus of this section are jet impingement cooling applications in which liquid jets coming from a nozzle impinges the target surface located at some distance from the nozzles tip. Jet impingment cooling is a promising cooling technology as stated by Agostini [10] and Bar-Cohen [6] reviews at the expense of greater pumping power. Figure 3 shows an schematic of a typical single jet configuration. The main geometric variables used in jet cooling are: nozzle diameter (d), center-center spacing between nozzles (S), and distance between nozzle to heater (H). The flow on a jet impinging could be divided into three separate regions: the free jet region, the impingement or stagnation region, and the radial flow or boundary layer region.

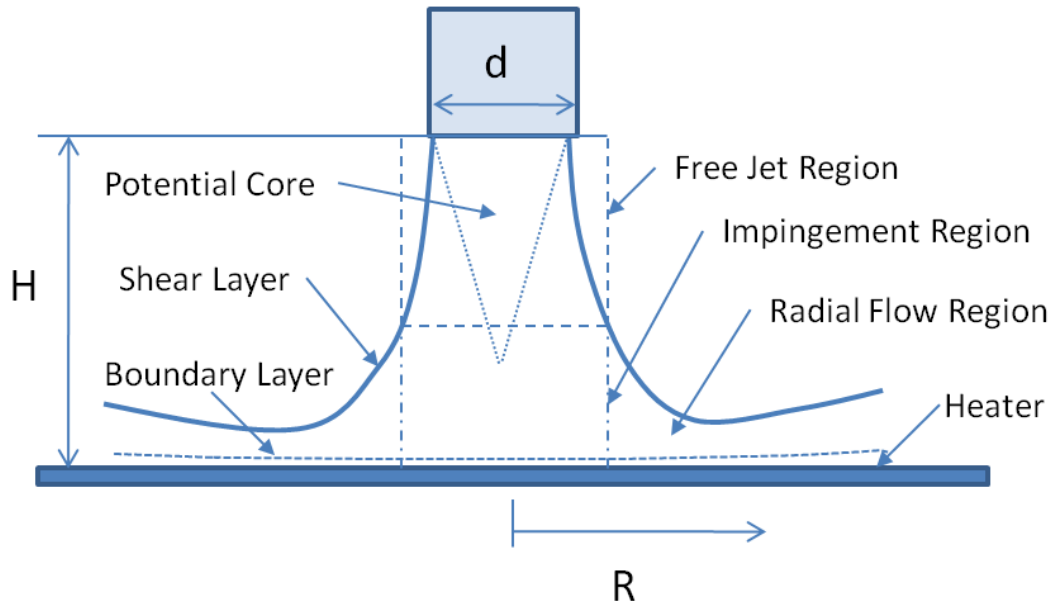

Fig. 3.: Schematic of jet cooling

The free jet region is not affected directly by the surface of the heater and the flow is mainly on the axial direction. This region present a core zone and a free surface which is affected by the shear stress of the surrounding region. In the impingement region, the fluid impinges the surface and turns about 90 ° flowing parallel to the surface. Outside of the impingement region, the fluid flows radially outward where boundary layer effects become dominant. Heat transfer in this region an be characterized as single phase or two-phase depending on fluid and wall temperatures. Jet impingement could also be classified as submerged or free surface jets. Submerged jets have surrounding liquid through which the jet flows, where as free surface jets are surrounded by a gas such as air.

Recent experimental work on single jet impingement cooling have focused on

air as the coolant of choice. Garg et al. [11] developed a synthetic air jet cooling device for applications where space is a constraint. The heat transfer reached a maximum with an enhancement over natural convection cooling by a factor of 8.2, which corresponded to a heat flux of 3.2 W/cm^2 at a heater's temperature of 80 ℃.

Kim et al. [12] investigated heat transfer occurring during the impingement of air jets on aluminum foam heat sinks. The focus of the research was to investigate the effects of pore density, jet velocity, and nozzle-to-heater distance. The average Nusselt number was found to increase with the Reynolds number and with decreasing pore density for a fixed nozzle-to-heater distance because of larger amount of flow passing through the aluminum foam.

Bintoro et al. [13] performed an experimental investigation on heat transfer from a single submerged water jet coupled with a mini-channel air heat exchanger. The system was able to remove 265 W/cm^2 with a heat transfer coefficient of 7 W/cm^2K.

Sun et al. [14] proposed a general equation (2.1) for the local Nusselt number at the stagnation zone for both submerged and free surface jet for the laminar case.

$$Nu_o = 1.25Pr^{1/3}Re^{1/2} \tag{2.1}$$

$$350 \geq Re \leq 6340$$

These research efforts have helped our understanding on how the structure of the liquid flow and heat transfer relate to each other taking into account geometric and dynamical features of the jet. From the experimental investigation, it was established that the heat transfer coefficient depends on Reynolds number, nozzle-to-heater distance, and coolant properties (i.e. thermal conductivity and specific heat). These conclusions are also supported by theoretical work for the wall-jet region based on

boundary-layer approximations [15, 16, 17] as well as by direct CFD numerical simulations based on conservation equations with the appropriate boundary conditions and/or turbulent models [18, 19, 20].

The studies revealed that as fluid starts flowing radially outward, the liquid film thickens forming very thin momentum and thermal boundary layers due to jet deceleration and increase in fluid pressure. As a consequence, extremely high heat transfer coefficients are found in the stagnation zone although with rapid decrease on the radial flow region. Most studies have concluded that jets offer a good solution for localized cooling. However, for chip cooling, the surface temperature variation needs to be limited to just few degrees to ensure proper operation of electronic components. The non-uniformity of jet cooling has prompted investigators to consider the use of arrays of jets for cooling applications. With multiple jets, the interaction among jets becomes crucial making nozzle array configuration very important.

Kim et al. [12] also investigated the effects of a 3x3 array of air jets on aluminum foam heat sinks. They found that an increase in the non-dimensional jet spacing (s/d) (i.e. spacing-to-jet diameter) caused a decrease in Nusselt number. Moreover, increasing the spacing between the nozzle and heater had a negative effect on Nusselt number for a ratio H/d below 8; however, varying the ratio H/d from 8 to 25 resulted in an increase in the Nusselt number. The effect of similar variables on droplet-impingement cooling were considered as part of this study.

Overholt et al. [21] used microfabrication techniques to build compact submerged jet impingement modules with a parallel return system that eliminates the effects of cross-flow, using jet diameters of 300 and 635 μm and outlet holes of 200 and 350 μm. Three nozzle-to-heater distances were used: 362, 686, and 1467 μm. The module with the larger jet diameter had a maximum heat transfer coefficient of 20 $W/cm^2 - K$. The module with the smaller jet diameter reach a heat transfer

coefficient value of 28 $W/cm^2 - K$ at the smallest separation distance.

Fabbri et al. [22] studied heat transfer using an array of free surface microjets with FC-72 as coolant. Jet diameters from 69 to 250 μm were used, with jet spacings of 1, 2, and 3 mm. Equation (2.2) shows the correlated average Nusselt number found for those experiments.

$$Nu = 0.042 Re_{d_j}^{0.78} Pr^{0.48} \exp -0.069 S/d_j \tag{2.2}$$

valid for the following ranges:

$$43 \leq Re_{d_j} \geq 3813$$

$$2.6 \leq Pr \geq 84$$

$$4 \leq S/d_j \geq 26.2$$

Brunschwiler et al. [23] investigated the effects of using several submerged jet cooling modules with a parallel fluid return system on heat transfer. The modules consisted of jet arrays of up to 40,000 jets with diameters ranging 31 to 103 μm and jet spacings between 100 to 500 μm. In the optimal configuration, tested a heat transfer coefficient of 10.5 $W/cm^2 - K$ was measured which allowed a heat removal of 370 W/cm^2 with a junction temperature of 83 ℃.This also suggests that proper spacing of liquid jets is crucial in the dissipation of large amounts of thermal energy.

Kanokjaruvijit et al. [24] cooled an enhanced surface consisting of structures to promote turbulence. The purpose of the structures was to help break the boundary layer thus enhancing heat transfer in the region between structures. They found that

the structures did not always enhance heat transfer.

Natarajan et al. [25] built a modified submerged microjet cooling module capable of removing up to 250 W/cm^2 with pressure dropless than 70 kPa. The device had 1,600 jets with 1,681 returns. Water was used in the single phase mode and operated at Reynolds numbers below 500.

Jet impingement cooling could experience two-phase phenomena, when boiling along the heated surface occurs. The generation of vapor bubbles within the liquid film splashes away a significant portion of the coolant. Increases in heat flux results in the formation of dry spots on the liquid film that spreads radially outside of the impact zone. Eventually, the dryout propagates inwards toward the stagnation zone resulting in dryout and CHF [7].

Boiling from high temperature surfaces experiencing liquid jet impingement can be quite complex. The physics governing heat transfer is still not completely understood and only few theoretical models are available [7, 26].

Experimental studies of two-phase jet impingement cooling have focused on measuring Critical Heat Flux (CHF). For free circular jets, CHF can be enhanced by increasing jet velocity or decreasing jet diameter [7]. In the case of FC-72, jet velocity has a stronger effect on CHF than jet width [27]. Increasing subcooling (using lower fluid temperature) promotes condensation of vapor bubbles in the boundary layer region, thus delaying the wall jet separation and the resulting dryout process.

B. Spray Cooling Review

Early work in spray cooling was done by Kopchikov et al. [28] who studied heat transfer on surfaces cooled by a spray generated by nozzles with orifices in the range of 20 to 200 μm. The fluids used in the investigation were distilled water, ethanol,

carbon tetrachloride, and benzene. The study reported heat fluxes several times larger than for pool boiling. However, spray characteristics such as liquid flow rates, droplet diameters, velocities and frequency of impact were not reported.

Toda [29, 30] obtained a heat transfer curve using distilled water for a wide range of surface temperatures, generating a heat flux-temperature plot similar to a pool boiling curve. The following heat transfer regimes were identified: nucleate boiling, transitional, and film boiling. Two circular heaters were used in the study with diameters of 40 and 15 mm. Droplets velocities and diameters were not measured directly but estimated based on previous empirical data of sprays. The maximum heat flux reported was 407 W/cm^2 with a superheat of 50℃ on the 15 mm heater with water being supplied at a rate of $1.15 \cdot 10^5$ $kg/m^2 - h$ (equivalent to a flow rate of 20,320 ml/hr). Estimated droplet diameter was 117 μm, with impact velocities of 72.4 m/s which corresponds to Weber number of 8,750.

Bonacina et al. [31, 32] performed an experimental study where only a fraction of the total heat transfer surface was impinged with droplets at relatively low superheat values at the liquid-solid interface. Water was used as heat transfer fluid at flowrates between 1.1 to 2.1 cm^3/s (equivalent to a flow rate of 300 ml/hr to 600 ml/hr) with a nozzle at cone angles ranging from 45 to 80 degrees impacting a 25 mm diameter heater. The maximum heat flux reported was of 215 W/cm^2 with a superheat of 36 ℃, and a mean droplet diameter of 90 μm with an estimated velocity of 1 m/s.

Other researchers [33, 34, 35, 36] have reported very large heat fluxes using pressure-atomized nozzles. Tilton [33] studied spray cooling using water as test fluid, impinging a copper test section of 1 cm by 1 cm that was heated using infrared lamps. A maximum critical heat flux of 983 W/cm^2 at 7.33 cm^3/s (equivalent to 26,300 ml/h) was obtained. Droplet diameter in the range of 50 to 100 μm and a velocity of 9 m/s were used. The results suggest that heat transfer is highly dependent

on spray characteristics such as velocity and droplet diameter. In order to improve heat transfer, it was recommended to minimize the size of the impinging droplets and to maximize the ratio of wetted area. Smaller droplets were thought to be more effective due to the formation of a thinner film during impingement which should have resulted in an increase of contact line length (CLL).

Navedo [37] performed a parametric analysis using pressure atomized nozzles and Phase Doppler Particle Analyzer (PDPA) to measure droplets characteristics of the spray including the Sauter mean diameter, velocity and frequency. It was found that frequency of droplet impact and velocity were directly proportional to both critical heat flux (CHF) and heat transfer coefficient at CHF. Sauter mean diameter (d_{32}) was found to be inversely proportional to heat transfer coefficient at CHF but had no effect on the value of CHF.

Ortiz et al. [38] and Estes et al. [39] studied several spray cooling variables in pressure-atomized nozzles including volumetric flux, surface roughness, subcooling temperature, and spray angle. In both studies, experiments using larger mass flow rates resulted in higher heat flux values. Subcooling was shown to have an effect when using dielectric fluids [39] obtaining higher CHF at increased subcooling. Ortiz [38] found a decrease in heat flux with increasing impact angle, and an increase in CHF with surface roughness.

Cho et al. [36] and Estes et al. [39] postulated correlations between heat transfer performance and Sauter mean diameter (d_{32}) of the spray. Hsieh et al. [40] also have confirmed the empirical relationship of the above variables when grouped in the Weber number along with the difference between surface temperature and saturation temperature (ΔT). Cho et al. [36] showed that heat transfer rate was a function of superheat temperature and the Weber number defined in terms of the Sauter Mean Diameter as indicated in Equation (2.3).

$$\frac{q^{''}H}{\mu_f h_{fg}} = 93.8\ We_{d_{32}}^{0.43} \left(\frac{c_f \Delta T_{sup}}{h_{fg}}\right)^{0.98} \tag{2.3}$$

Estes et al. [39] developed a CHF correlation for FC-72, FC-87 and water. The correlation (2.4) shows a strong dependence of CHF on volumetric flux and Sauter mean diameter.

$$\frac{qc^{''}}{\rho_q h_{fg} Q^{''}} = 2.3 \left(\frac{\rho_f}{\rho_g}\right)^{0.3} \left(\frac{\rho_f Q^{''2} d_{32}}{\sigma}\right)^{-0.35} \left(1 + 0.0019 \frac{\rho c_f \Delta T_{sub}}{\rho_g h_{fg}}\right)^{0.98} \tag{2.4}$$

Other group of researchers have focused their attention to air-atomizing nozzles [41, 42, 43]. Monde [41] studied heat transfer phenomena on a thin water layer that covered a heated disk where water was supplied with an air-atomizing nozzle. The study showed an increase of heat flux with an increase in the volumetric flow rate. It also suggested that CHF did not increase after exceeding the critical volume flow rate. Monde [41] proposed that the critical volumetric flow rate was a direct result of the thickness of the nucleate boiling liquid layer.

Yang [42, 43] used an air-atomizing nozzle with water as test fluid on a range of flow rates from 1 to 3 l/h with air pressures on the range of 10 to 50 PSI. The maximum CHF obtained was of 850 W/cm^2 with flowrate of 2 l/h, superheat of 50 ℃, velocity 57 m/s, and pressure air (atomizer) of 50 PSI. A major contribution of their research work was the measurement of film thickness and film topography. In order to measure film thickness, the change in the line of sight was tracked using

a laser beam. The measurement provided the maximum film thickness produced by the spray. Film topography was obtained using a holographic technique. The range of film thickness varied between 75 and 300 μm. Yang [43] suggested that the main mechanism of heat transfer in the case of spray cooling with an air-atomizing nozzle was thin-film nucleate boiling and secondary nucleation caused by impinging droplets.

Chen et al. [44], Griffin et al. [45] and Rini et al. [46, 47, 48] have studied bubble behavior on spray cooling using FC-72 as heat transfer fluid. A transparent heater was used to allow high speed imaging of the surface of the heater. In their visualization studies, they observed bubble formation even without heat transfer attributed to entrapped gas. They also studied several bubble parameters such as bubble growth, bubble diameter at puncture, lifetime, life cycle and bubble number density. They reached the conclusion that impinging droplets provide secondary nuclei for the formation of bubbles. They proposed this secondary nucleation as a mechanism of heat transfer enhancement in spray cooling applications.

More recently, Horacek et al. [49] performed a series of experiments using a single nozzle with FC-72 as the heat transfer fluid. The heater surface consisted of a micro heater array (total of 96 heaters) with a total surface dimension of 7 x 7 mm. The flow rate studied was 11.3 ml/min with a velocity of 21 m/s. Measurements of the contact line length (CLL) were performed on the semitransparent heaters using Total Internal Reflectance (TIR) technique. A strong correlation between contact line length (CLL) and wall heat flux was determined. Critical heat flux obtained in this study were in agreement with Estes correlation (2.4) within an uncertainty of 30%.

Pautsch et al. [50, 51, 52] focused their efforts in studying the liquid film formed in the modified version of the Cray X1 vector supercomputers cooling unit. The fluid delivery system consisted of a ten nozzle array design with two kinds of nozzles. Later the delivery system was modified to include momentum-driven linear nozzles. The

heater consisted of an array of eight 17x17 mm heaters accommodated on a total area of 70x70 mm and was positioned downward. Pautsch[51, 52] used a diffraction technique to obtain the measurement of the film in heat transfer regimes below nucleate boiling. Film thickness on the order of 30 to 60 μm were obtained.

C. Droplet Stream Cooling Review

Most studies have relied on the use of sprays generated by nozzles which usually consist of a wide range of droplet conditions with little to none ability to regulate parameters such as droplet diameter, velocity and frequency. On the other hand, piezo-electric droplet generators provide an alternative way to control those parameters within an acceptable range. Few researchers have studied the pertinent several physical phenomena, including localized heat transfer caused by the coherent impingement of monosized droplets. With an adjustable droplet generator, droplet cooling (i.e. droplet size, droplet velocity, and frequency) can be effectively controlled resulting in conditions ranging from thin films to individual droplet evaporation.

Early work in droplet cooling concentrated on water at temperatures around or higher than the Leidenfrost temperature. Wachters et al. [53] used a spray nozzle to produce droplets in order of 60 μm with an approximate velocity of 5 m/s. In the experiment, the cooling of a disk with an initial temperature of 500 ℃ was reported. Michiyoshi et al. [54] studied experimentally the evaporation characteristics of large water droplets on heated surfaces of various materials at surface temperatures between 80 to 450 ℃. Thermocouples were used to measured surface temperature below the impinged drop as a function of time. The droplet behavior on heated surface was studied using high-speed photography.

Droplet spreading ratio has been experimentally studied by Yang et al.[55]. Yang postulated a correlation for the droplet spreading ratio, β, as a function of the Reynolds number and Weber number(2.5).

$$\frac{1}{2}We = \frac{1}{2}\beta^2\left(1 + 3\frac{We}{Re}\left(\frac{\mu_f}{\mu_s}\right)^{0.14}\left(\beta^2\ln\beta - \frac{\beta^2-1}{2}\right)\right) - 6 \tag{2.5}$$

Halvorson et al.[56, 57] performed an experiment using a stream of monodispersed droplets with diameters ranging from 2 to 4 mm with a velocity of 1.3 m/s and frequencies of 2 to 15 Hz. A CHF of 325 W/cm^2 was obtained, with results suggesting an increase in CHF with thinner films, reduced droplet diameter and increased frequency. The findings of Halvorson [56, 57] were in accordance to the results obtained using pressure atomized nozzles [33, 34, 35, 36] and air-atomizing nozzles [41, 42, 43].

Sawyer et al. [58] performed experiments with droplets in the range of 1.5 to 2.7 mm, velocities in the range of 2.4 to 4.6 m/s at frequencies of 12 to 42 Hz. Heat transfer fluxes were calculated based on the wetted area caused by droplet impact. They also postulated a correlation for the nondimensional critical heat flux as a function of the Weber and Strouhal numbers. Healy et al. [59] modified Sawyer correlation to include results from Holvorson (2.6).

$$\frac{qc''}{\rho_f\left[h_{fg} + 0.1\left(\frac{\rho_f}{\rho_g}\right)^{\frac{3}{4}}c_p\Delta T_{sub}\right]v_d} = 0.146We^{-0.9816}St^{0.6883}\left[\frac{P}{P_{atm}}\right]^{0.6081} \tag{2.6}$$

where:

$$55.0 < We < 730$$

$$7.0 \cdot 10^{-3} < St < 3.0 \cdot 10^{-2}$$

Sheffield [60] performed an investigation to understand the effect of monodispersed stream of droplets with a range of $50-300\ \mu m$, with droplet velocities on the range of 3 to 14.2 m/s on heat transfer. Three orifice plates with different patterns were used to produce droplets including a single 144 μm orifice, a nine hole array (3x3) with 40 μm orifices at a distance of 500 μm between orifice centers and nine hole array (3x3) with 30 μm orifices at a distance of 500 μm between orifice centers. The effect of frequency and Weber number on critical heat flux values were presented; however, a clear distinction among the different configurations was not evident in the analysis.

Sellers [61] modified the set-up used by Sheffield [60] using a charge-based deflection mechanism to control the trajectory of the droplets. The deflection mechanism allowed to position droplets with an uncertainty of 22%. In the study, a correlation of critical heat flux (CHF) in terms of Weber number, and Strouhal number was formulated(2.7).

$$\frac{qc^{''}}{\dot{m}^{''}h_{fg}} = 1.1145We^{-0.1202}St^{-0.1431} \tag{2.7}$$

where:

$$23.0 < We < 202$$

$$0.047 < St < 0.58$$

In the case of deflected streams, Sellers et al. [62, 61] defined the Strouhal number based on the impact frequency of the droplets hitting a fixed point on the surface.

A correlation for critical heat flux (CHF) as a function of Weber number, Strouhal number, and dimensionless spacing between consecutive droplets was also formulated (2.8).

$$\frac{qc''}{\dot{m}'' h_{fg}} = 0.8382 We^{-0.0826} St^{-0.1654} \left(\frac{s}{L}\right)^{0.2391} \tag{2.8}$$

where:

$$23.0 < We < 202$$

$$2.6 \cdot 10^{-5} < St < 0.30$$

$$8.5 \cdot 10^{-3} < \left(\frac{s}{L}\right) < 0.47$$

D. Single Droplet Impact Review

Several researchers have focused their efforts in studying single droplet impact from the hydrodynamic and heat transfer perspective. Moreira et al [63], and Cossali et al [64] provide good reviews of the state-of-the-art of single droplet impingement research. The rationale of these single droplet studies was to generate knowledge to predict the behavior of sprays in applications such as spray cooling of electronic systems and fuel-spray impingement in internal combustion engines. However, there still is a controversy in the scientific community on the usefulness of individual droplet research to predict the outcome of sprays due to the fact that droplet-to-droplet interactions are not considered when studying individual droplet research. Moreover,

some have argued that single droplet studies cannot be extrapolated or used to predict spray behavior since single trains of droplet do not represent the whole spray phenomena. However, studying spray cooling without isolating droplet-to-droplet interactions and factors such as droplet spacing make the in-depth study of spray cooling almost impossible. Therefore, isolating and blocking some of the parameters should allow for a better understanding of the main physical mechanisms at play when droplets impinged a surfaces coherently.

From the hydrodynamic perspective, the most simple case is the impact of a droplet on a dry surface. The phenomena occurring when a single droplet impinges onto a dry surface depends on many factors associated with the interface and the impact conditions. The phenomena can be characterized using impaction energy as proposed by Bai et al. [65], or by a suitable time scale as suggested by Rioboo et al. [66]. The characterization using either approach clearly identifies the following stages: (i) stick, (ii) spread, (iii) splash and (iv) rebound. Rioboo et al [66] also identify the occurrence of (v) fingering after the spreading phase. Moita et al [67] and Riobo et al [66] have identified splashing or disintegration mechanisms of impacting droplets as: (i) prompt splash, (ii) corona splash, (iii) receding breakup, (iv) finger breakup, and (v) partial rebound.

Prompt splash is the disintegration mechanism that is usually used as the criteria between spread and disintegration limits. This prompt splash which takes place within the first instants after impact is dominated by inertial forces with roughness-amplitude playing an important role. In some cases, splashing occurs after the formation of a crown as shown by Rieber et al [68] and Trujillo et al [69]. Prompt splash occurs when the inertial forces overcome capillary forces as expressed by equation (2.9).

$$\rho v_o^2 > \frac{\sigma_{lv} t_l}{d_o^2} \tag{2.9}$$

Furthermore, Stow et al. [70] and Mundo et al. [71] proposed a dimensionless splashing parameter defined by equation (2.10).

$$\kappa_C = A.Oh^a.We^b \tag{2.10}$$

It is worth noting that for particular impact conditions, it is possible to neglect the Ohnersoge number in equation (2.10), making the splashing parameter a function of Weber number only. The correlation (2.10) does not take into account the mechanisms when a droplet impinges onto a rough surface. The role of surface roughness makes it difficult to establish a unique general criterion κ_C for all the disintegration mechanisms. Cossali et al [72] tried to overcome this problem by proposing a variable splashing parameter dependent on dimensionless roughness.

Roisman et al [73] studied the impact of individual droplets on a liquid film finding that impingement behavior depends on Weber number of the droplet and thickness of the liquid film. . Droplet impingement exhibit the following behaviors:

- Deposition and coalescence of the droplet over the film at low Weber numbers ($We < 10$).
- Crater formation on the liquid film at the point of impact of the droplet when the droplet impinges at moderate Weber numbers ($10 < We < 300$).

- Formation of symmetric or asymmetric corona splash at moderate-medium Weber numbers ($We > 300$).

- Film fluctuations causing the destruction of the splashing crown.

- Film jetting with subsequent breakup.

The thickness of the film also influences the droplet impact depending not only on the relationship of the thickness of the film to the droplet diameter but also on the ratio of roughness amplitude R_{ND} to film thickness. Tropea et al. [74] distinguishes four categories of droplet impact on a film based on film thickness as follows:

- Very thin film: when the film is on the order of magnitude of the surface roughness amplitude. In this case the droplet behavior depends on surface topography.

- Thin film: when the ratio of film thickness to droplet diameter is less than 1.5. The dependence of droplet impingement behavior on surface roughness becomes weaker.

- Thick film: when the ratio of film thickness to droplet diameter is between 1.5 and 4. Droplet impact is only dependent on thickness of the film.

- Deep pool: when the ratio of film thickness to droplet diameter is larger than 4. Droplet impact is independent of surface topography and film thickness.

Spray impingement phenomena becomes more complex with variations of surface temperatures with a strong dependence on the ratio of time scales of momentum and heat transfer time scales. Several researchers [75, 76, 77, 78] have taken the

approach to study single droplets in order to incorporate thermal induced effects on the hydrodynamics mechanisms of single droplet impact.

Different heat transfer regimes have been associated with the temperature dependence of droplets deposited onto a hot surface or with the droplet lifetime. Four regimes similar to pool boiling are identified based on surface temperature (T_W):

- Single phase film evaporation ($T_W < T_{sat}$): Heat transfer mechanisms are mainly driven by conduction and convection without phase change.

- Nucleate boiling ($T_{sat} < T_W < T_{CHF}$): Heat transfer with multiphase phenomena which increases with surface temperature up to a maximum at the Critical Heat Flux Temperature (T_{CHF}).

- Transition boiling ($T_{CHF} < T_W < T_{Leidenfrost}$): An insulating vapor layer at the liquid-solid interface is formed which reduces heat transfer down to a minimum at the at the Leidenfrost temperature.

- Film boiling ($T_W > T_{Leidenfrost}$). The vapor layer becomes stable, and the main mechanisms of heat transfer are conduction through the vapor layer and radiation.

In the single phase and nucleate boiling regimes, the contact between solid and liquid phases is permanent which correspond to a wetting regime from the hydrodynamic viewpoint. In the transition regime, the contact is intermittent, while the film boiling regime corresponds to a non-wetting regime.

Extensive research [79] has been performed to determine the departure of the limiting temperatures (T_{CHF} and $T_{Leidenfrost}$) of the heat transfer curve from the

pool boiling case and the parameters that have an effect on such departure. Several research works [80, 81, 82] have reported that droplet diameter has negligible effects on limiting temperatures. Nishio et al. [83] found an increase in $T_{Leidenfrost}$ with droplet. The effect of velocity is not clear with contradictory results. Nishio et al. [83] reported negligible effect of droplet impact velocity for velocities lower than 5 m/s, while other groups reported a decrease [84] or increase [85, 86, 87] of $T_{Leidenfrost}$ at moderate velocities. The Leidenfrost temperature $T_{Leidenfrost}$ increases with surface roughness [88],and impact angle [85]. Critical Heat Flux temperature (T_{CHF}) is relative insensitive to impact conditions [79, 89].

A general representation of the droplet impingement regimes taken into account surface temperature provides a qualitative description of the effect of surface temperature on impingement phenomena. Figure 4 depicts the different impingement modes as described by Bai et al. [65] and Rein [90] based on Weber number and surface temperature (T_W). The regimes are quite complex because the hydrodynamic and thermal effects are conjugated. The common approach to study the regimes has been to perform experimental studies by varying different parameters such as liquid properties, wettability, and impact angle.

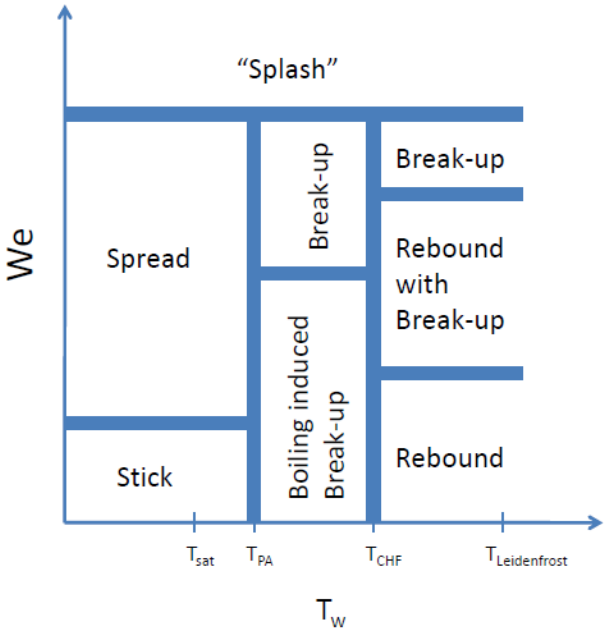

(a)

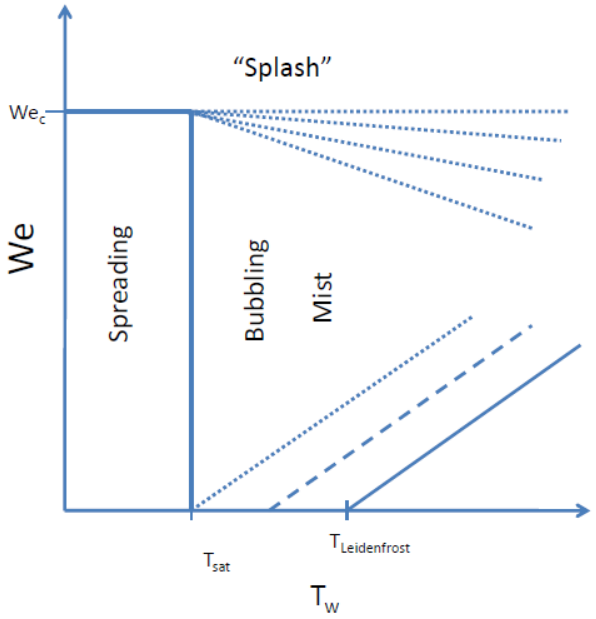

(b)

Fig. 4.: Representations of Impact Regimes. a)Adaptation from Bai et al. [65], b)Adaptation from Rein [90]

E. Identification of Gaps in Current Knowledge Base

Several mechanisms [4, 5] have been proposed to explain heat transfer enhancement in spray cooling when compared to pool boiling. The main mechanisms routinely proposed include: forced convection caused by droplet impingement on the surface, evaporation from the thin-film surface, nucleate boiling, and secondary nucleation. However, due to the inherent complexity of spray cooling, these mechanisms are not completely understood since it is difficult to isolate them. The dependence on many parameters that are not easily adjusted independently have hindered the understanding of the physics of spray cooling.

In the parametric study conducted by Navedo [37] and Chen et al. [91], three parameters were studied namely: velocity, frequency and diameter of droplets. In the study, spray with large velocity, low number of droplets with large diameter was found to be more effective than sprays with low velocity, large number of droplets with small diameter. The conclusions reached by Chen and Navedo are opposite of those reached by Estes et al. [39].

Some other variables studied such as film thickness have only been studied to a limited extent. Yang [43] measured the maximum film thickness in the entire film. Pautsch et al. [51, 92] used a methodology [93] that require complete knowledge of the diffraction coefficient above the heat transfer surface and neglected the possibility of having vapor bubbles within the liquid film. The presence of secondary-nucleation-induced bubbles [46, 44, 94] which have appeared in sprays even without heat transfer would make an estimation of the diffraction coefficient of a film difficult. Other factors studied include surface roughness which have produced contradictory results. Ortiz et al. [38] observed an improvement in CHF at larger surface roughness values while Pais et al. [35] reported the opposite behavior.

Most of the studies in the area of droplet cooling have focused on characterizing critical heat flux (CHF) as a function of droplet stream parameters under the assumption of uniform surface temperature. No effort have been made to characterize or differentiate between heat transfer behavior at the zone of impact of the droplets, and at the liquid film that surround droplet impact zone. Furthermore, some of these studies [58, 61, 59] estimate crown diameter of the impact zone by using the correlation developed by Yang [55] which tends to overpredict experimental values by as much as 31.5% [62]. Accurate crown diameter measurements are necessary to understand the relationship between droplet impingement and surface cooling.

The parametric studies [60, 62] performed on droplet cooling have compared results of single and multiple streams as in the case of Sheffield [60]. In the case of Sellers [62], the studies were performed using only one orifice plate making it impossible to vary independently other parameters for a monodispersed droplet streams. Even in the case that they would have varied the main parameters of the droplet stream, the surface temperature measurement methodology, which consisted of using embedded thermocouples in heating elements, would have limited the assessment and understanding of the key heat transfer mechanisms in the zone of impact of the droplet.

Most of the experimental work focused on studying the impact zone have been done for the case of individual droplet [75, 76, 77, 78, 80, 81, 82, 85, 86, 87] which relied on the use of thermocouples to characterize surface temperature, and studying hydrodynamic phenomena using high speed imaging. The focus of these efforts have been in applications such as fuel injection systems with surface temperatures in the range of Leidenfrost temperature.

CHAPTER III

EXPERIMENTAL APPARATUS DESCRIPTION AND EXPERIMENTAL METHODOLOGY

In this section, the description of the experimental set-up which was designed and constructed to achieve the objectives of the project will be presented. Additionally, the methodology used to calibrate the experimental set-up will be discussed.

In order to achieve the proposed objectives of the research project, an experimental setup was designed, built, and calibrated. The experimental set-up consisted of three main systems, namely: fluid delivery system, heater system and a data acquisition system as shown in Figure 5. The fluid delivery system comprised of a syringe pump, heat exchanger, chiller, droplet generator head, and a frequency generator. The heater system consisted of a power supply, and heater assembly. The data acquisition system consisted of an infrared camera, high speed camera, PC, and an electronic data acquisition system.

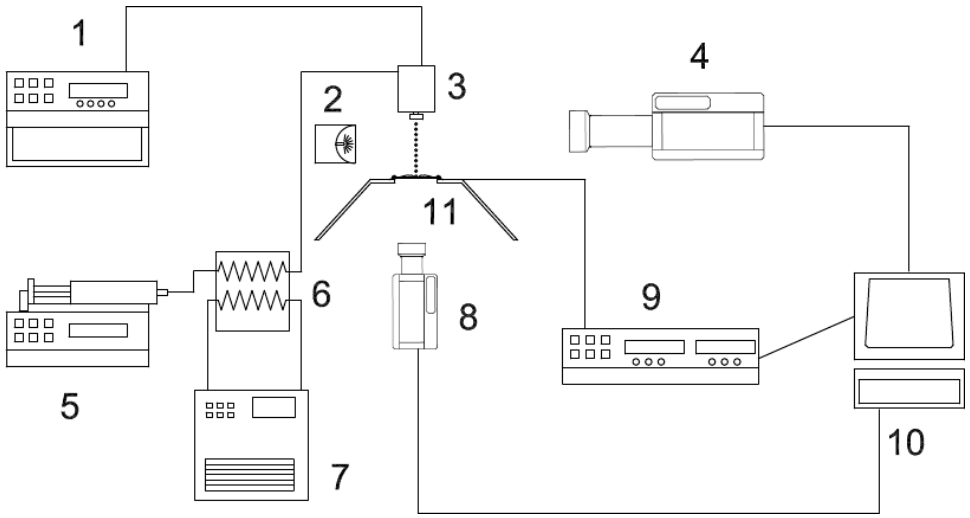

Fig. 5.: Experimental set-up. 1) frequency generator, 2) backlight illuminator, 3) droplet generator head, 4) high speed camera, 5) syringe pump, 6) heat exchanger, 7) chiller, 8) infrared camera, 9) power supply , 10) pc and data acquisition system, and 11) heater assembly

A. Fluid Delivery System

The production of a stream of mono-dispersed sized droplets was achieved using a piezoelectric droplet generator. The fluid was delivered by a syringe pump and disturbed by high frequency vibrations taking place in the piezoelectric electric crystal attached to the orifice plate. An orifice plate with a 150 μm orifice was used to produce the desired droplet stream. The plate was constructed on a heavy substrate of BeCu with a thin layer of Ni where the orifice was etched. Induced vibrations caused the controlled breakup of liquid jets by the Rayleigh breakup mechanism. Square waves at high frequencies were controlled and delivered by a frequency signal generator (BK Precision Model 4011A). The set up was able to generate a monodispersed stream of droplets ranging from 50 to 350 μm, with exit velocities ranging from 1 to 30 m/s.

A view of the impinging droplets captured in flight is shown in Figure 6.

In this research work, 3M ™Novec ™Engineered Fluid HFE-7100 was chosen as a coolant. HFE-7100 is a clear, colorless, non flammable and low-odor dielectric fluid with low toxicity and favorable environmental properties. It is ideal for use in a variety of heat transfer applications, and it is compatible with most electronic components. It is being used for direct contact cooling of computers, transformers and fuel cells. Appendix A list the most important properties of HFE-7100.

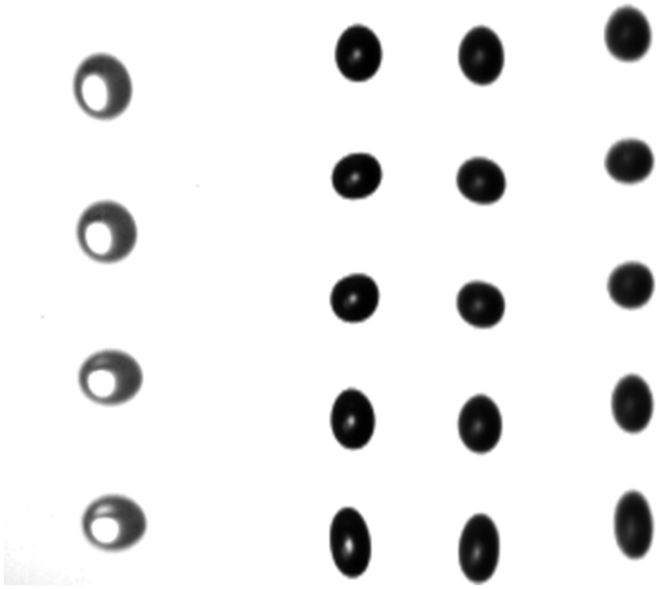

(a) (b)

Fig. 6.: Droplet streams. a) Single (d= 318 μm, f= 2,970 Hz.), b) Triple (d= 235 μm, f= 7,320 Hz.)

B. Heater System

The heater was made by coating a 0.787 mm thick Zinc Selenide (ZnSe) substrate with a surface quality of 60-40 with a thin layer of Indium Tin Oxide (ITO) of approximately 100 nm in thickness to obtain a resistance of approximately 50 Ω/sq. ZnSe was chosen due to its good transmissivity in the optical range, from 0.4 to 0.7 μm, and in the infrared range, from 1 to 13 μm. ITO was chosen mainly for its very high transmissivity in the optical range as well. Combined ZnSe and ITO, provided high transmissivity in the optical range which is compatible with other optical experiments; and exhibits good infrared transmissivity through the bottom part of the ITO coating which is compatible with infrared thermography.

The dimensions of the heater are 15 by 10 mm (see Figure 7). Two wires were attached to the heater surface using a silver-based electrical conductive epoxy to provide electrical connectivity between the power supply and the heater. Once the wires were attached, the usable area was about 0.9 cm^2.

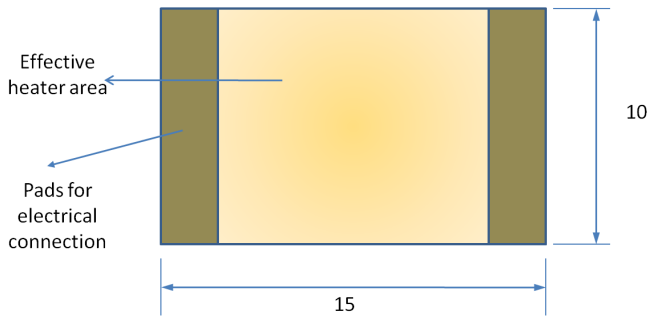

Fig. 7.: Heater schematic

The assembly of the heater was attached to a Teflon ® holder using an optical

grade epoxy. The droplets always impinged the heater on the ITO coating side.

Power was supplied using a 1500 W power supply (Lambda GEN600-2.6). The power supply was controlled by a PC through serial port communication using Microsoft Hyper Terminal version 5.1. The estimated uncertainty in heat flux measurement was $\pm 1.24\ W/cm^2$. An estimation of heat flux uncertainty is provided below. A schematic representation of the temperature measurement set up is depicted in Figure 8.

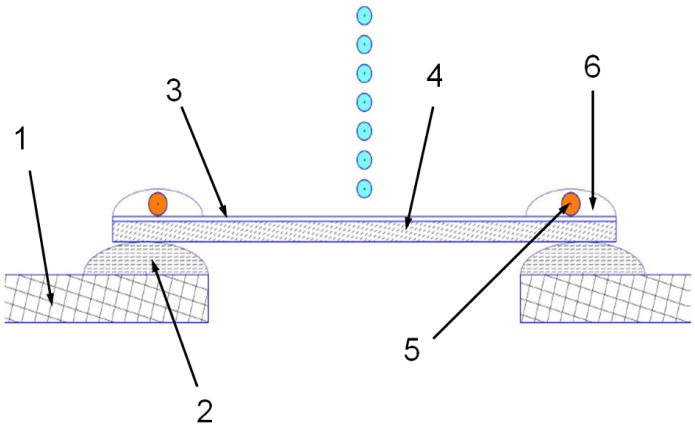

Fig. 8.: Heater set-up: 1) Holder; 2) Optical Grade Epoxy; 3) ITO Coating; 4) ZnSe Substrate; 5) Copper Wire; 6) Electrical Conductive Epoxy

Temperature was measured using an infrared camera (FLIR A325) located below the heater. The infrared camera with a resolution of 320 x 240 pixels was able to collect data at a frequency of 60 Hz. The temperature range of the camera was between 0 and 350 ℃. The camera was used with a close up lens (Model AT197215) with a spatial resolution of 100 μm, and FOV (field of view) of 32 x 24 mm. The IR

camera was connected to a PC through an Ethernet connection, and controlled using ExaminIR package from FLIR. Analysis on the temperature readings indicated an uncertainty of ± 1.6℃ at 55 ℃, and ± 0.8 ℃ for measurements at 40 ℃ as described below. Figure 9 shows samples of infrared images for one-stream and triple-stream droplet impact zones.

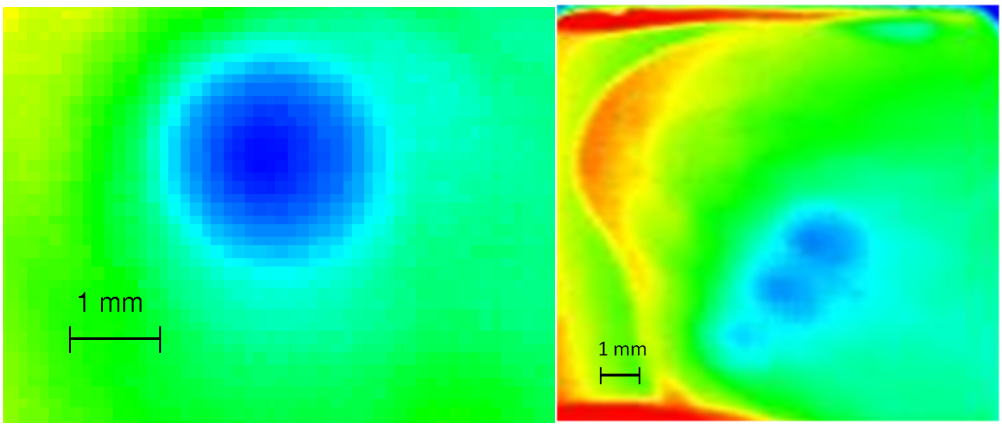

(a) (b)

Fig. 9.: Infrared images of impinged droplets. a)single stream, b) triple streams

C. High Speed Imaging System

The imaging system consisted of a high speed Photron SA3 camera capable of recording images at 1,000 frames per second (fps) at a resolution of 1,024 x 1,024 pixels, and up to 60,000 fps at a reduced resolution of 128 x 16 pixels. High magnification zoom lenses (zoom 6000 series lens Navitar) were used with the system. These lenses were capable to work with coaxial and backlight illumination, and attachments that could be used to provide the required magnification to be able to observe individual droplets at a magnification of 18X. A magnification of 0.35X was used to capture the

total dimension of the film.

Images of the droplets were obtained with the high speed camera (see Figure 6) using backlight illumination at the proximity of the heater surface. The Image Analysis Tool from National Instruments was used to measure the projected vertical surface area of each droplet which in turn was used to compute droplet diameter. A magnification of 1.5 μm/pixel was used for droplet measurement with a corresponding uncertainty value of ± 7.5 μm in diameter. These values were compared to the theoretical values given by (3.1):

$$d_d = \left(\frac{6Q''}{\pi f} \right)^{1/3} \tag{3.1}$$

Images of crown diameter upon impact were obtained using two approaches. First, direct images from above were obtained by inclining the high speed camera 35 degrees. Second, images were also obtained by placing a 45 degree mirror below the heater and illuminating the heater from above. Figure 10 shows images obtained from both methodologies. A magnification of 5.88 $\mu m/pixel$ was used. An estimated uncertainty of $\pm$ 4 pixels was considered for crown diameter measurements. The value of crown diameter measurement uncertainty was estimated to be $\pm 24 \mu m$.

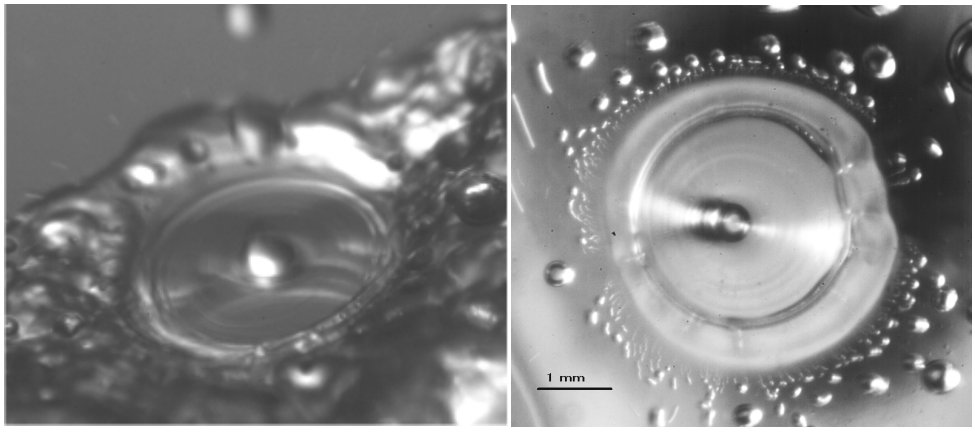

(a) (b)

Fig. 10.: Crown formation images. a) above, b) below

D. Film Thickness Experimental Apparatus

A total internal reflection technique [92, 93] was used to measure film thickness inside the crown formation due to droplet impingement. The technique consisted on measuring the diameter (with and without liquid film) produced by the first fully reflected light ray coming from a laser light source underneath the heated surface. The measured diameters were used in combination with the Fresnel equations (**??**) to determine the film thickness above the surface. Figure 11 shows the path followed by the first fully reflected ray and defines the relevant geometric relations for cases with and without film above the surface. The first fully reflected light ray occurs at the critical angle between the liquid and air interface when there is a liquid film above the surface (θcvl). In the case of a dry surface, it occurs at the critical angle between the solid wall and air (θcvs). The Fresnel relation for the liquid and air interface critical angle is given by Equation (3.2). Equation (3.3) defines the Fresnel relation for the solid wall and air interface.

$$\theta_{cvl} = \arcsin \frac{n_v}{n_l} \tag{3.2}$$

$$\theta_{cvs} = \arcsin \frac{n_v}{n_s} \tag{3.3}$$

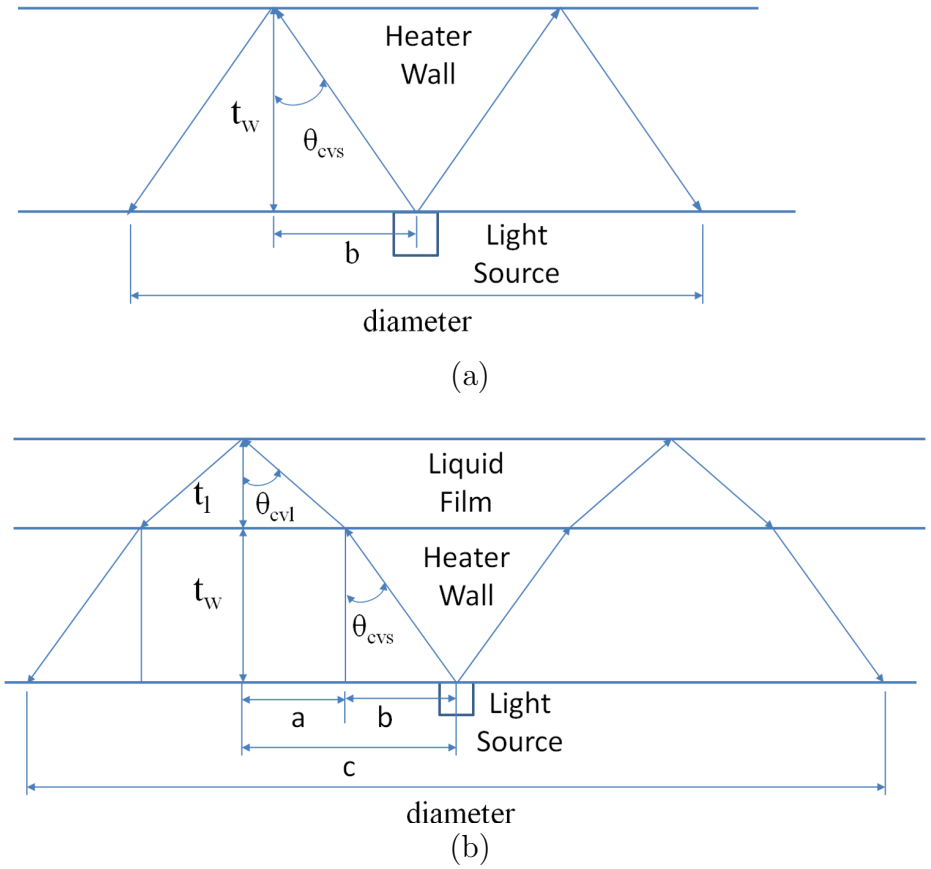

Fig. 11.: Dimensions definitions for film thickness measurement methodology. a) without liquid film, b) with liquid film

By measuring the diameters of the ring produced by the diffraction of light with

fluid and without fluid, variables c and b are easily determined (see Figure 11). It can be shown that the thickness of the film can be obtained using Equation (3.4).

$$t_l = \frac{c}{\tan\theta_{cvl}} - \frac{b}{\tan\theta_{cvl}} \tag{3.4}$$

where:

$$b = t_w \tan\theta_{cvw}$$

The light source for film thickness determination was a 10 mW laser (Lasiris) which emits a green ray with wavelength of 532 nm focused at the center of the droplet impingement zone. The bottom part of the heater was covered by a thin opaque coating to avoid reflection at this interface. The imaging system consisted of a high speed Photron SA3 camera capable of recording images at 1,000 frames per second (fps) at a resolution of 1,024 x 1,024 pixels, and up to 60,000 fps at a reduced resolution of 128 x 16 pixels. High magnification zoom lenses (zoom 6000 series lens Navitar) were used with the system with a 0.5 X lens attachment. It is worth noting that since this technique requires knowledge of the refraction index of the film above the surface, it is only suitable for measuring film thickness where no vapor or air bubbles are present [93].

The total internal reflection technique was further validated by measuring the thickness of the heater using the described technique and comparing the results with readings of a high precision micrometer. Measurement with micrometer was $787.4 \pm 12.7\ \mu m$, the refractive index technique resulted in $779.8\ \mu m$. Also, results of this technique were used to measure film thickness outside the crown formation without heat transfer were compared with the laser induced fluorescence technique (LIF) which has been previously used for measuring film thickness for falling films around

a cylinder [95]. In this technique, a cross section of the impact zone of the impinging droplet was illuminated using a laser sheet which makes the free surface visible. The light source was a 10 mW laser (Lasiris ®) emitting a green ray with wavelength of 532 nm. Line generators with fan angles of 1 and 5 degrees were used to produce the laser sheet. The cooling fluid (HFE-7100) was mixed with a fluorescent -red nile-dye in a concentration of 5 mg per 100 ml of fluid. The mixture is later filtered using a 20 μm membrane filter. The high speed imaging system was used to obtain images of the illuminated section at a small inclination in order to be able to see inside the impact zone at a velocity of 60 frames per second. Pixels resolutions of 1.3 μm were used in the system. The average result of film thickness obtained with the LIF technique was 70 to 100 μm compared with the total internal reflection technique which provided thickness values between 80 to 90 microns. In summary the total internal reflection film thickness measurement technique yielded much greater film thickness accuracy than the other two techniques. The film thickness results are presented in Chapter IV which are used to understand the main heat transfer mechanisms taking place inside the droplet impingement zone.

E. Temperature Measurement

In infrared thermography [96, 97], the temperature of an object is obtained by measuring irradiance W ($W/str - m^2$). The temperature of interest in this particular setup is measured at the interface of ZnSe substrate and ITO coating. Figure 12 shows a schematic of the five irradiance components received by the IR camera when a thin film heating element is attached to translucent substrate in the IR range.

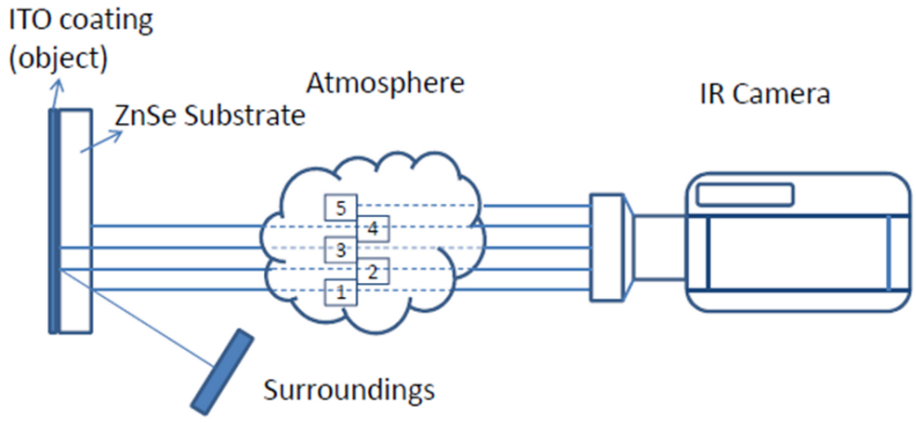

Fig. 12.: Schematic of temperature measurement device using ZnSe and ITO coating as heater

The irradiance components in this case are:

1. Irradiance from surroundings reflected on substrate surface, and transmitted through ambient air.
2. Irradiance from surroundings transmitted through the substrate, reflected on ITO coating and transmitted through ambient air.
3. Irradiance emitted by ITO coating transmitted through substrate and ambient air.
4. Irradiance emitted from substrate, and transmitted through ambient air.
5. Irradiance emitted by ambient air.

The total irradiance received by the IR camera from each of the components can be expressed as follows:

$$W_{tot} = \underline{\rho}_{sub}\tau_{atm}W_{surr} + \tau_{sub}\underline{\rho}_{obj}\tau_{sub}\tau_{atm}W_{surr} + \varepsilon_{obj}\tau_{sub}\tau_{atm}W_{obj} + \varepsilon_{sub}\tau_{atm}W_{sub} + \varepsilon_{atm}W_{atm} \tag{3.5}$$

It is assumed that the irradiance from the substrate can be represented by irradiance of the object and difference irradiance:

$$W_{sub} = W_{obj} + W_{diff} \tag{3.6}$$

Inserting Equation (3.6)in Equation (3.5), the following expressions is obtained:

$$W_{tot} = (\underline{\rho}_{sub} + \tau_{sub}\ \underline{\rho}_{obj}\ \tau_{sub})\ \tau_{atm}\ W_{surr} + (\varepsilon_{obj}\ \tau_{sub} + \varepsilon_{sub})\ \tau_{atm}\ W_{obj} + \varepsilon_{atm}\ W_{atm} + \varepsilon_{sub}\ \tau_{atm}\ W_{diff} \tag{3.7}$$

Emissivity of the substrate (ZnSe) can be estimated based on transmissivity property data of ZnSe and the assumption that ZnSe behaves as a gray body in the wavelength range of interest (8 to 12 μm). Transmissivity of a ZnSe window with a thickness of 1.5 mm with antireflective coating is above 0.90. Assuming a perfect coating with zero reflectivity, the emissivity value is in the order of 0.04. Emissivity is even lower in the case of a non-perfect coating.

The irradiance difference term is the difference between irradiance of the object (ZnSe - ITO interface) and the ZnSe surface. Irradiance is a function of absolute temperature, and its value is proportional to the difference of absolute temperature of the two objects. In the case of the setup having a substrate with a thickness of 1.2 mm, it is safe to assume that the difference of temperature between the two surfaces is very small. This fact means that the irradiance difference term is very small too.

Based on the fact that emissivity of the substrate and the irradiance difference term are very small, it is safe to ignore the last term of Equation (3.7)

$$\underline{\rho_{eq}} = (\underline{\rho}_{sub} + \tau_{sub}\ \underline{\rho}_{obj}\ \tau_{sub}) \tag{3.8}$$

$$\varepsilon_{eq} = (\varepsilon_{obj}\ \tau_{sub} + \varepsilon_{sub}) \tag{3.9}$$

As a result, Equation (3.7) can be modified as follows:

$$W_{tot} = \rho_{eq}\ \tau_{atm}\ W_{surr} + \varepsilon_{eq}\ \tau_{atm}\ W_{obj} + \varepsilon_{atm}\ W_{atm} \tag{3.10}$$

Equation (3.10) represents the total irradiance received by the IR camera from a single opaque equivalent surface. Taking into account the above assumptions, the main irradiance components are as follows:

1. Irradiance from surroundings reflected on an equivalent surface, and transmitted through ambient air.
2. Irradiance emitted by equivalent surface and transmitted through ambient air.
3. Irradiance emitted by ambient air.

For the experimental cases tested, the following assumptions were found to be valid.

1. At any surface, all energy is absorbed, reflected or transmitted (Equation (3.11)).
2. For small temperature ranges, it is safe to assume that the object is a graybody, which means that it is possible to assume that emissivity and absorptivity of

the equivalent surface are the same and constant in the wavelength of interest (Equation (3.12)).

3. The surface subject to measurement is opaque which means zero transmissivity in the wavelength of interest (Equation (3.13)).

4. Ambient air is also considered to be a graybody and its reflectivity is assumed to be zero (Equations (3.14) and (3.15)).

$$1 = \alpha + \underline{\rho} + \tau \tag{3.11}$$

$$\alpha_{eq} = \varepsilon_{eq} \tag{3.12}$$

$$\tau_{eq} = 0 \tag{3.13}$$

$$\alpha_{atm} = \varepsilon_{atm} \tag{3.14}$$

$$\rho_{atm} = 0 \tag{3.15}$$

The above assumptions simplify Equation (3.10) as shown below (Equation (3.16)):

$$W_{tot} = \varepsilon\ \tau\ W_{obj} + (1-\varepsilon)\ \tau\ W_{surr} + (1-\tau)W_{atm} \tag{3.16}$$

The sensor of the IR camera receives radiation energy according to Equation (3.16). The irradiance received by the sensor is converted to an output signal (volts). The output signal received by the detector is amplified and converted electronically into a digital value D (units = digital counts). The digital readings of the camera (D) and the irradiance (W) are related according to the following equation:

$$D_{tot} = A + B\ W_{tot} \tag{3.17}$$

where:

A = Constant taking into account internal irradiance effects of the camera

B = Constant taking into account detector response to irradiance

Constant A is a fixed response of the sensor due mostly to the heat generation of electronic components inside the camera. Constant B represents the linear response of the camera to incoming irradiance. The higher the value of constant B is, the more sensitive the camera becomes.

In the case of a blackbody, irradiance and absolute temperature are related through the Planck function in which the irradiance varies exponentially with temperature. A good approximation of the absolute blackbody temperature as a function of irradiance is the following:

$$T_{tot} = F + G\ ln(W_{tot}) \tag{3.18}$$

where:

F and G are constants used to represent the Planck Function.

Equations (3.17)and (3.18) are combined in order to obtain an expression that relates absolute temperature with the digital reading (counts of the camera) as follows:

$$T_{tot} = A^* + B^* ln(D_{tot}) \tag{3.19}$$

where:

A^* = constant to account for internal effects of the camera.

B^* = constant to account for detector response of the camera.

The calibration constants A^* and B^* are obtained by measuring the camera response to a series of blackbodies at different temperatures and using regression method for data fitting. It is worth to notice that this calibration was performed by the camera manufacturer using NIST-traceable calibrated blackbody sources and thermocouples.

In order to obtain the surface temperature of an object, Equations (3.16) and (3.17) were combined and solved for the equivalent digital reading of the object (D_{obj}) as follows:

$$D_{obj} = \frac{1}{\varepsilon\ \tau} D_{tot} - \frac{1-\varepsilon}{\varepsilon\ \tau} D_{surr} - \frac{1-\tau}{\varepsilon\ \tau} D_{atm} \tag{3.20}$$

Combining equations (3.19) and (3.20), it is possible to obtain an expression for the temperature of the object expressed as a function of the digital value from the camera, and average temperatures of the surroundings and ambient air as shown in Equation (3.21):

$$T_{obj} = A^* + B^* ln\left(\frac{1}{\varepsilon\ \tau} D_{tot} - \frac{1-\tau}{\varepsilon\ \tau} e^{\frac{T_{surr}-A^*}{B^*}} - \frac{1-\tau}{\varepsilon\ \tau} e^{\frac{T_{atm}-A^*}{B^*}}\right) \tag{3.21}$$

The digital value of the object is then used in Equation (3.21) to obtain the tem-

perature of the object. Equation (3.21) is embedded in the software of the camera (Examin IR), which needs surround and ambient air temperatures, emissivity of the object, and transmissivity of ambient air. The software of the camera Examin IR has an embedded algorithm to calculate transmissivity of ambient air using relative humidity of air, temperature, and distance from object to the camera. It is worth indicating that at small distances and laboratory conditions, transmissivity is considered to be equal to one.

F. Emissivity Measurement and Uncertainty Analysis

In this research, standard ASTM E1933 "Standard test methods for measuring and compensating for emissivity using infrared imaging radiometers"[98] was used to measure emissivity of the equivalent surface. ASTM E1933 methodology to measure emissivity using a reference material of known emissivity can be summarized as follows:

1. Measure the digital reading of the irradiance from surroundings where the temperature measurement will be performed (Equation (3.19) applied to surroundings). This was done by placing a reflective foil over the surface to be measured and recording digital counts. The reflective foil would suppress the irradiation from the object reaching the camera only allowing reflection from the surroundings to reach the camera. Due to the small distance between the camera and the object, the effect of ambient air is negligible.

2. Apply a coating of known emissivity to a small section of the surface of the ITO heater.

3. Heat the object so its temperature is at least 30 ℃ above the temperature

of the surroundings. Measure both the number of irradiance counts from the target and object of known emissivity.

Using this methodology, the emissivity can be calculated using Equation (3.22) where D represents the digital reading of the camera in number of counts [96]. Note that D_{ref} refers to the total digital value measure of the reference object.

$$\varepsilon_{obj} = \frac{D_{tot} - D_{surr}}{D_{ref} - D_{surr}} \varepsilon_{ref} \tag{3.22}$$

The emissivity of the equivalent surface was found using the above mentioned methodology. The reference material was placed on the ZnSe surface to determine its emissivity. The heater and reference material were placed in a laboratory oven for 3 hours at three different temperatures. The reference used for this measurement was an electrical vinyl tape Super 88 with a known emissivity value of $\varepsilon = 0.95 \pm 0.05$. The IR camera was focused on the interface ZnSe-ITO layer. The calculated emissivity values at different temperatures are listed in Table I.

Table I.: Emissivity values of equivalent surface at different temperatures

Temperature ℃	Emissivity ε
74	0.790
52	0.798
45	0.798

Driggers [96] used the Kline-McClintock [99] methodology to compute the error propagation in emissivity measurement. The proposed expression is Equation (3.23).

$$\left(\frac{\Delta\varepsilon_{eq}}{\varepsilon_{eq}}\right)^2 = \sqrt{\left(\frac{\Delta\varepsilon_{ref}}{\varepsilon_{ref}}\right)^2 + 2\Delta D^2\left(\frac{1}{(D_{tot}-D_{surr})^2}\frac{1}{(D_{ref}-D_{surr})^2}\right)} \tag{3.23}$$

The uncertainty value of the counts readings was found by computing the standard deviation (σ) of statistically significant readings of the uniform target. Assuming a normal distribution of the measurements, a range of three-standard deviations (3 σ) gives a probability of 99.7% that the result lies within the range. Applying equation (3.23), the emissivity uncertainty of the equivalent surface was found to be 0.792 ± 0.43.

G. Temperature Measurement Uncertainty Analysis

The first step required to compute the temperature uncertainty of the camera was to plot the apparent temperature (done when the object emissivity was set to one), and the counts digital readings of the camera over a temperature range of interest (Figure 13). Using the least squares method and Equation (3.18), the values of the calibration constants of the camera (A^* and B^*) were found be $A^* = -1014.8$ and $B^* = 104.97$.

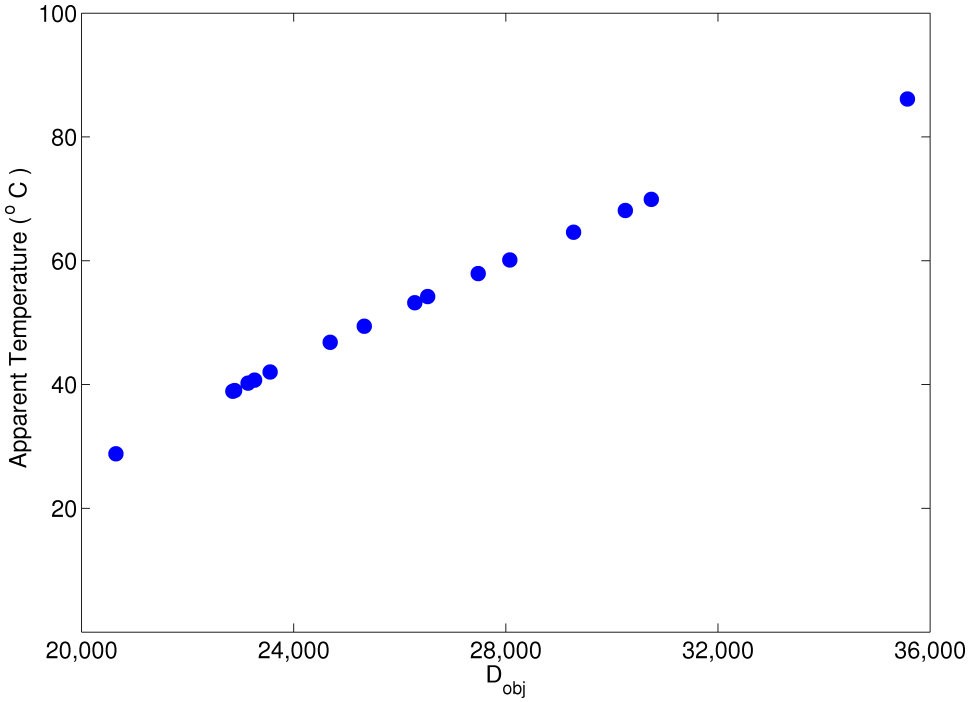

Fig. 13.: Apparent surface temperature vs. digital counts

Using Equation (3.18) and the Kline McClintock methodology [99], the temperature uncertainty was foundusing the following Equation(3.24):

$$\Delta T = \frac{B^* \ \Delta D_{eq}}{D_{eq}} \tag{3.24}$$

The uncertainty of the digital value of the equivalent surface (D_{eq}) cannot be expressed directly, instead, it is expressed as a function of the background, ambient air and total readings (as stated in Equation (3.24)). At small distances between the camera and target, the effects of water vapor in ambient air are considered negligible. In those cases, it is safe to assume that $\tau_{atm} = 1$ and $\rho_{atm} = 0$; then Equation (3.24) is transformed to:

$$\Delta T = \frac{B^*}{D_{tot} - (1 - \varepsilon_{eq})\, D_{surr}} \left[\Delta D_{tot}^2 + \Delta D_{surr}^2 (1 - \varepsilon_{eq})^2 + \Delta \varepsilon_{eq}^2 \left(\frac{-D_{eq} + D_{surr}}{\varepsilon_{eq}} \right)^2 \right]^{1/2} \tag{3.25}$$

D_{tot} was obtained by taking readings of the object using digital counts mode. On the other hand, D_{surr} was obtained by taking readings at the target location covered with a reflective foil as indicated previously. The uncertainty values of the digital readings were obtained by computing the standard deviation of statistically significant samples of the total and surroundings (D_{tot} and D_{surr}) as it was done in the case of emissivity uncertainty measurement. Applying Equation (3.25) using three different digital reading values of the equivalent surface, representing three different temperatures results in the following temperature measurement uncertainties listed on Table II.

Table II.: Temperature uncertainty at different temperature values

Temperature (℃)	Temperature Uncertainty (℃)
30	0.5
40	0.8
55	1.6

The variation of uncertainty is due to an increment of the difference between $D_{tot} - D_{surr}$ as represented by the third term in Equation (3.25). If emissivity had a deterministic value, the values of uncertainty would become ± 0.06 ℃ at an apparent

temperature of 55 ℃.

Besides conducting an uncertainty analysis of temperature measurement, validation experiments were conducted using a thin film thermocouple attached to the backside of the heater to obtain temperature readings along with the IR camera. Power was applied to the heater and surface temperature was monitored using the IR camera and the attached thermocouple (TC). Once steady state conditions were reached, readings of the IR camera and attached thermocouple (TC) were taken. At low temperatures, the difference between the readings was low. The difference between TC and IR readings increased with temperature due to the cooling fin-effect of the thermocouple. Table III shows the results of the validation test.

Table III.: Temperature measurement validation results for heater test

Thin Film Thermocouple (℃)	Infrared Camera (℃)
25.5	25.8
36.0	37.2
42.0	44.2
49.1	52.1

A second validation procedure using an oven to ensure isothermal conditions was also performed. A ceramic thermal insulator with a thin-film type T thermocouple attached to it and covered with a tape with of known emissivity ($\varepsilon = 0.95$) was used as the experimental sample. Once the entire sample reached isothermal condition, the sample was quickly taken out of the oven and infrared images and TC readings were taken simultaneously. The difference between IR camera and attached thermocouple

readings were less than 1.0 ℃ in the four cases. The results of the comparison are presented in Table IV.

Table IV.: Temperature measurement validation results using an oven

Thin Film Thermocouple (℃)	Infrared Camera (℃)
33.8	33.7
38.0	37.2
46.1	45.9
60.0	59.0

Sellers [62] performed a similar validation experiment of surface temperature using a thin film heater. An infrared radiometer system ($ThermaCAM^{TM}$ by Inframetrics) was used to validate the readings of an array of thin-film thermocouples located 2.54 mm below the surface of the heater. The heater was tested for temperatures in the range of 25 to 130 ℃. The difference in temperatures readings between the infrared camera and the thin-film thermocouples was less than 4 ℃ in those experiments.

An experiment was performed with the objective of providing verification of temperature measurement technique for pool boiling.

The set-up was similar but used but with a silicon heater. The heater was made by coating the polished side of a 300 μm thick silicon wafer with a thin layer of ITO (Indium Tin Oxide). The dimensions of the heater were 20 x 14 mm, but the usable part of the heater was 11 x 14 mm after being connected to power (copper) wires. Two copper wires were attached to the heater surface using a silver-based

electrical conductive epoxy to provide electrical connectivity from the power supply to the heater. The assembly of the heater was attached to a Teflon holder using an optical grade epoxy. A transparent holder piece was glued to the substrate, in order to have a column of fluid above the heater.

The power was supplied by a 1500 W power supply (Lambda GEN600-2.6). The power supply was controlled by a PC through serial port communication using Microsoft ® Hyper Terminal version 5.1. Temperature was measured using an infrared camera (FLIR A325) located below the heater. The infrared camera had a resolution of 320 x 240 pixels and was able to collect data at a frequency of 60 Hz. The temperature range of the camera was 0 - 350 ℃. The camera had a close up lens (Model AT197215) with a spatial resolution of $100\mu m$, and field of view (FOV) of 32 x 24 mm.

An amount of fluid of about 60 ml was poured into the container. The height of fluid above the heater was approximately 4 cm. Power was applied and temperature was monitored at the center of the heater until steady state conditions were reached. Once temperature was oscillating by less than 0.5 ℃ for 2 minutes, temperature measurements and high speed images were taken.

Table V provides the results for pool boiling tests performed. Mean Temperature was the average of 199 IR frames (3.33 seconds at 60 Hz) in the Region of Interest (box in the middle of the heater). Minimum and Maximum temperatures are absolute minimums and maximums temperatures in the region of interest for the entire 199 IR frames.

Table V.: Temperature measurement verification using pool boiling

Heat Flux (W/cm^2)	Mean Temperature (℃)	Minimum Temperature (℃)	Maximum Temperature (℃)
3.9	41.6	40.7	42.7
4.9	50.0	48.9	51.2
6.6	58.3	57.0	59.6
8.0	64.0	63.9	65.7
9.0	65.83	63.73	67.19

The following observations can be made from the temperature measurement verification using pool boiling:

- Nucleation at the region of interest (ROI) was only observed at heat fluxes of 8 and 9 W/cm^2 when temperature were above 60 ℃.

- In the case of heat flux of 6.6 W/cm^2 (mean temperature of 58.3 ℃) no nucleation was observed in the ROI, however some nucleation was observed nearby the wire leads.

- In the case of heat flux of 4.9 W/cm^2 (mean temperature of 50 ℃) no nucleation was observed.

- Difference of maximum and minimum temperature in the zone of interest was less than 4 ℃ in all cases.

- There is a good agreement in the temperature measurements and nucleation observation given the saturation temperature of HFE-7100.

The above findings further validate that the devised IR thermal imaging technique provides accurate and reliable data for the analysis of droplet impingement during surface cooling.

H. Heat Flux Measurement and Uncertainty Analysis

In the setup, there are three heat losses modes including (1) natural convection on the both sides of the heater, (2) conduction through the holder, and (3) conduction and then convection through the connecting wires. The three modes are driven by the temperature difference between the heater and surroundings. In this setup, the losses are determined by keeping track of the amount of power needed to maintain a given surface temperature on the heater while there is not liquid impacting the heater.

Heat losses were measured when no droplet impingement on the top part of the heater was taken place. Average surface temperatures on the backside of the heater were recorded after the surface temperature reached steady state. Figure 14 shows a linear correlation between the power input and steady state wall temperature. It is worth noting that the heat losses measured experimentally are in the order of 8 to 11 % of the total input power.

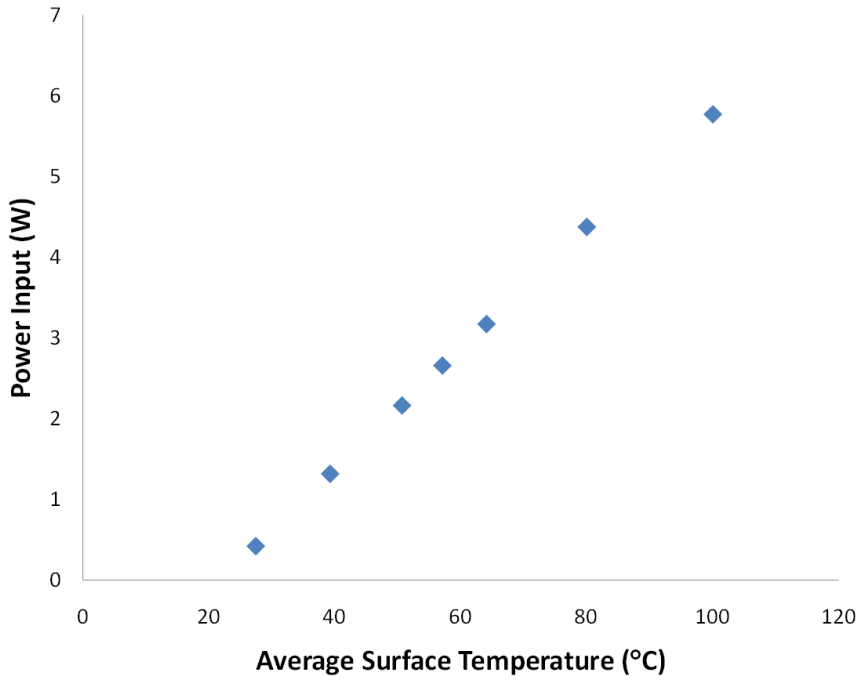

Fig. 14.: Power input as a function of average surface temperature for ZnSe-ITO heater

Equation (3.26) was used to compute heat flux while performing droplet impingement cooling experiments.

$$q'' = \frac{(P_{in} - q_{loss})}{A_{htr}} \tag{3.26}$$

As indicated above, heat flux was imposed using a DC power supply connected to the ITO heater to provide heat in-situ. The uncertainty associated with the calculation of heat flux can be found using the Kline McClintock methodology[99] as follows:

$$u_{q''}^2 = \left(\frac{\partial q''}{\partial V} u_V\right)^2 + \left(\frac{\partial q''}{\partial I} u_I\right)^2 + \left(\frac{\partial q''}{\partial T} u_T\right)^2 + \left(\frac{\partial Q q''}{\partial A} u_A\right)^2 \tag{3.27}$$

The error associated with the measurement of voltage and current for power supply GEN- 600-2.7 used in this experimental work according to manufacturers was:

u_V=0.1 % reading+0.2 % rated output voltage

u_I=0.1 % reading+0.4 % rated output current

Uncertainty values for voltage and current associated with measurement of maximum heat flux were found to be 1.2 V and 0.012 Amps, respectively. Applying the above values of uncertainty to equation (3.27), the uncertainty associated to heat flux measurement was found to be 1.24 W/cm^2 which is approximately 4.8% of the minimum critical heat flux obtained during the experimental work.

I. Crown Diameter and Film Thickness Measurement Uncertainty Analysis

National Instrument vision assistant was used for measuring the diameter of the impact zone produce by droplet impingement under constant heat flux conditions. For crown diameter measurement, a magnification of 5.88 $\mu m/pixel$ was used. An estimated uncertainty of 4 pixels was considered for crown diameter measurements. The value of crown diameter measurement uncertainty was estimated to be ± 12 μm.

In the case of film thickness measurement, the National Instrument vision assistant was used. The magnification used was of 2.9 $\mu m/pixel$ providing a resolution of 2.2 μm in film thickness measurement if the refractive indexes of ZnSe and HFE-7100 were taken as deterministic. An uncertainty of 4 pixels was considered for crown diameter measurements. The value of film thickness uncertainty was estimated to be $\pm$ 4.5μm.

J. Droplet Diameter Measurement and Uncertainty Analysis

The Image Analysis Tool from National Instruments was used to measure the projected vertical surface area of each droplet which in turn was used to compute droplet diameter (see Equation (3.1)). A scale of $1.5\mu m/pixel$ was used for these measurements. The estimation of the diameter measurement uncertainty as follows:

$$u_{d_d} = \frac{\partial d_d}{\partial A} u_A \tag{3.28}$$

Applying equation (3.28), the uncertainty for droplet diameter measurement was found to be $\pm$ 7.5μm.

K. Droplet Velocity Measurement and Uncertainty Analysis

Droplet velocity was calculated according to Equation (4.6), in which L is the distance between droplets in micrometers and f is the input frequency from the function generator.

Measurements of distance between droplets were performed at a magnification of 4.5 $\mu m/pixel$ with a corresponding uncertainty of $\pm$20 μm. Frequency uncertainty from signal generator (BK Precision Model 4011A) was $\pm 10Hz$. Uncertainty on velocity measurements was then given by:

$$u_{v_d}^2 = \left(\frac{\partial v_d}{\partial L} u_L\right)^2 + \left(\frac{\partial v_d}{\partial f} u_f\right)^2 \tag{3.29}$$

Application of Equation (3.29) resulted in a velocity measurement uncertainty of $\pm$ 0.14m/s.

CHAPTER IV

RESULTS AND DISCUSSIONS

This Chapter presents the experimental results obtained in this research effort. First, droplet characterization data are given. Heat transfer results including critical heat flux measurement for single and multiple streams are included. Characterization data of the liquid film formed by droplet impingement impact with and without heat transfer are given including film thickness and size of the crown formed by droplet impact. A parametric study of the effects of Weber number (relation of inertial and surface tension forces), and Strouhal number (dimensionless frequency) are presented for the case of single stream.

A. Droplet Stream Results

Before running heat transfer experiments, the stream of droplets was characterized to ensure a monodispersed stream was being produced by the piezo-electric droplet generator. Also, droplet diameter, d_d, as well as the drop velocity, v_d, were measured experimentally.

Limitations to the production of a monodispersed stream of droplets are first given by the ability to form a jet at the orifice plate outlet. A minimum velocity is necessary to form a jet which has been investigated before [100] and, it is expressed by equation (4.1). In the case of HFE-7100, the lower limit of velocity from the jet is 0.7 m/s which is obtained with 43 ml/hr. In this research work, the lower limit of jet velocity is given by heat transfer demands of the heater to avoid dry-out conditions.

$$v_{j,min} = \left(\frac{8\sigma}{\rho d_j}\right)^{1/2}; \tag{4.1}$$

Once that a stable jet is obtained, there is a range of imposed disturbance frequencies (based on Rayleigh droplet break up theory) that induce well-spaced mono-sized droplets. For a stream of droplets produced by the Rayleigh droplet breakup, Schneider et al. [101] presented empirical results for water of a range of disturbance frequencies (equation (4.2)) that would generate monodispersed stream of droplets.

$$\frac{v_j}{2.0(\pi d_j)} < f < \frac{v_j}{1.1(\pi d_j)}; \tag{4.2}$$

Schneider relationship (4.2) was used as a first reference in determining experimentally the range of operating frequencies that would allow the formation of monosized droplet for each flow rate. The actual range of frequencies in which monodispersed droplets were found are shown in Figure 15 for the case of single and triple streams using an orifice of 150 μm and HFE-7100 as a fluid instead of deionized water. High speed imaging did confirmed that well-spaced monosized droplets were being generated when using disturbance frequencies between 2.2 and 13 kHz at different flowrates, as described below.

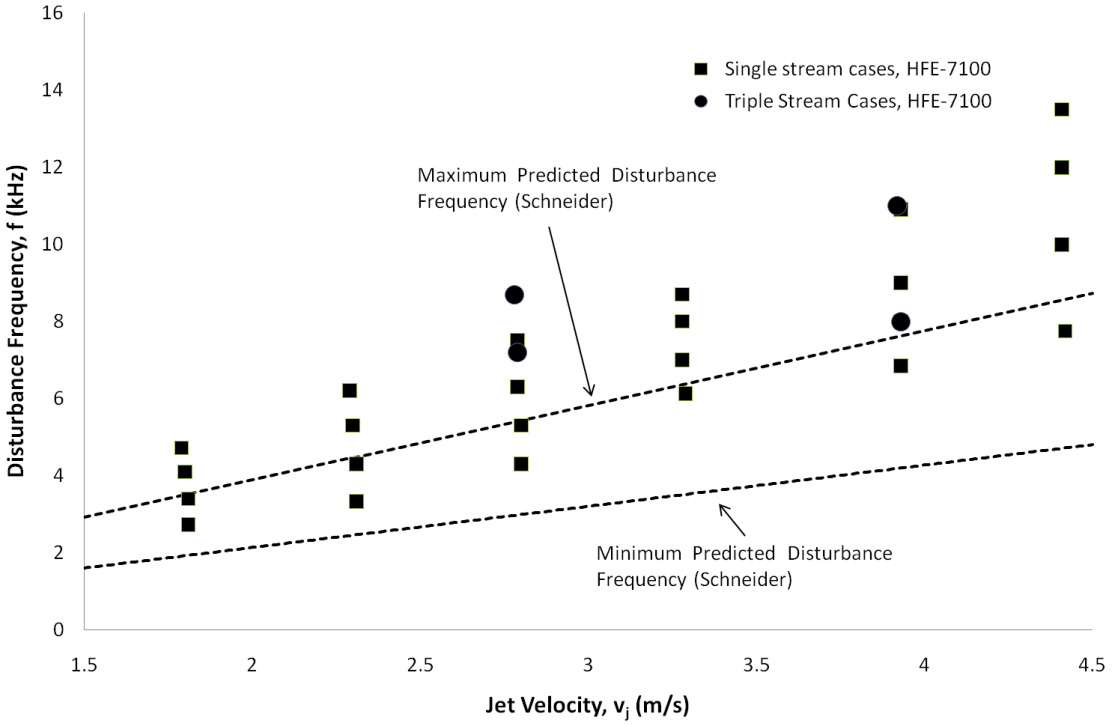

Fig. 15.: Disturbance frequencies range

Measurements of droplet diameter and velocity were performed next. First, images of the droplets were obtained with the high speed camera using backlight illumination at the proximity of the heater surface. A code using the Particle Image toolbox of the Image Analysis Tool from National Instruments was used to measure the projected vertical surface area of each droplet which in turn was used to compute droplet diameter. A magnification of 1.5 μm/pixel was used for droplet measurement with a corresponding uncertainty value of ± 7.5 μm in diameter [99]. These values were compared to the theoretical diameter values given by equation (4.3) for the case of 180 ml/hr in Table VI

$$d_d = \left(\frac{6Q''}{\pi f}\right)^{(1/3)}; \tag{4.3}$$

Table VI.: Diameter measurement case 180 ml/hr

Flow (ml/hr)	Frequency (Hz.)	d_d Eq(4.3)μm	d_d exp μm	% diff
180	4,300	281	269	4.4 %
180	5,300	262	249	5.3 %
180	6,300	247	236	4.9 %
180	7,500	233.5	220	6.1 %

Also, images of the orifice plates to be used during the experiments were characterized using a Unitron MEC2 microscope series to make sure it had the right size, shape and relative low roughness to ensure proper droplet formation. The images were processed to obtain diameter of the orifice plate using Micrometrics SE Premium version 2.9. The diameter of the jet was taken to be equal to the diameter of the orifice plates used which was later confirmed by high speed imaging. The jet velocity for each experimental condition was determined using equation (4.4) once the mass flow rate from the orifice, $\dot{m}$, and the jet diameter, d_j were known:

$$v_j = \frac{4\dot{m}}{\pi\rho d_j^2}; \tag{4.4}$$

Equation (4.5) is derived based on the energy balance taking place before and after the breakup of droplets in flight. Initial droplets velocities were calculated using

Equation (4.5). Velocities obtained using Equation (4.5) were compared with the measured velocities obtained by measuring the distance between droplet and multiplying it by the input frequency using (4.6). Measurements of distance between droplets were performed at a magnification of 4.5 μm/pixel with a corresponding uncertainty of $\pm$ 20 μm. Measurements of input frequency had an uncertainty of $\pm$ 10 Hz. The associated uncertainty with the velocity measurements was about $\pm$ 0.14 m/s [99]:

$$v_d = \left(v_j^2 - \frac{12\sigma}{Dens \ * \ d_d} \right)^{1/2}; \tag{4.5}$$

$$v_d = (Lf); \tag{4.6}$$

The effect of drag on droplet velocity at the point of impact have been shown [102] to be very low for closely spaced, monodispersed droplet streams (spacing less than 4 droplets diameters). All of the monodispersed stream tested in this research work fits on the category of closely spaced, monodispersed droplet streams. As a consequence, the initial droplet velocity is relatively similar to the impact velocity as shown on Table VII.

Table VII.: Velocity measurement

Flow (ml/hr)	Frequency (Hz.)	v_d Eq(4.5) m/s	v_d Eq(4.6) m/s	% diff
180	4,300	2.80	2.90	3.6 %
180	5,300	2.80	2.70	3.6 %
180	6,300	2.79	2.83	1.4 %
180	7,500	2.79	2.85	2.1 %

The difference of theoretical and experimental results on droplet diameter and velocity is below 10%. A source of error on the experimental measurement could be the use of a 250 W-lamp as a source of backlight illumination that could cause a higher rate of evaporation of the stream of droplets on flight. For the remainder of this dissertation theoretical values calculated using equations (4.3) and (4.5) will be used as shown in appendix B and C.

B. Heat Transfer Results

The goal of the investigation was to measure surface temperature at a given heat flux inside the crown formed by the impingement of droplets for single and triple stream cases. Also, the maximum or critical heat flux (CHF) for a given set of parameters was measured.

1. Individual Stream Results

At the beginning of each heat transfer experiment, the top surface of the heater was cleaned using isopropyl alcohol and deionized water. The surface was then dried using

a pressurized duster containing tetrafluoroethane. The head of the droplet generator was positioned in the Z direction (completely vertical) using a manual XYZ positioner at approximately 5 cm from the surface of the heater. Power was applied with a Lambda GEN 600-2.6 DC power supply. The voltage across the heater was increase in small steps until reaching a steady state temperature of approximately 30 ℃ which was recorded using the infrared camera.

After this step, the droplet stream was initiated and visually centered on the heater surface using a manual XYZ positioner. At this point, humidity and ambient temperature were monitored and recorded using a humidity temperature meter. Surroundings temperature was monitored using a thin film type T thermocouple attached to the surface of the holder of the heater that was connected to the data acquisition system (DAQ). Surface temperature was monitored at a region of interest within the surface of the heater. Once the surface of the heater reached a steady temperature value, 199 images at a frequency of 60 Hz. were recorded using the infrared camera and corresponding software. The corresponding value of power supplied, relative humidity, ambient temperature and surface temperature were used to calibrate IR temperature values and to determine heat transfer rate.

The power supplied was incremented, surface temperature was constantly monitored to ensure the integrity of the heater. The power supplied neat the critical heat flux, CHF, was incremented in small steps of less than $1 W/cm^2$. The power supplied to the heater was stopped once the CHF conditions were reached. CHF was easily recognized by the non-wetting behavior of the fluid hitting the surface (see Figure 16), and a sudden increase in surface temperature. The CHF was defined as the maximum heat flux for which a thin film of fluid could be sustained on the surface of the heater. After reaching CHF and shutting down the heater, images of the droplet stream were taken in order to ensure that the stream was still stable and monodispersed.

Fig. 16.: Start of critical heat flux

Heat flux, and surface temperature data collected during heat transfer experiment were further processed. Heat flux data was adjusted to take into account conduction heat transfer losses through the holder, and natural convection from the bottom of the heater. Surface temperature was determined based on the average of 199 readings.

Figure 17 shows heat transfer results for the cases when individual droplet stream impinge on the surface. In the abscissa, the average minimum temperature for each case is presented. In the ordinate, the corrected heat flux value. The cases plotted shown were for flow rates ranging from 120 to 280 ml/hr. Weber number was varied from 87 to 598, while the Strouhal number is on 0.415 to 0.680 range. However, the maximum variation of Weber number at a fixed flow rate was 103 at a flowrate 280 ml/hr; on the other hand, the variation of Weber number at 120 ml/hr was 20. One point worth noting on Figure 17 is that heat transfer behavior is primarily a function

of flowrate showing that an increase in slope in the heat flux vs. minimum wall temperature graph correlates well with flow rate (or number of same sized droplets per unit time). From Figure 17 , Weber and Strouhal number do not have a clear effect on heat transfer behavior when comparing within the same flowrate.

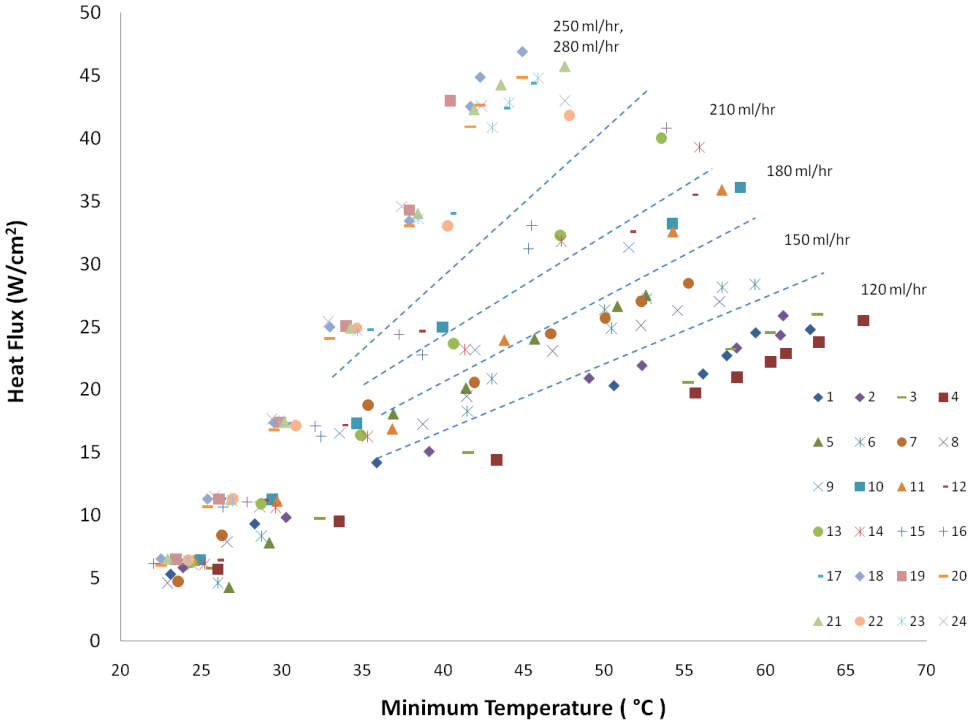

Case	Flow rate ml/hr	Weber	Strouhal	Case	Flow rate ml/hr	Weber	Strouhal
1	120	96.5	0.454	13	210	315.7	0.498
2	120	89.7	0.525	14	210	302	0.544
3	120	84.3	0.595	15	210	288.9	0.594
4	120	80.4	0.654	16	210	281	0.628
5	150	165	0.430	17	250	466	0.472
6	150	151.6	0.508	18	250	442.5	0.524
7	150	141.4	0.584	19	250	425	0.567
8	150	134.2	0.649	20	250	399	0.644
9	180	242	0.441	21	280	588	0.473
10	180	225.7	0.508	22	280	540	0.561
11	180	213	0.568	23	280	508.3	0.634
12	180	201	0.639	24	280	489	0.685

Fig. 17.: Heat transfer results

Only cases at 120 ml/hr exhibited maximum minimum temperature above the saturation temperature of HFE-7100 at atmospheric temperature (61 ℃) before reaching CHF. For all the other cases, the maximum minimum temperature was below saturation temperature congruent with single phase cooling which is suspected to be the main heat transfer mechanism at those flowrates.

Figure 18 shows cross-sectional temperature profiles in the case of a single droplet stream at 120 ml/hr, droplet frequency of 2,730 Hz, Weber number of 107.5 and Strouhal number of 0.430 impinging the heater surface. The temperature profile is an average of 199 IR frames from the infrared camera of a line crossing through the impact zone in a direction normal to the direction of the flow. The impact point of the droplet coincides with the radial origin and with the lowest surface temperature.

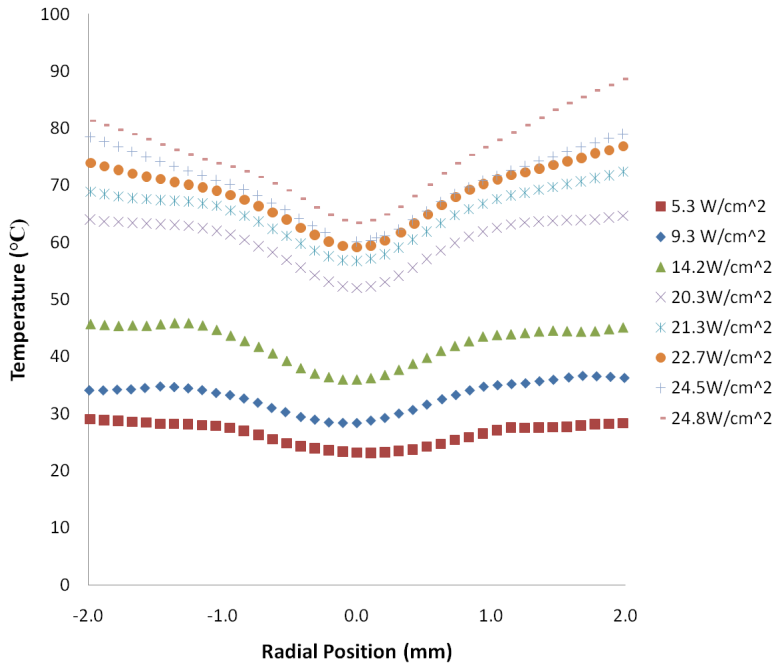

Fig. 18.: Temperature profile 120 ml/hr, We=107.5, St=0.430

Figure 19 shows the case of a single droplet stream at 280 ml/hr, 13,500 Hz., Weber number of 495, and Strouhal number of 0.681. Common features of these cases (Figure 18 and Figure 19) include an increase of the temperature gradient (slope) with respect to the point of impact at higher heat fluxes. Also, a significant reduction in the size of the thermal impact zone (i.e. impact crater) at higher heat fluxes is observed.

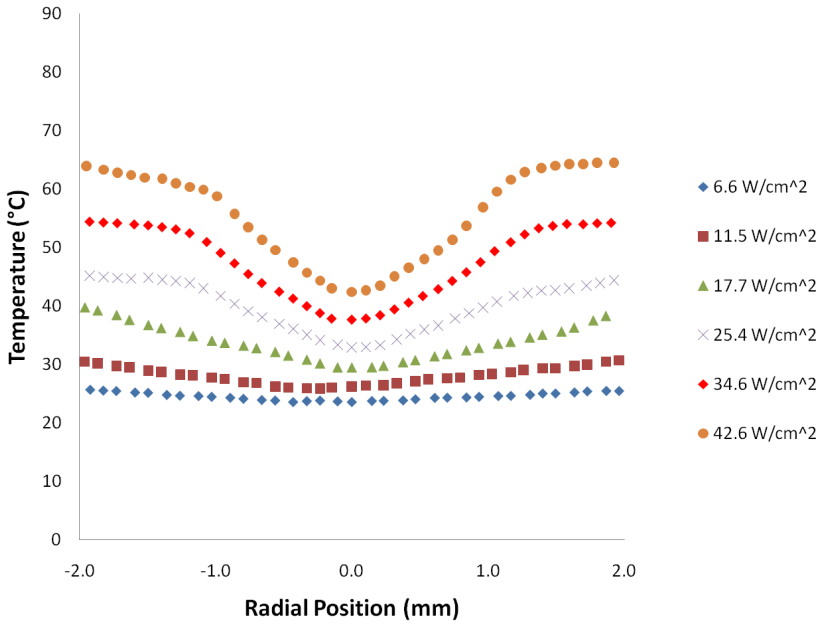

Fig. 19.: Temperature profile 280 ml/hr, We=495, St=0.681

As part of the heat transfer experiments, the high speed imaging system was used to observe impact of the droplets on the heater under three different heat flux conditions, namely: no heat flux, low heat flux, and high heat flux. Low heat flux was on the order of 8 to 9 W/cm^2 after taking into account heat losses and illumination. The condition of high heat flux was chosen to be near the point of CHF at 25 W/cm^2 in the case of a flowrate of 120 ml/hr to 43 W/cm^2 in the case of a flowrate of 280 ml/hr. The purpose of the high speed imaging visualization was to observe impingement phenomena at the proper time scale given the high frequency of droplet impingement, and to identify the corresponding impact regimes (i.e. spreading or splashing).

Figure 20 shows images of the impact of a single droplet stream with a flow rate of 120 ml/hr, 2,730 Hz. It is possible to see a smooth spreading of the droplet with a radially outward expansion of the impact wave in the case of no heat flux (see Figure 20a). In the case of low heat flux, an increment of the height of the surrounding film is seen with the formation of a well defined crown (see Figure 20b). In the high heat flux case (see Figure 20c) shows a further increase on surrounding film height due to bubble formation at the edge of the crown.

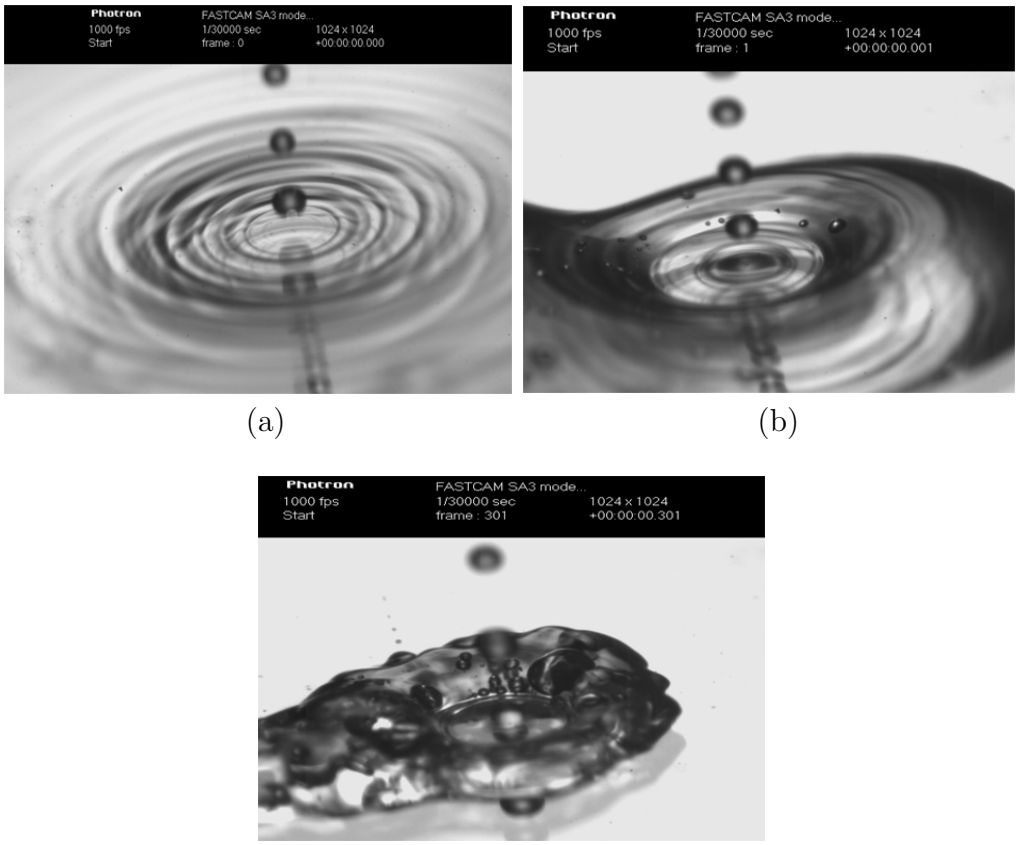

Fig. 20.: Stream impact 120 ml/hr, We=80. a)No heat flux, b) low heat flux, c)high heat flux

Figure 21 presents still pictures of the impact of single stream of droplets at a flow rate of 280 ml/hr with a frequency of 13,500 Hz. At no heat flux, the impact of the droplet is more irregular as compared with lower flowrates and corresponding lower Weber numbers (see Figure 21a). It is also possible to identify some splashing upon impingement of the droplet without a clear formation of a crown or crater zone. In the case of low heat flux a small increment of the height of the surrounding film is observed and the formation of the crown becomes clearer than in the case of no heat flux (see Figure 21b). The high heat flux case (see Figure 21c) shows a clearer crown

formation with an increase of height of the surrounding film. Bubble formation at the edge of the crown formation is also observed but not as clear as in lower flowrates and Weber numbers.

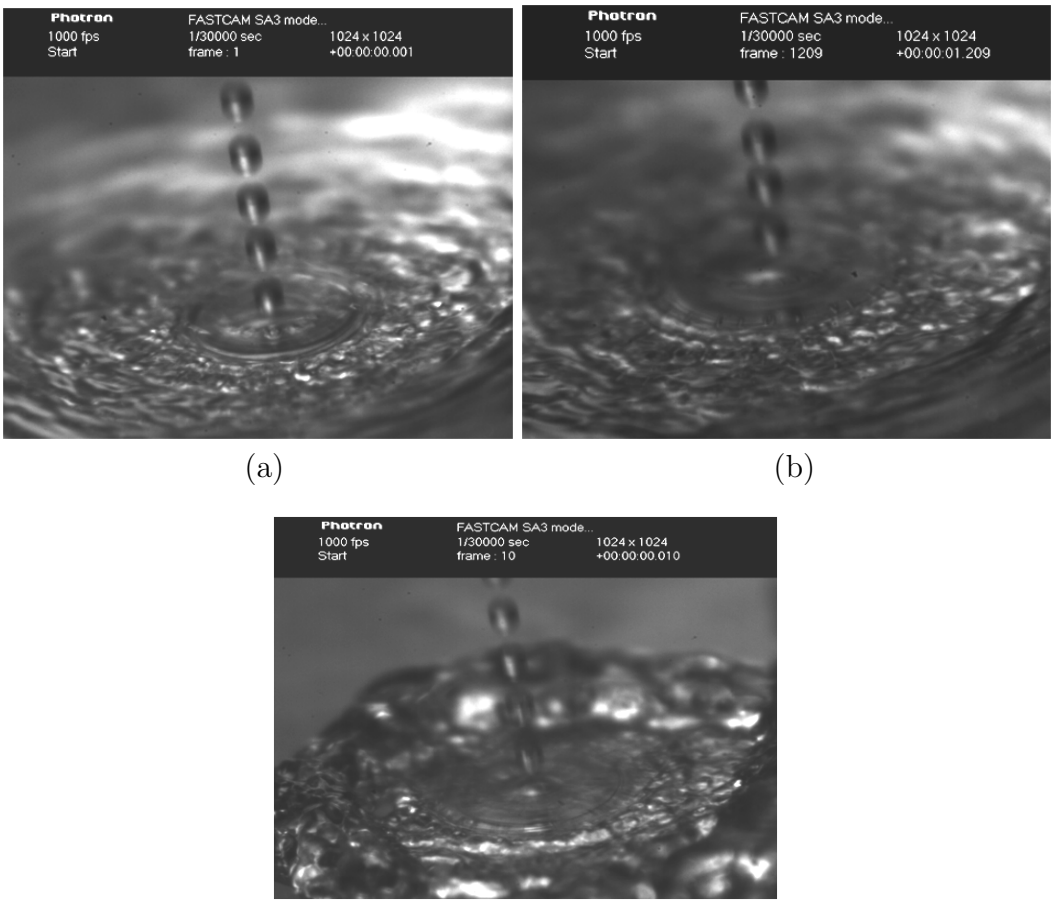

Fig. 21.: Stream impact 280 ml/hr, We=489. a)No heat flux, b) low heat flux, c)high heat flux

2. Triple Stream Results

As part of the study, the effect of adjacent droplet impingement on heat transfer was also investigated. Research in the area of single droplet impingement to date has not considered the effects of droplet impingement spacing which is fundamentally important in the understanding of the physics of spray cooling. For this study, coherent and simultaneous triple droplet impingement was characterized to understand its effects on surface cooling.

In the case of triple streams experiments, the experimental procedure was similar to the one followed with single streams. One main difference was that the head of the droplet generator was positioned in the Z (vertical) direction using a manual XYZ positioner at approximately 2.5 cm from the surface of the heater instead of 5 cm. The reason was that the droplet streams separated 800 μm from each other becomes unstable at higher heights. Also, due to the higher flow rates involved in these experiments, each experimental run required at least two consecutive experiments due to the limited volume capacity of the syringe pump.

Figure 22 shows heat transfer results where triple streams impinges the heater surface at a 540 ml/hr flowrate. The range of droplet frequencies is from 7,200 to 8,700 Hz. In the cases tested the Weber number varies from 197 to 211. The Strouhal number variation is from 0.611 to 0.705. The spacing between droplets shown was 400, 800 and 1,500 μm. Maximum heat flux attainable ranges from 47 to 67 W/cm^2.

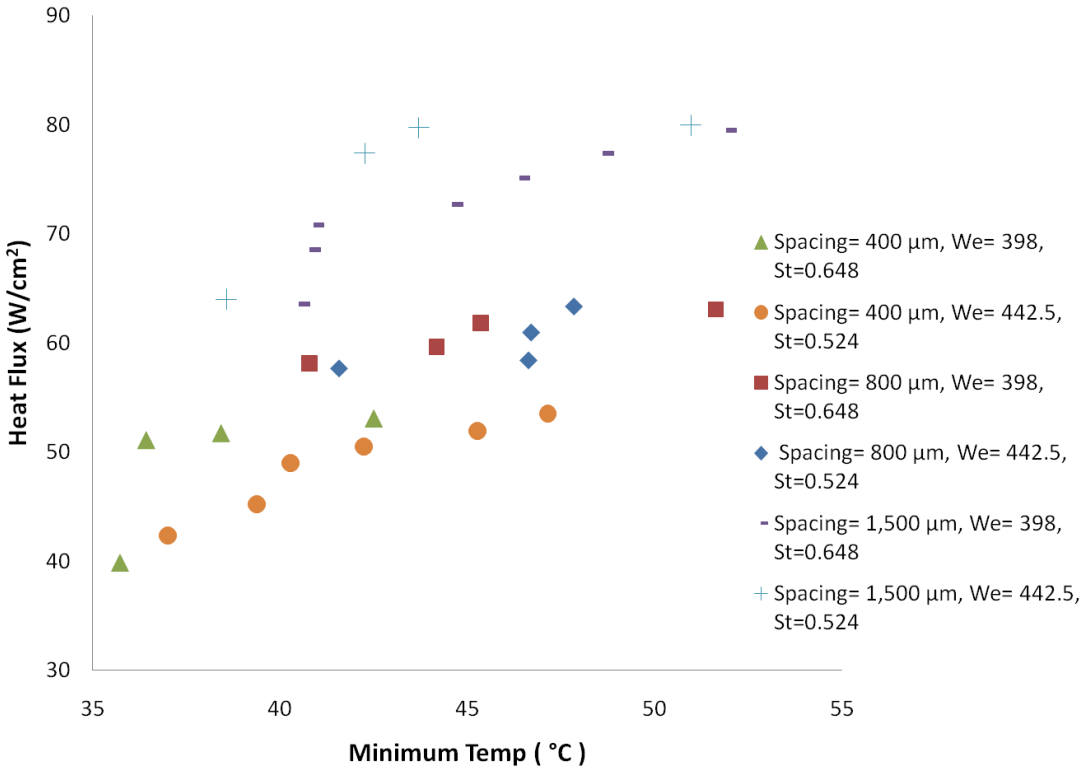

Fig. 22.: Heat transfer results triple streams at 540 ml/hr at different separation values

Figure 23 shows heat transfer results where triple streams impinged the heater surface at a flowrate of 750 ml/hr. The droplet frequencies were varied from 8,000 to 11,000 Hz. In the cases tested, Weber number was varied from 404 to 452. The Strouhal number variation was between 0.519 and 0.643. The spacing between adjacent droplets were 400, 800 and 1,500 μm. Maximum heat flux was between 56 and 82 W/cm^2 for triple streams only.

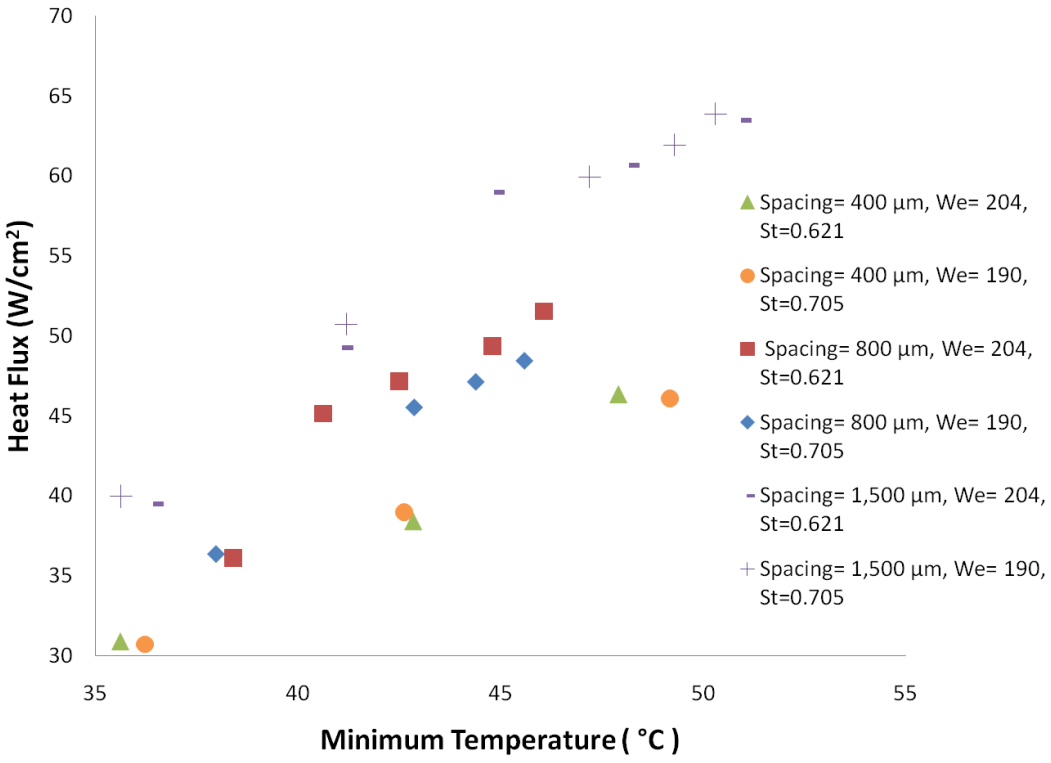

Fig. 23.: Heat transfer results triple Streams at 750 ml/hr at different separation values

One feature worth noting in Figure 17 and Figure 23 is that heat transfer behavior is a strong function of droplet spacing. In both cases (Figures 17 and 23) heat flux increased and surface temperature decreased with droplet spacing. Weber and Strouhal number did not exhibit any significant effect on heat transfer behavior.

All the triple stream cases exhibited maximum minimum temperature below the saturation temperature of HFE-7100 (61℃) at atmospheric temperature (22℃) before reaching CHF which is consistent with single phase cooling as the main heat transfer mechanism at those flowrates.

Figure 24 shows cross-sectional temperature profiles at a droplet impingement

frequency of 7,200 Hz, with Weber number of 211 and Strouhal number of 0.611 impinging the heater surface. The spacing between droplets was 400 μm. The temperature profile consisted of the average of 199 IR frames of the impact zones of the three droplet stream in a direction normal to the direction of the flow, with the center of the central stream coincident with the origin. At this separation of the collinear streams, the temperature profile was almost flatten in the middle which made difficult to identify the impact zone of each stream from the graph at low heat flux values.

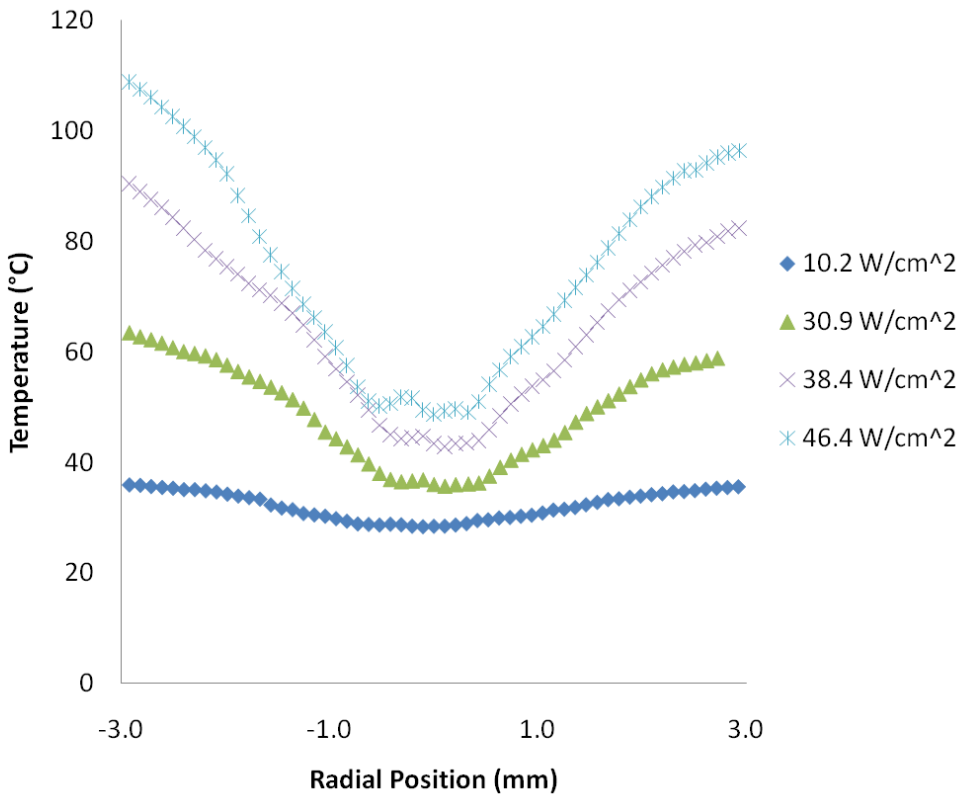

Fig. 24.: Temperature profile triple stream at 540 ml/hr, We= 211, St=0,611, and spacing= 400 μm

Figure 25 shows cross-sectional temperature profiles when droplets impinged at a frequency of 7,200 Hz., Weber number of 211 and Strouhal number of 0.611 impinging the heater surface. The spacing between droplets was 800 μm. At this separation, it was possible to identify the impact zones of each droplet stream at higher heat fluxes. Also, a reduction of the size(crown diameter) of impact zone temperature profile at higher heat fluxes is noticeable.

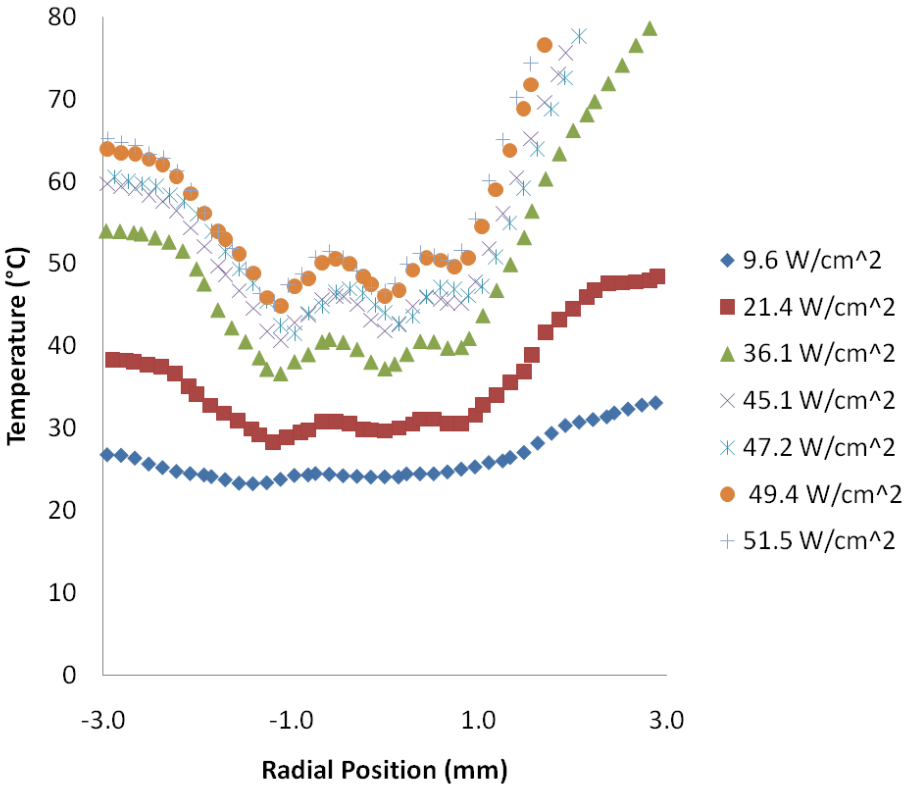

Fig. 25.: Temperature profile triple stream at 540 ml/hr, We= 211, St=0.611, and spacing= 800 μm

Figure 26 shows cross-sectional temperature profiles at 7,200 Hz., Weber num-

ber of 211, and Strouhal number of 0.611. The spacing between droplets was 1,500 μm. At this separation, the impact zone of each droplet stream are easily identifiable even at low heat fluxes. It is worth noting that the right stream exhibits a higher temperature than the middle and left stream due to its proximity to the dry zone of the heater.

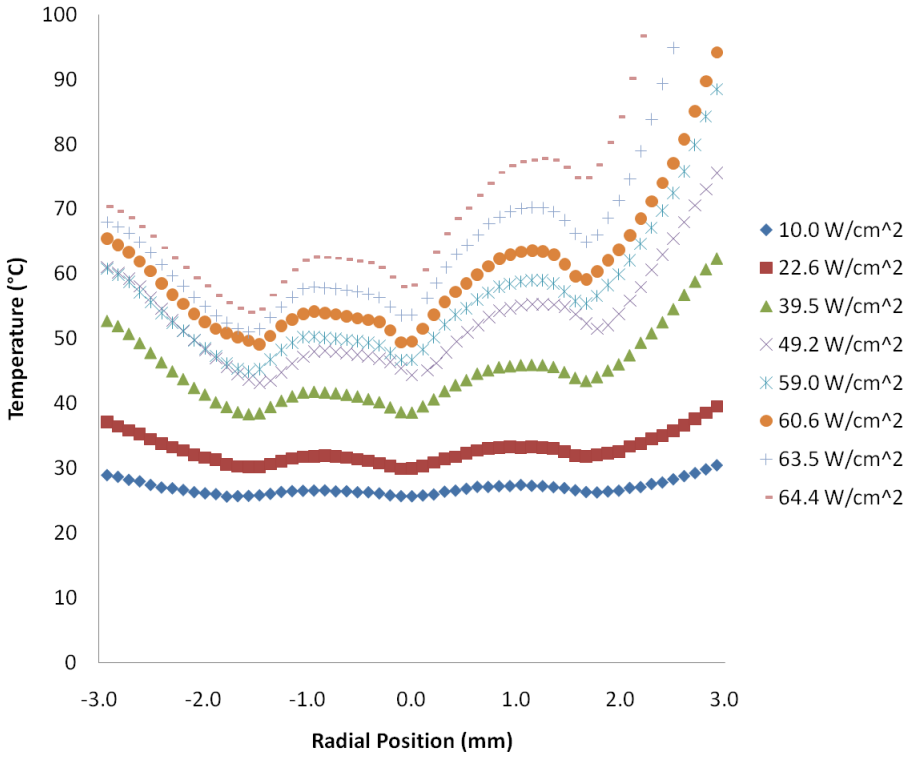

Fig. 26.: Temperature profile triple stream 540 ml/hr, We= 211, St=0.611, and spacing= 1,500 μm

High speed images were taken to observe droplet impingement on the heater under three different heat flux conditions and spacings. The high speed camera was

positioned at a 30 ° with respect to the horizontal. The condition of low heat flux on the order of 20 W/cm^2 with effects of the lamp and heat losses taken into account. The high heat flux was near the point of CHF or about 45 W/cm^2 in the case of a flowrate of 540 ml/hr with droplet stream spacing of 400 μm, and 65 W/cm^2 in the case of a flowrate of 540 ml/hr with droplet stream spacing of 1,500 μm. The purpose of this visualization was to observe impingement phenomena, interaction between droplet streams and identify the corresponding impact regimes.

Fig. 27.: Droplet stream impact at 540 ml/hr, spacing = 400 μm with no heat flux

Figure 27 shows an image of the impact of a triple streams of droplets with a total flow rate of 540 ml/hr, 7,200 Hz., Weber number of 211 and Strouhal number of 0.611, with a separation between streams of 400 μm. Splashing and formation of secondary droplets upon impact was observed (see Figure 27) even in the case of no heat flux.

When the spray is too dense as in the case of droplet spacing of 400 μm, there is not enough space for crowns to develop and small secondary droplets are generated by the breakup of finger-like jets emerging from the film [103]. In this case, the fluctuation of pressure produced film fluctuations which caused the breakup of jets as explained by Roisman et al. [103]. The characteristic velocity and length fluctuations determine the velocity and size of secondary droplets. This case of minimum droplet stream separation exhibits the worst performance from the heat transfer perspective viewpoint.

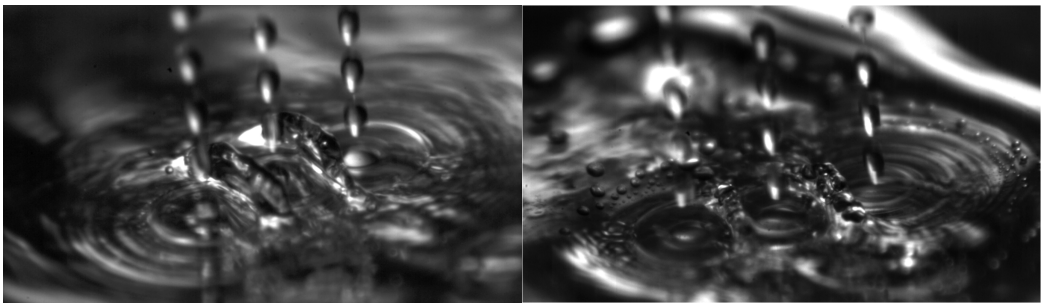

(a) (b)

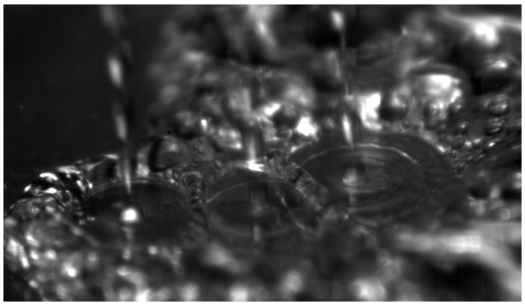

(c)

Fig. 28.: Stream impact at 540 ml/hr, spacing=800 μm. a)no heat flux, b) low heat flux, c)high heat flux

Figure 28 shows images of the impact of triple droplet streams at a total flow rate of 540 ml/hr, 7,200 Hz, Weber number of 211, and Strouhal number of 0.611, with a separation between streams of 800 μm. In all the three cases namely: no heat flux (Figure 28a), low heat flux (Figure 28b), and high heat flux (Figure 28c); it is possible to see three distinct impact craters with accumulation of fluid and formation of ridges with a height several times larger than the droplet diameter. No secondary droplets or splashing can be seen in these cases. In this case, heat transfer exhibits a better performance when compared to the case of smaller separation between droplet streams.

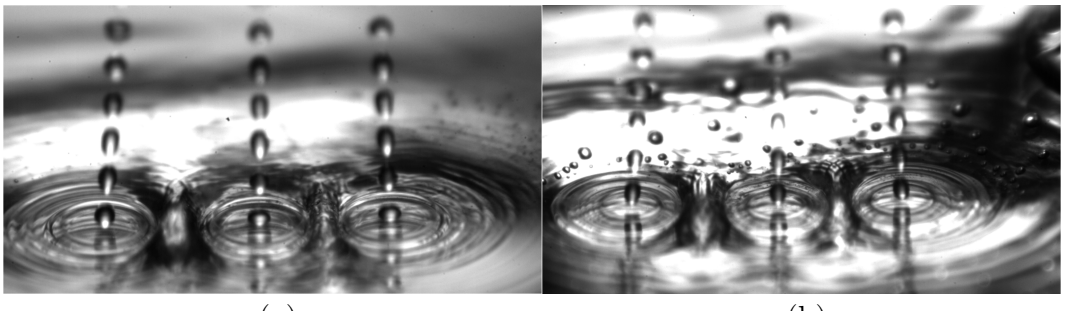

(a) (b)

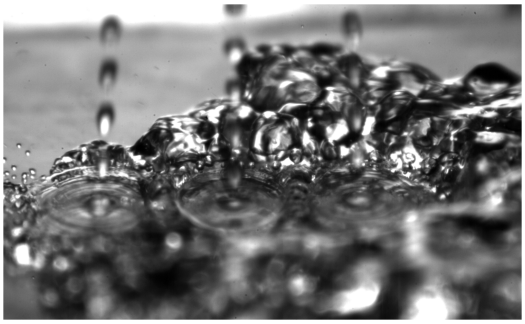

(c)

Fig. 29.: Stream impact 540 ml/hr, spacing=1,500 μm. a)no heat flux, b) low heat flux, c)high heat flux

Figure 29 shows images of the impact of a triple streams of droplets with a total flow rate of 540 ml/hr, 7,200 Hz., Weber number of 211 and Strouhal number of 0.611, with a separation between streams of 1,500 μm. In all the three cases namely: no heat flux (Figure 29a), low heat flux (Figure 29b), and high heat flux (Figure 29c); droplet spreading upon impact and a clear crater formation can be seen in each droplet stream. This case exhibits the best heat transfer performance of all triple stream cases.

In summary, separation (spacing) between adjacent droplets plays a significant role on film dynamics and surface heat transfer. It appears that crown formation should not be disturb to achieve high heat flux rates. Moreover, optimal separation ($1,500\ \mu m$) allows for proper formation of each impact crown while ensuring enough fluid is in contact with the surface to provide sufficient cooling.

C. Visualization and Film Thickness Results

The high speed imaging system was used to obtain horizontal images of the droplet impact zone by placing a 45 degree mirror below the heater and illuminating the heater from above. Figure 30 shows a high speed image obtained with this approach for a single stream case at 180 ml/hr, 5,300 Hz, Weber number of 235, and a high heat flux near to the CHF. Images were taken at a speed of 60 frames per second (fps), the light source was located far from the heater with little effect on heat flux values. An 0.5 X attachment was mounted on to the magnification lens of the camera, with a working distance 175 mm which gave a magnification of 5.88 $\mu m/pixel$. The value of crown diameter measurement uncertainty was calculated to be $\pm$ 24 μm.

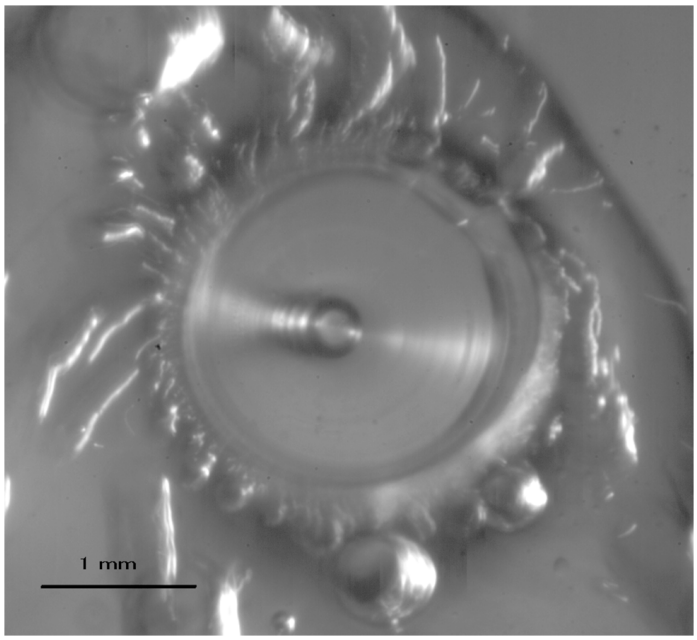

Fig. 30.: Image of crown formation from below

Table VIII gives values of an average diameter of the crown diameter. At low flow rates, below of or equal to 210 ml/hr, it was possible to observe a crown formation at all heat flux values. On regimes where splashing was observed, above of 210 ml/hr, it was only possible to identify a crown formation at high heat fluxes. From the measurements, it was possible to detect an increase in crown diameter with flow rate. A decrease in crown diameter with heat flux was also observed. The reduction is crown diameter with heat flux can be attributed to two main factors: the vigorous boiling process taking place outside the impact crown (i.e. greater inertia forces versus surface tension forces) and thin film evaporation. Both mechanisms can only be explained better by knowing the effect of heat flux on crown film thickness.

Table VIII.: Single stream crown diameter (μm)

Heat flux (W/cm^2)	Crown diameter (μm)					
	120 ml/hr	150 ml/hr	180 ml/hr	210 ml/hr	250 ml/hr	280 ml/hr
0	1,898	2,145	2,349	2,710	3,176	na
9.5	1,357	1,573	1,826	2,038	na	na
27	1,015	1,194	1,403	1,616	2,114	2,066
32	-	1,109	-	-	-	-
37	-	1,227	1,450	1,729	1,896	
40	-	-	-	-	1,605	1,798

In the case of triple droplet streams, the formation of each crown is dependent on the spacing between adjacent droplet streams. Figure 31 shows high speed images for the case of a separation between droplets of 400 μm which corresponds to a dense spray case. In this situation, it is not possible to observe crown formations for all individual streams. However, it is possible to observe a thin film area surrounded by a larger crown at higher heat flux values. Nevertheless, triple streams separated at 400 μm exhibit poorer heat transfer performance than at greater spacing.

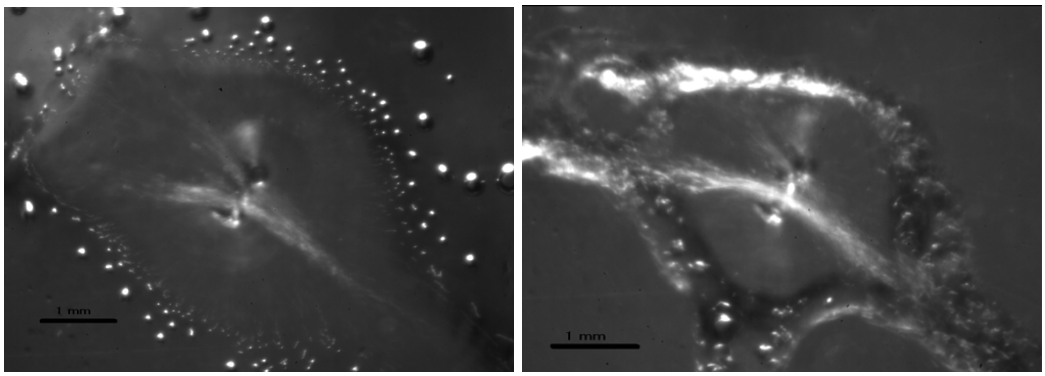

(a) (b)

Fig. 31.: Triple stream visualization at flow rate of 540 ml/hr, separation between droplets of 400 μm. a)low heat flux (10 W/cm^2), b) high heat flux (45 W/cm^2)

Figure 32 shows high speed images where spacing between adjacent droplet streams is $1,500$ μm which corresponds to a sparse spray case. At this separation, the interaction between adjacent droplets diminishes allowing individual and distinct crown formations. As in the case of individual droplet streams, the diameter of each crown reduces with heat flux. It is worth noting, that the middle crown stream shows an elliptical shape due to the effects of the adjacent droplet induced crowns.

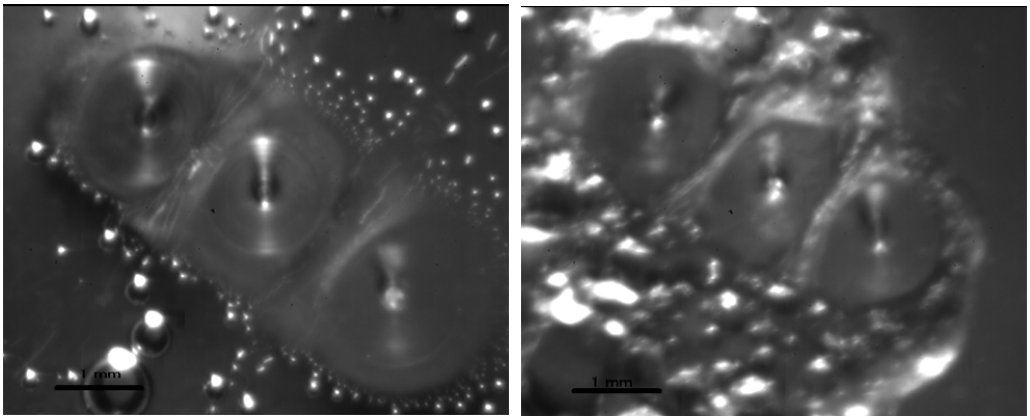

(a) (b)

Fig. 32.: Triple stream visualization at flow rate of 540 ml/hr, separation between droplets of $1,500\ \mu m$. a)low heat flux ($10\ W/cm^2$), b) high heat flux ($55\ W/cm^2$)

Film thickness measurements were obtained using a light diffraction technique as previously discussed in Chapter III. The camera speed was set to 60 frames per second (fps) with a shutter speed of $1/60s$ obtaining a resolution of 3.6 $\mu m/pixel$. The values of refractive index for ZnSe for a wavelength of 532 μm is 2.69. The effect of a thin opaque coating on the bottom of the heater and the ITO coating on top were negligible due to the thin thickness of each layer (in the order of mm for ZnSe, μm for the opaque coating, nm for the ITO coating). The refractive index for HFE-7100 for a wavelength of 589 μm is 1.27.

Previous to each film thickness measurement test, the droplet stream parameters were set to the same values used for heat transfer experiments. The impact of the droplet stream was made to coincide with the center of the ring formed by the refraction of the laser light. The ring had a diameter of 625 μm. This means that all the diameters of light rings obtained were less than the crown formation diameter as shown by Table VIII (i.e. all the values listed in the table are greater than 625 microns).

The technique works well if the refractive index of the fluid above the heater surface is known. This technique is not suitable for applications where air and vapor bubbles are present since the refractive index would not be fixed. From all the high speed images taken it can be concluded that inside the crown formation, no bubbles were present, thus making this technique appropriate for film thickness measurements inside the droplet impact crater.

After the droplets parameters were set and the droplet stream centered, data was collected in the following sequence:

- No heat flux on the surface with center of the laser aligned with point of impact of the droplets.
- Low heat flux of approximately 10 W/cm^2 with center of the laser aligned with point of impact of the droplets.
- High heat flux near the point of CHF with center of the laser aligned with point of impact of the droplets.
- No heat flux on the surface with center of the laser pointing away from point of impact of the droplets. The purpose of this measurement was to obtained film thickness outside the point of impact of the droplets.
- No film on the surface of the heater.

Images of the ring produced by the refraction of the laser beam were obtained with the high speed imaging system which allowed for accurate measurements before, during, and after each impingement event. In the case of dry surface and liquid film outside the droplet impact crown formation only one individual ring structure was obtained as seen in Figure 33.

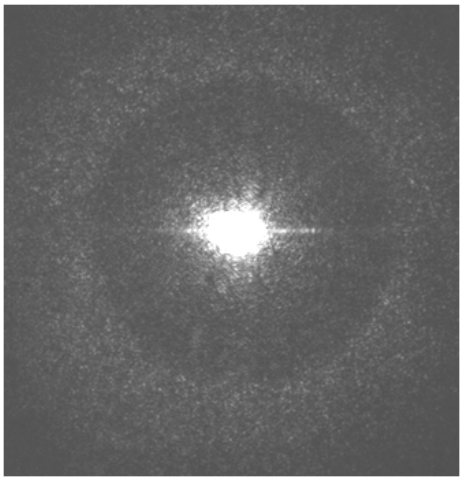

Fig. 33.: Image obtained for a dry heater

When the film thickness measurement was done inside the crown formation, two rings were obtained. This feature could be seen in Figure 34.

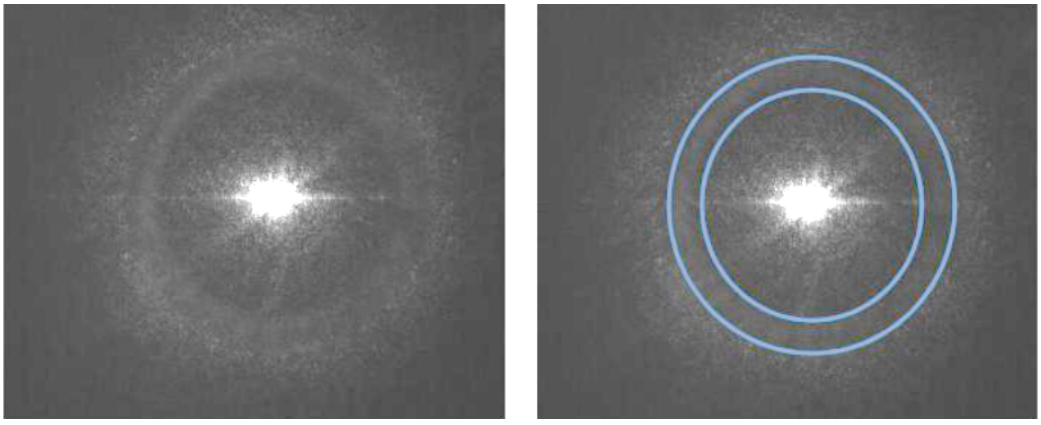

Fig. 34.: Film thickness image for 120 ml/hr, 2750 Hz with 10 W/cm^2

Film thickness was computed from the following equation (4.7) from Pautsch and Shedd[51, 52, 93] :

$$t_{film} = \frac{(0.5R - t_{base}\tan(\theta_{c,13}))}{(\tan(\theta_{c,23}))} \tag{4.7}$$

where $\theta_{(c,12)}$ is the critical angle between mediums 1 and 2. Subscripts 1,2, and 3 denote air, ZnSe, and HFE-7100, respectively.

The measurements were taken at a speed of 60 fps for cases in which droplets impact the surface at rates from 2,730 Hz to 13,500 Hz. Each image is composed of at least 40 droplet impacts which means that the two rings represented the average of minimum and maximum film thickness during the droplet impact process. The maximum film thickness corresponds to the maximum height of the wave crest produced after impact of each droplet with an outward direction inside the crown formation. The minimum film thickness (wave through) corresponds to the height of the film before and after the wave motion. Figure 35 shows film thickness results for the case of no heat flux as a function of Weber number. The different droplet parameters used to obtain the reported Weber number are presented in Appendix B. The value of film thickness varies from 10 *to* 18 μm for minimum film thickness, and a variation of 79 *to* 86 μm for maximum film thickness. There is not a clear tendency of each value as a function of Weber number.

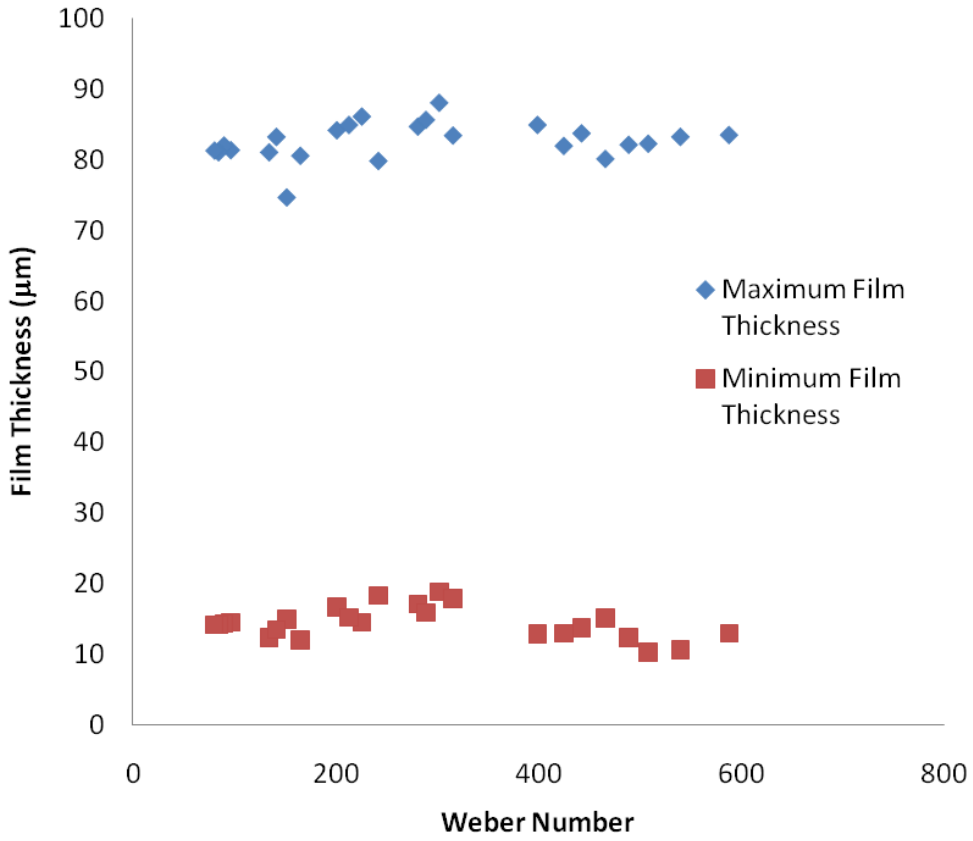

Fig. 35.: Film thickness for no heat flux case

Figure 36 shows film thickness results for the case of low heat flux at approximately 10 W/cm^2 on the heater as a function of Weber number. The value of film thickness varies from 10 *to* 17 μm for minimum film thickness, and a variation of 71 *to* 81 μm for maximum film thickness. There is not a clear tendency of each value as a function of Weber number.

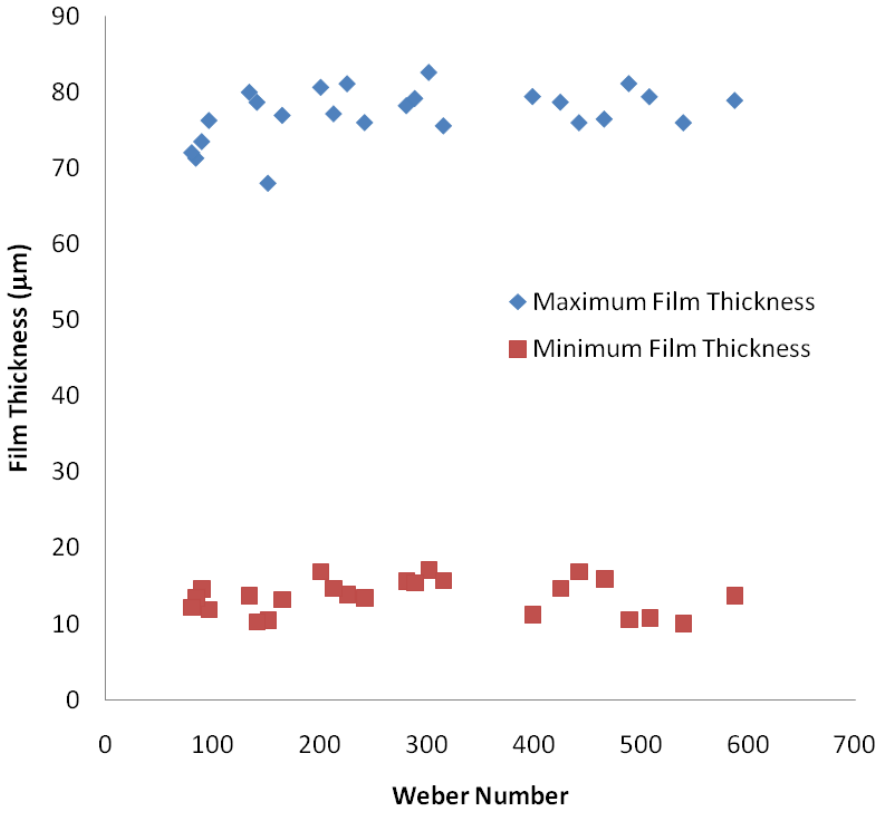

Fig. 36.: Film thickness low heat flux case (10 W/cm^2)

Figure 37 shows film thickness results for the case of high heat flux near the value of CHF, ranging from 25 to 37 W/cm^2, for each droplet stream condition. In this case as in the previous case, data is shown as a function of Weber number. The value of film thickness varies from 7 to 16 μm for minimum film thickness, and a variation of 66 to 75 μm for maximum film thickness. There is not a clear tendency of each value as a function of Weber number though the average value of maximum film thickness decreased with heat flux. Also, there is a small increase in the variation of film thickness with increasing heat flux values. This suggest that thin-film evaporation takes places as heat flux is increased. A variation of standard deviation from 2.68 μm for

maximum film thickness with no heat flux to 3.48 μm for maximum film thickness at high heat flux was found. In the case of minimum film thickness, the variation in film thickness is minimal with a standard deviation of 2.24 μm in the case with no heat flux to 2.39 μm in the case of high heat flux.

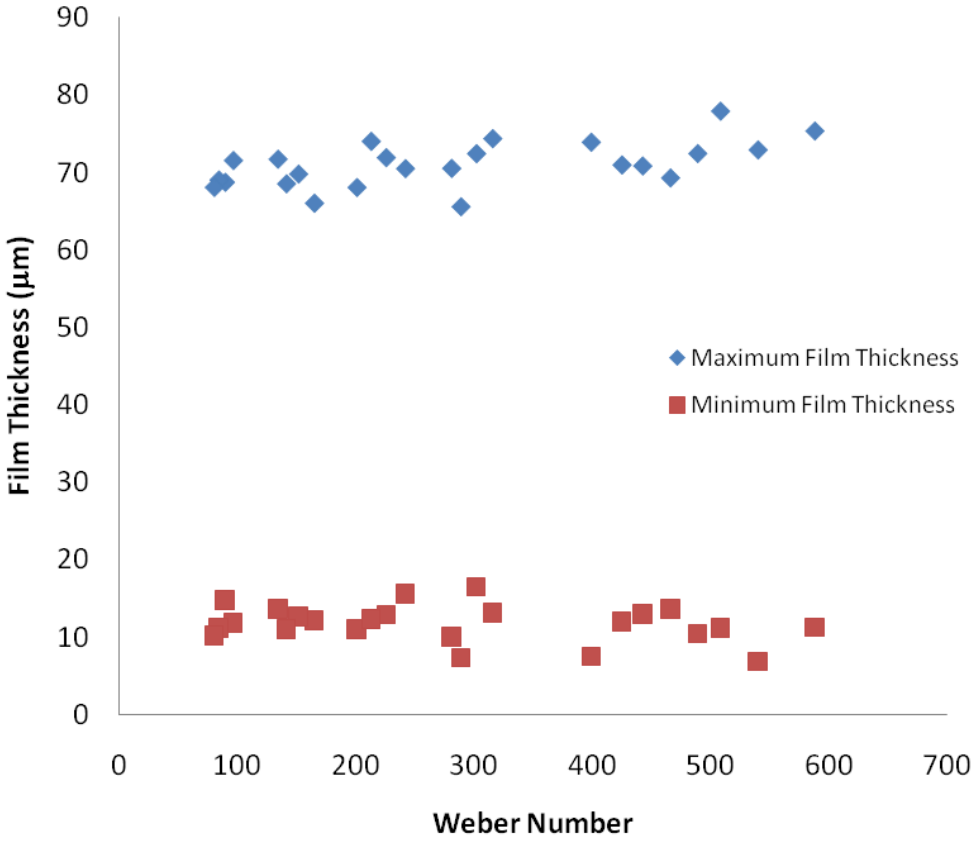

Fig. 37.: Film thickness high heat flux case

Figure 38 shows minimum film thickness for the no heat flux, low heat flux and high heat flux cases. In these cases, it is possible to observe a small reduction in film

thickness height of 2.2 μm from the case of no heat flux to high heat flux which is within the uncertainty of the experimental method used. Thus, it could be concluded that heat flux has little to not effect on minimum film thickness.

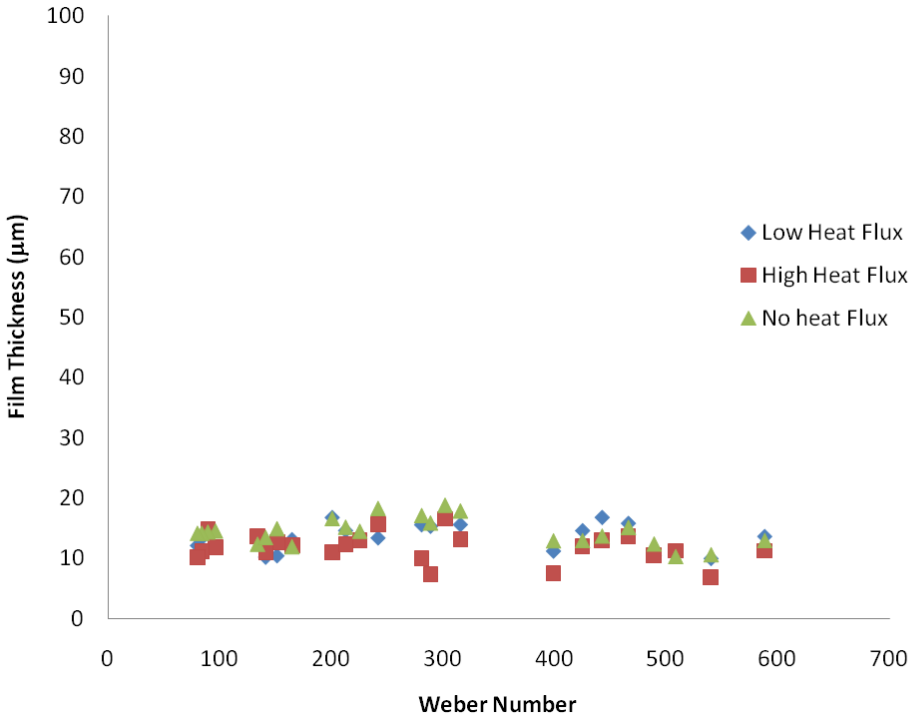

Fig. 38.: Minimum film thickness

Figure 39 shows maximum film thickness for the no heat flux, low heat flux and high heat flux cases. In these cases, it is possible to observe a small reduction in film thickness height of 12 μm which is more that the corresponding experimental uncertainty. The reduction in maximum film thickness may suggest evaporation of the film layer as a possible heat transfer mechanism during the droplet impingement process. However,given the high impingement frequency, low fluid temperature (below satura-

tion temperature), and constant minimum film thickness, thin film evaporation does not seem to account for the reduction in maximum film thickness. The reduction in maximum film thickness can be attributed to a reduction in surface tension at higher heat flux and surface temperature values. The overall heat transfer process seems to be dominated mainly by forced convection during the periodic droplet impingement process.

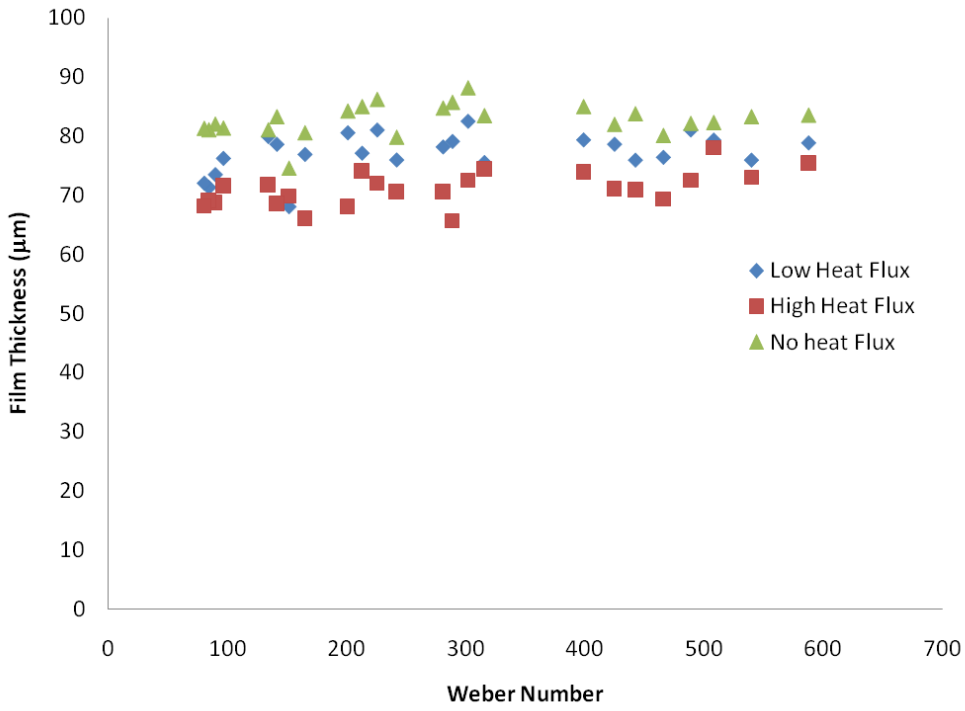

Fig. 39.: Maximum film thickness

D. Parametric Study

Among the objectives of this research project is to study the effects experimental parameters of the droplets trains on hydrodynamic and heat transfer responses upon impingement on the heater surface. Important parameters in monosized droplet streams are namely: droplet diameter, droplet velocity, and frequency; or in dimensionless form: Weber number ($We = (\rho v_d^2 d_d)/\sigma$) to take into account the joint effect of velocity and diameter on inertial forces of the droplet train, Strouhal number ($St = (f d_d)/v$) to account for oscillation effects. The expected outcome of the study is the identification of the effects of these parameter on heat transfer and impinged droplet crown morphology.

Changing parameters such as droplet diameter, droplet velocity and frequency while keeping flow rate constant is physically impossible for droplet generators based on the Rayleigh breakup principle. In this study, two parameters, Weber, and Strouhal numbers were varied to determine their effects on film dynamics and heat transfer. In order to change these parameters, four single-orifice plates with different orifice diameters were used. Orifice plates images were obtained using a Unitron MEC2 microscope and processed with Micrometrics SE Premium version 2.9. The results are presented in Table IX.

Table IX.: Orifice plates characterization

Nominal Diameter (μm)	Measured Diameter (μm)
130	128.7
140	138.7
150	149.
160	157.9

The working range at different flow rates was found experimentally using the Schneider [101] relationship as starting point. Table X provides a range of each variable that could be experimentally obtained with 150 ml/hr and 210 ml/hr of flow rate.

Table X.: Experimental range of We and St as a function of orifice plates diameter

Nominal diameter (μm)	flow rate (ml/hr)	frequency (Hz.)	Weber	Strouhal
130	150	6,160-11,400	212-264	0.46-0.70
130	210	9,300-14,450	442-515	0.48-0.64
140	150	4,700-8,380	172-212	0.45-0.66
140	210	7,400-12,500	342-409	0.48-0.68
150	150	3,335-6,200	141-176	0.41-0.63
150	210	5,500-8,300	292-337	0.46-0.60
160	150	3,780-5,720	112-131	0.51-0.68
160	210	6,000-8,100	232-272	0.49-0.67

Based on the experimental range obtained, experiments at different heat flux

values were performed by changing Weber number and keeping Strouhal number, and flow rate constant. Experiments were performed to study the effect of varying Weber number on surface temperature, and film thickness. Table XI provides the input values for the Weber number experiments.

Table XI.: Experimental conditions for Weber number tests

flow rate (ml/hr)	orifice plate (μm)	Weber	Strouhal
Test 1			
150	130	232	0.589
150	140	184	0.586
150	150	147	0.584
150	160	124	0.572
Test 2			
210	130	460	0.598
210	140	368	0.592
210	150	295	0.593
210	160	246	0.593

In the case of heat transfer experiments, the droplet stream was first set up to the desired parameters and power was applied to the heater. TLow heat flux condition was 8.6 W/cm^2, while for the high heat flux condition, it was 25 W/cm^2. The system was allowed to reach steady state and 199 IR images were acquired at a rate of 60 Hz. The images were processed, and the average minimum temperature was

obtained. No significant effect of Weber number on minimum surface temperature was found at both heat fluxes as shown in Figure 40. Posterior visualization of the droplet impingement confirmed that at this range of low Weber number spreading was the characteristic droplet impingement mode.

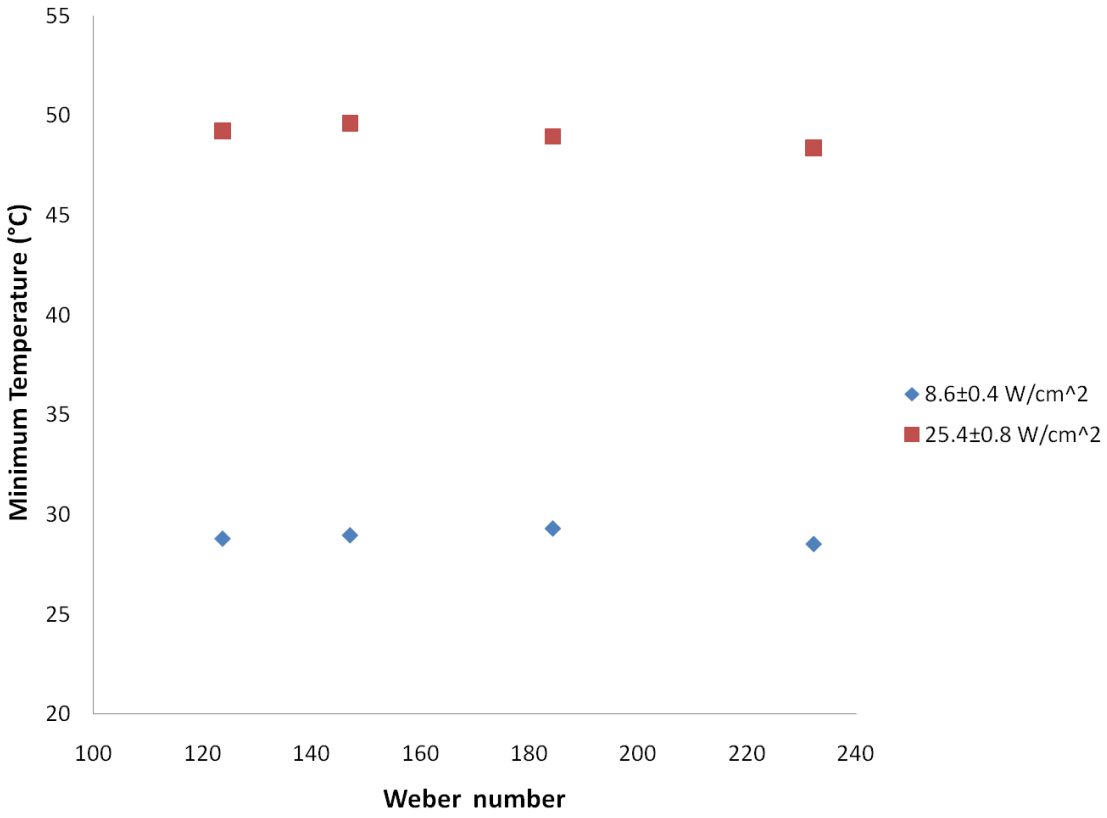

Fig. 40.: Minimum surface temperature at a flow rate of 150 ml/hr at Strouhal number of 0.585

In the case of film thickness experiments, the experimental procedure was similar. First, the droplet train was first fixed to the desired parameters and aligned

with the center of the laser beam. Then, power was applied to the heater to produce a heat flux condition of 8.6 W/cm^2, and 25 W/cm^2, respectively. Once the heater reached steady state, film thickness data were obtained. Figure 41 shows a decrease of maximum film thickness with heat flux, but variation of film thickness with Weber number is within experimental uncertainty for this range of Weber number.

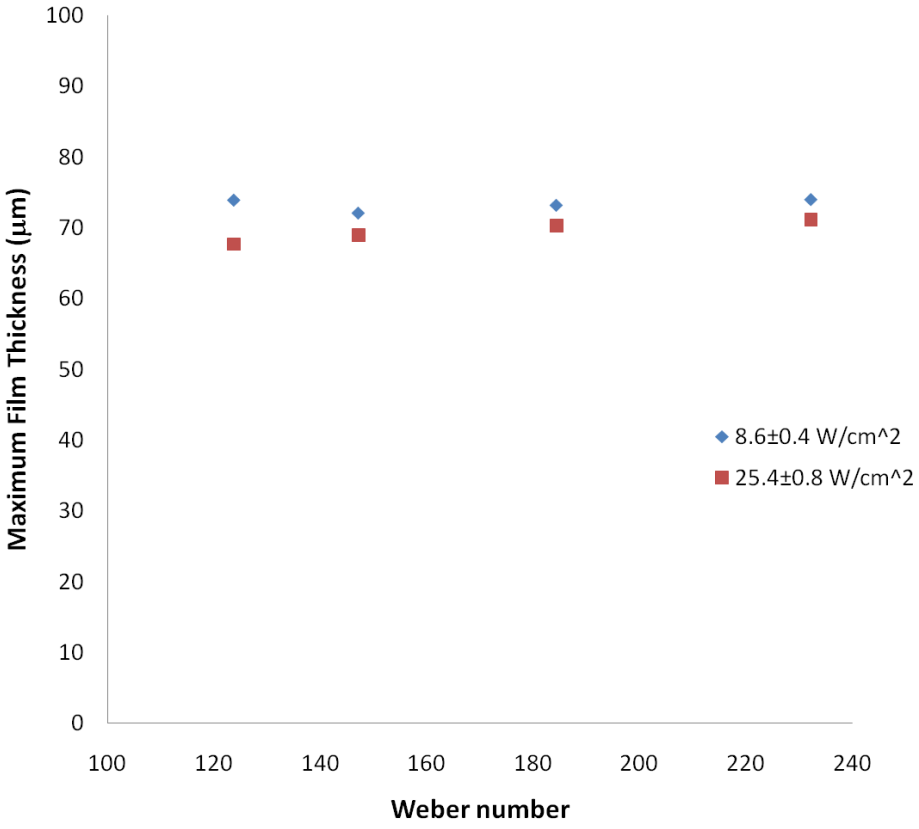

Fig. 41.: Film thickness flowrate of 150 ml/hr at Strouhal of 0.585

A similar procedure was followed for the cases of higher range of Weber number. An increase of minimum surface temperature averaging 5 ℃ was found (see Figure

42) with increasing Weber number. Posterior visualization of the impingement zone showed an impact regime of splashing. The results suggest that an increase in Weber number resulting in splashing affecting the impingement mode and the ability of the droplet stream to remove heat effectively resulting in a higher surface temperature.

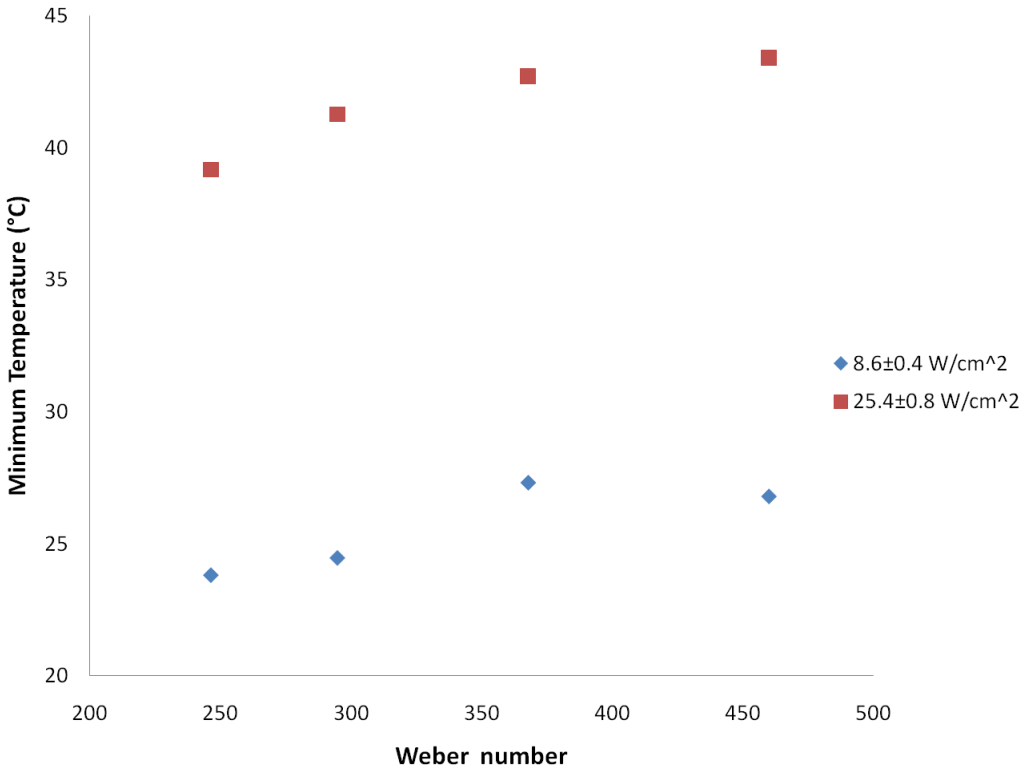

Fig. 42.: Minimum temperature at a flow rate of 210 ml/hr at Strouhal number of 0.594

At the higher range of Weber number, film thickness variation with heat flux was found to be minimal. The apparent decrease of film thickness seen in Figure 43 is within experimental error of the measurement technique. For the two cases tested,

maximum film thickness was independent of Weber number and heat flux rate.

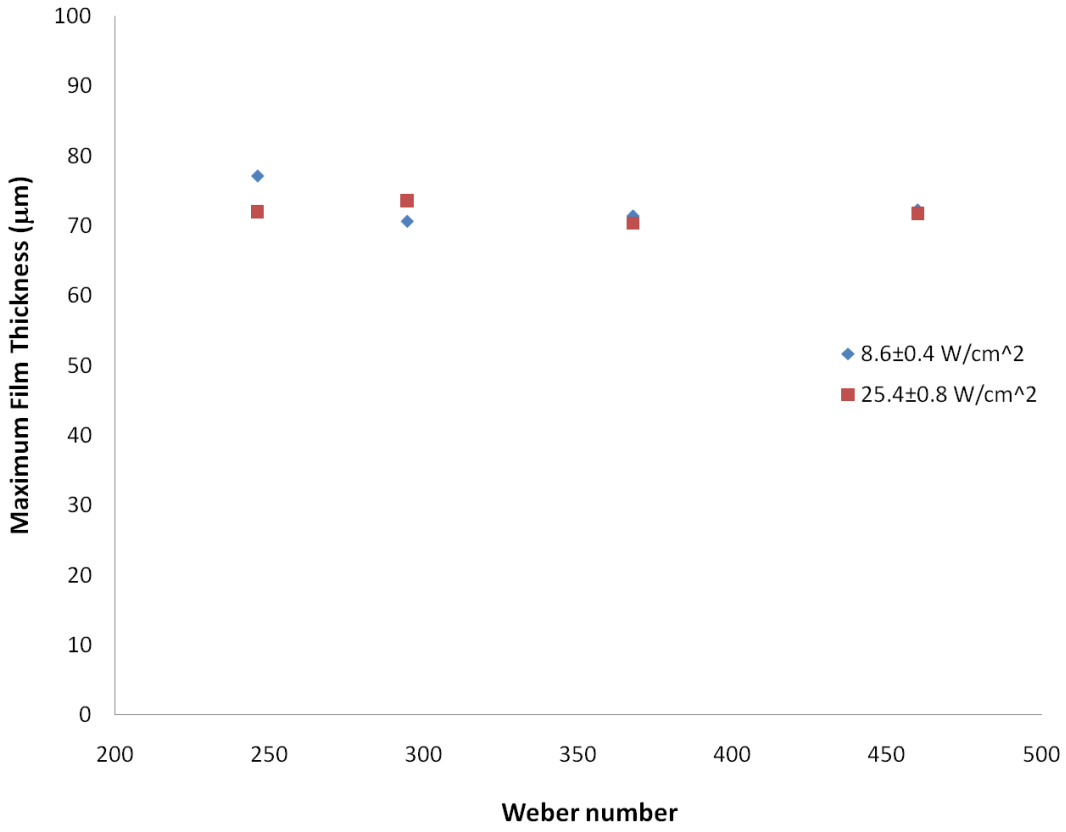

Fig. 43.: Film thickness at a flow rate of 210 ml/hr at Strouhal number of 0.594

Investigation of the effect of Strouhal number variation was only possible at two values of Strouhal number for fixed flow rates and Weber number. Experiments were performed at a fixed flow rate value of 210 ml/hr and Weber number of 339, Strouhal number was varied from 0.456 to 0.683. No significant effect was found based on time average minimum temperature value as well as film thickness as shown in Table XII .

Table XII.: Strouhal test results

Strouhal	Heat flux (W/cm^2)	Minimum Temperature ℃	Maximum Film Thickness (μm)
0.456	8.6	26.7	75
0.683	8.6	26.9	71
0.456	26.0	70.3	71
0.683	25.9	70.4	73

E. Characterization of Overall Heat Transfer Trends and Modes

The experimental data obtained through the project has given us the tools and information needed to identify the main heat transfer phenomena inside the crown formation caused by droplet stream impingement. Experimental data have allowed for the analysis of the heat transfer process.

1. Single Stream Impact Regime Characterization

Characterization of the droplet impact regime provides information about the hydrodynamics and heat transfer phenomena present during the impingement and film evolution processes. Impinged film hydrodynamics phenomena during droplet impact changes when transitioning from one impingement regime to other. As a consequence, changes in heat transfer behavior including variation in heat transfer coefficient or critical heat flux (CHF) value may be affected by a regime transition. Impact regimes of the experiments performed have been identified by means of high speed visualiza-

tion and compared with available models in the literature.

The simplest of the empirical models are those do not take into account any influence of surface temperature or presence of a liquid film on the target surface. In the case of a monodispersed droplet train impacting a flat surface, Mundo et al. [71] performed a series of experiments using water, ethanol, and a mixture of water-sucrose-ethanol on a stainless steel surface in which any film from previous droplet deposition had been continuously removed. A correlation for deposition-splashing boundary in terms of Reynolds number ($\rho v d_d/\mu$) and Ohnesorge number ($\mu/\sqrt{\rho\sigma d_d}$) has been proposed as defined by equation (4.8) [71]. The relationship shows that the influencing factor is the momentum of the primary droplets in the direction normal to the surface.

$$\kappa_C = Oh.We^{1.25} \tag{4.8}$$

$$\kappa_C > 57.7 \quad (splashing)$$

$$\kappa_C < 57.7 \quad (spreading)$$

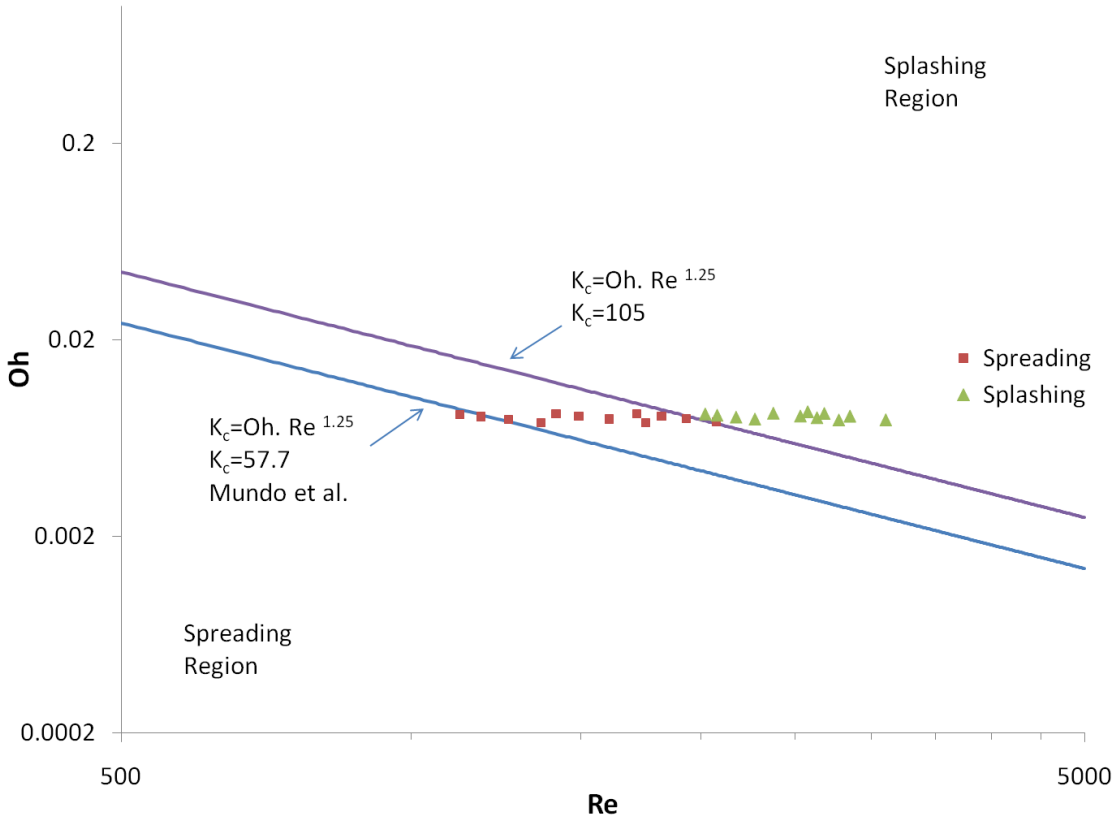

Fig. 44.: Limits for splashing and spreading of monosized droplet trains ($80 < We < 590$)

Figure 44 shows a comparison of Mundo et al. [71] model with the data collected as part of this research work. From Figure 44, it is clear that Oh number had little variation for the different single-stream experiments that were performed. In order to test a broader range of Oh number, different fluids with distinct properties would be necessary. The transition from spreading to splashing occurs at a critical value of constant κ of 105 for data obtained and not at 57.7 as predicted by Mundo et al. 44. One possible explanation for this difference is the permanent presence of a liquid film on the heater surface which acted as a damping medium and helped delay the

transition from spreading to splashing.

Other researchers have characterized droplet impingement regimes taking into account surface temperature. This approach provides a qualitative description of the heat induced phenomena. The two most used approaches to map the impact regimes have been done by Bai et al. [65] and Rein [90] based on Weber number and surface temperature (T_W). In these two approaches, a critical Weber number in which transition from spreading to splashing occurs is defined based on experimental observations.

Several empirical models exist that describes droplet behavior upon impingement [64]. The physics of droplet impact on a wetted wall is captured by the models of Bai-Gosman [65] and Samenfink [104]. Bain-Gosman defines a critical Weber number as seen in Equation (4.9) at which transition from spreading to splashing occurs.

$$We_{cr} = 1320.Oh^{0.36} \tag{4.9}$$

Figure 45 depicts the observed impact regimes following the Rein approach based on the Bai-Gosman model for the definition of the critical Weber number. The Bai-Gosman model predicts a transition Weber number of 239 which is close to the observed spreading-to-splashing transition at a Weber number of 257. Rein mapping approach predicts an impact regime of bubbling for surface temperatures above the saturation temperature of the fluid and below the critical Weber number. Those conditions are obtained at a low flow rate (120 ml/hr) at high heat fluxes. However, the presence of that regime had not been observed as part of this work.

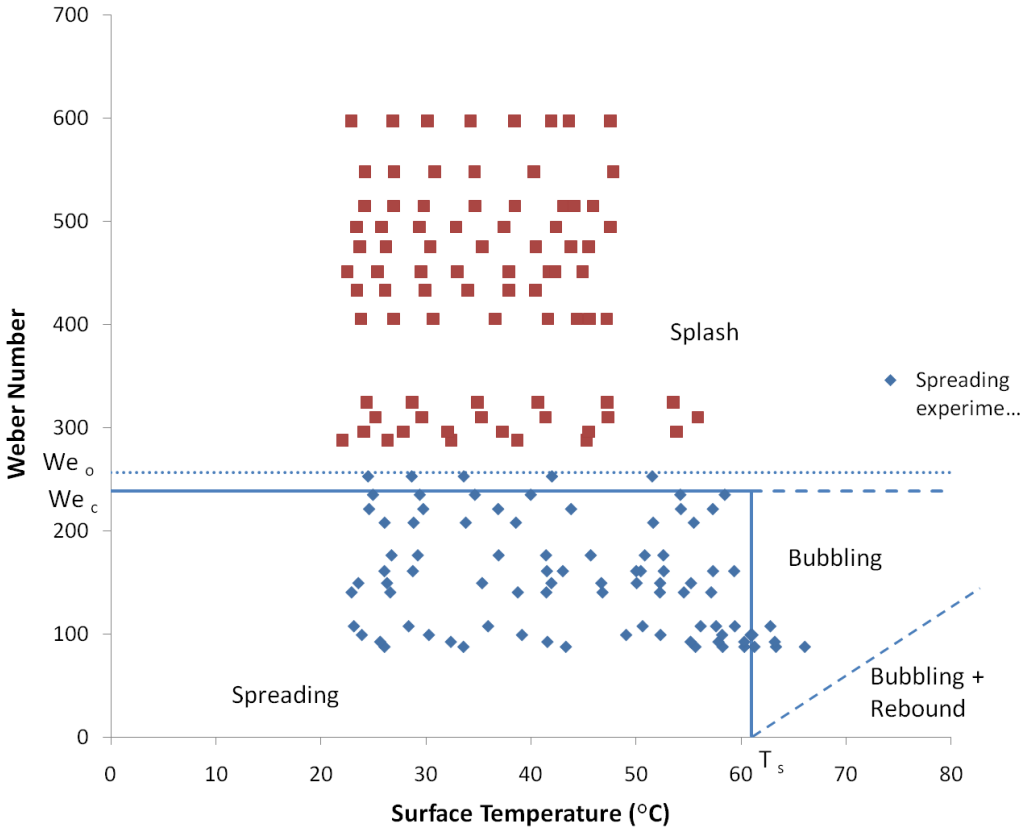

Fig. 45.: Mapping of splashing and spreading of monosized droplet trains of HFE-7100(Rein approach)

Figure 46 depicts the observed impact regimes following Bai approach using the Bai-Gosman model. In addition to depicting the transition between splashing and spreading, Bai et al. [65] also describes a transition from stick to spreading at a Weber number of 5. Bai et al. [65] also introduces a pure adhesion temperature (T_{PA}) above which transition to a break up regime occurs. The value of this temperature (T_{PA}) is larger than the boiling temperature of the fluid. In general, Bai's mapping technique of impact regimes fits well with observed data.

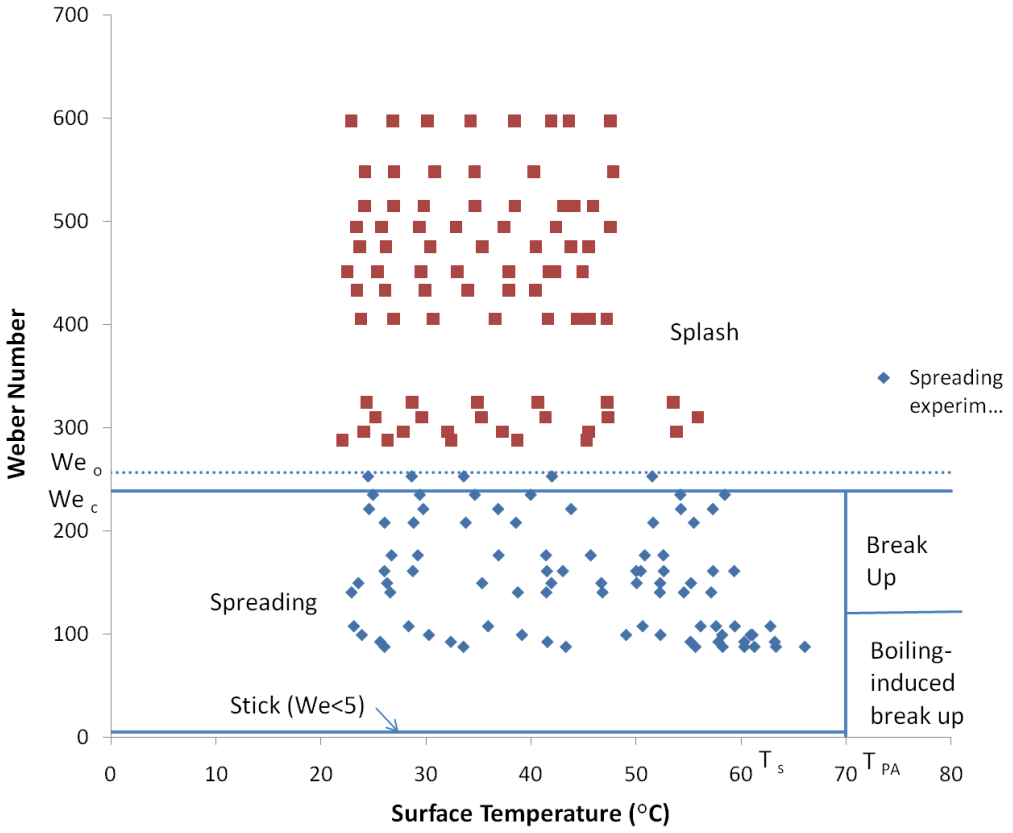

Fig. 46.: Mapping of splashing and spreading of monosized droplet trains using Bai approach

Samenfink et al. [104] also proposed a model to describe single droplet impact on a wetted surface. Thickness of the film is taken into account by a reference dimensionless value of film thickness (see Equation (4.10)). The transition criteria for the spreading to splashing transition is given by a critical Reynolds number (see Equation (4.11)).

$$\delta_b = \frac{film \;\; thickness}{droplet \;\; diameter}$$

$$\delta_{ref} = 1 + 0.39\delta_b - 0.08\delta_b^2 \tag{4.10}$$

$$Re_{cr} = 38.1 \frac{Oh^{-0.8378}}{\delta_{ref}} \tag{4.11}$$

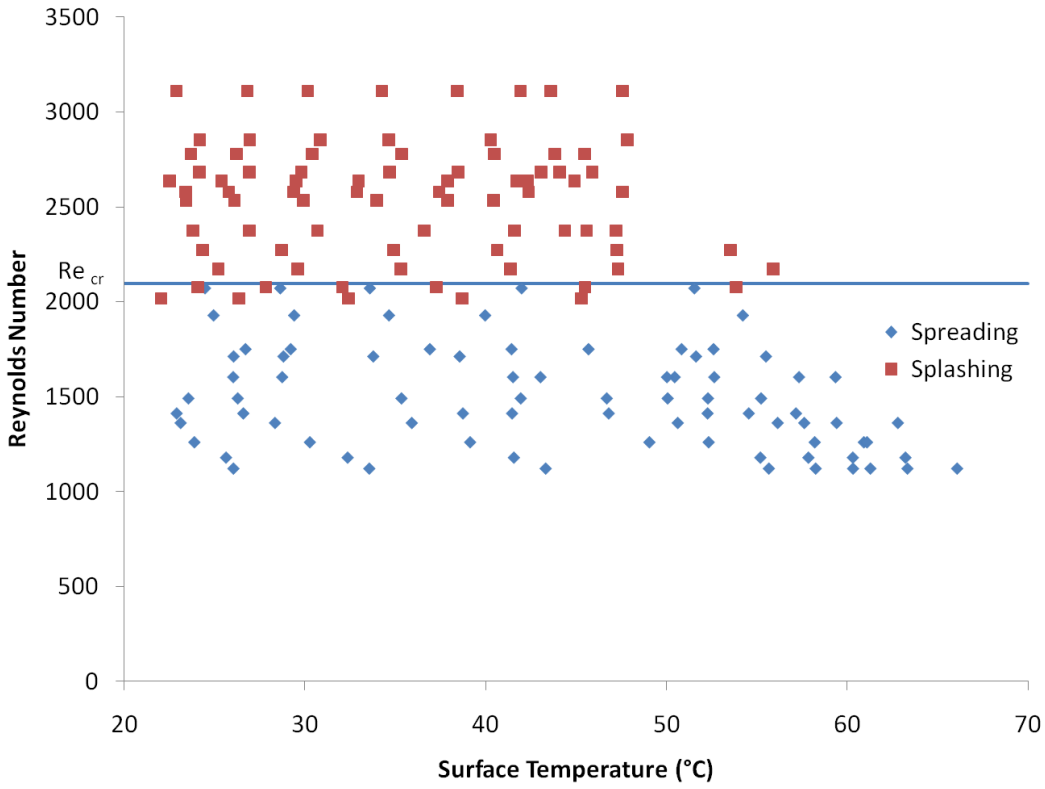

Fig. 47.: Mapping of impact regimes based on Samenfink model

Figure 47 presents a comparison of measured data with the Samenfink model. Reynolds critical value of 2,097 predicted by the Samenfink model fits well the observed data. However, there is a range of Reynolds number between 2,018 to 2,072 in which both spreading and splashing are present. Below Reynolds number of 2,018, all the cases observed belong to the spreading impact regime. Above Reynolds of 2,072,

all the observed cases exhibited a splashing behavior.

Overall, there is a good agreement between the three models found in the literature and experimental observations of this research work. Bai mapping approach with Bai-Gosman criteria for transition of spreading to splashing describes well the experimental findings of this research work. Moreover, the experimental data show that the three models can be used to reach conditions that could lead to best heat transfer performance.

2. Heat Transfer Analysis

A study of heat transfer behavior before, during and after crown formation upon droplet impingement was conducted. First, the regions of interest inside the crown formation were identified according to Figure 48. In the present research, we focused on the stagnation region, directly below of the impact of the droplet; and the boundary layer region in which both a momentum and thermal boundary layers grow periodically upon impingement of each droplet.

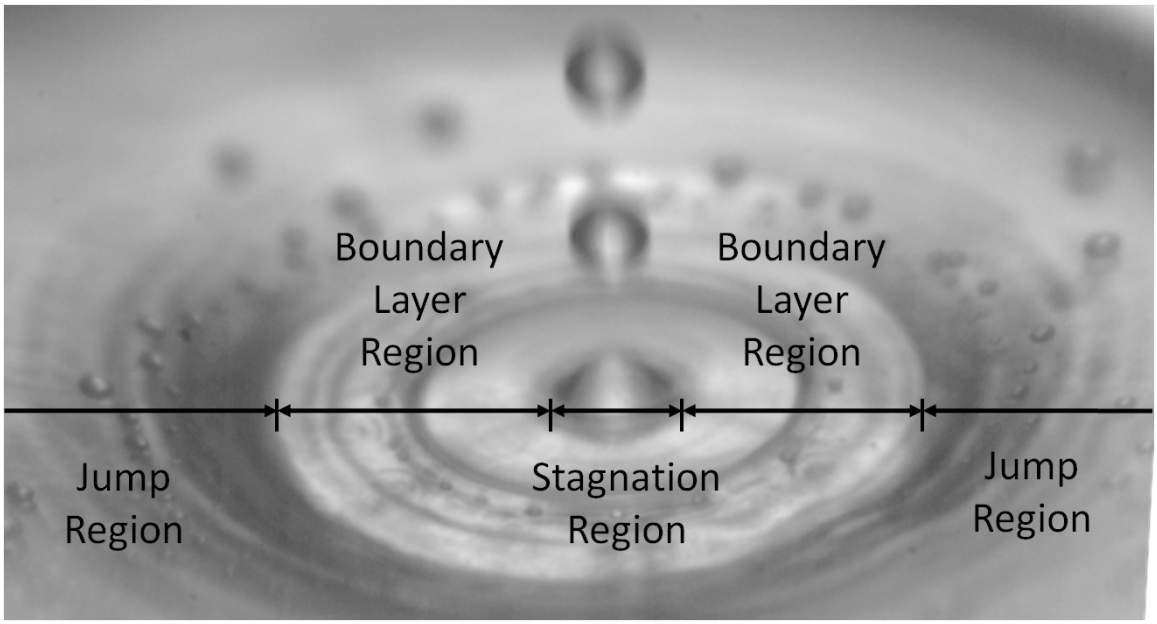

Fig. 48.: Identification of thermal regions upon droplet impingement

A good approximation of the convective heat transfer behavior of periodic droplet impingement can be found by using correlations for circular liquid jets [105, 106]. A comparison to the case of impinging droplets has been performed using existing analytical results for circular liquid jets for fluids with Prandtl number above one which fit the case of HFE-7100 at $Pr = 9.59$.

Integral analysis of the boundary layer [107, 108] for the case of circular jet impingement shows that film thickness can be correlated to other physical parameters using Equation (4.12). Film thickness in the range of 14 to 18 μm can be predicted for jets equivalent in size to single train of droplets at a radial position of 300 μm from the point of impact. This result shows very good agreement with the measured film thickness at the same position in the range of 10 μm to 80μm.

$$h = 0.1713 \left(\frac{d^2}{r}\right) + \frac{5.147}{Re_d} \left(\frac{r^2}{d}\right) \tag{4.12}$$

Convective heat transfer of a circular jet have been explained by different authors [105, 106]. Liu et al. [105] identified four different regions for a jet impinging on a surface. First, the stagnation zone directly at the point of impact of the jet in which the jet decelerates and changes direction. The following is the local Nusselt number correlation (4.13) suggested for for that zone with Prandtl number values greater than unity[105].

$$Nu_d = 0.797 Re_d^{1/2} Pr^{1/3} \tag{4.13}$$
$$0 \leq r/d < 0.787$$

The second region identified is the boundary layer region. In this region, both the viscous and thermal boundary layers develop along the radial direction. This region ends where the viscous boundary layer encounters the film surface. [105]. The local Nusselt number correlation (4.14) suggested by Liu et al. [105] is as follows:

$$Nu_d = 0.632 Re_d^{1/2} Pr^{1/3} \left(\frac{d}{r}\right)^{1/2} \tag{4.14}$$
$$2.23 < r/d < 0.1773 Re_d^{1/3}$$

In the third region, the viscous boundary layer reaches the free surface but the thermal boundary layer is still developing. In this region, the velocity outside the viscous boundary layer decreases with radial position. The local Nusselt number is given by Equation (4.15). For all practical purposes, the region where the thermal boundary layer reaches the free surface starts at a radial position outside of our region of interest.

$$Nu_d = \frac{0.407 Re_d^{1/2} Pr^{1/3} \left(\frac{d}{r}\right)^{2/3}}{\left[0.1713 \left(\frac{d}{r}\right)^2 + \frac{5.147\ r}{Re_d d}\right]^{2/3} + \left[\frac{1}{2}\left(\frac{r}{d}\right)^2 + C_3\right]^{1/3}} \tag{4.15}$$

$$C_3 = \frac{0.267 \left(\frac{d}{r_o}\right)^{1/2}}{\left[0.1713 \left(\frac{d}{r_o}\right)^2 + \frac{5.147\ r_o}{Re_d d}\right]^2} - \frac{1}{2}\left(\frac{r_o}{d}\right)^2$$

$$0.1773 Re_d^{1/3} < r/d < 1200 Re_d^{-0.422}$$

The experimental local Nusselt number was obtained at each radial position using the corresponding local temperature, the initial (before impact) fluid temperature, and the corrected heat flux value as indicated by equation (4.16).

$$Nu(r) = \frac{q''}{T(r) - T_o} \frac{d}{k_l} \tag{4.16}$$

Figure 49 shows Nusselt number data as a function of radial distance for several cases. The first case is based on the Liu et al.[105] model for jet impingement. Figure 49 also depicts experimental data from single droplet impingement at the same flow rate as the Liu's case as well as fitted model to the single droplet impingement case. Figure 49 shows local Nusselt number for three distinct cases at 120 ml/hr, 180 ml/hr, and 280 ml/hr. The comparison was done to understand any similarities between the single droplet impingement and jet impingement cases by just looking at the behavior inside the crown formation. The fitted local Nusselt number has the following form (see Equation (4.18)).

$$Nu_d = ARe_d^{1/2}Pr^{1/3} \tag{4.17}$$

$$0 < r/d \leq 1$$

$$Nu_d = ARe_d^{1/2}Pr^{1/3} * (d/r)^b \tag{4.18}$$

$$r/d > 1$$

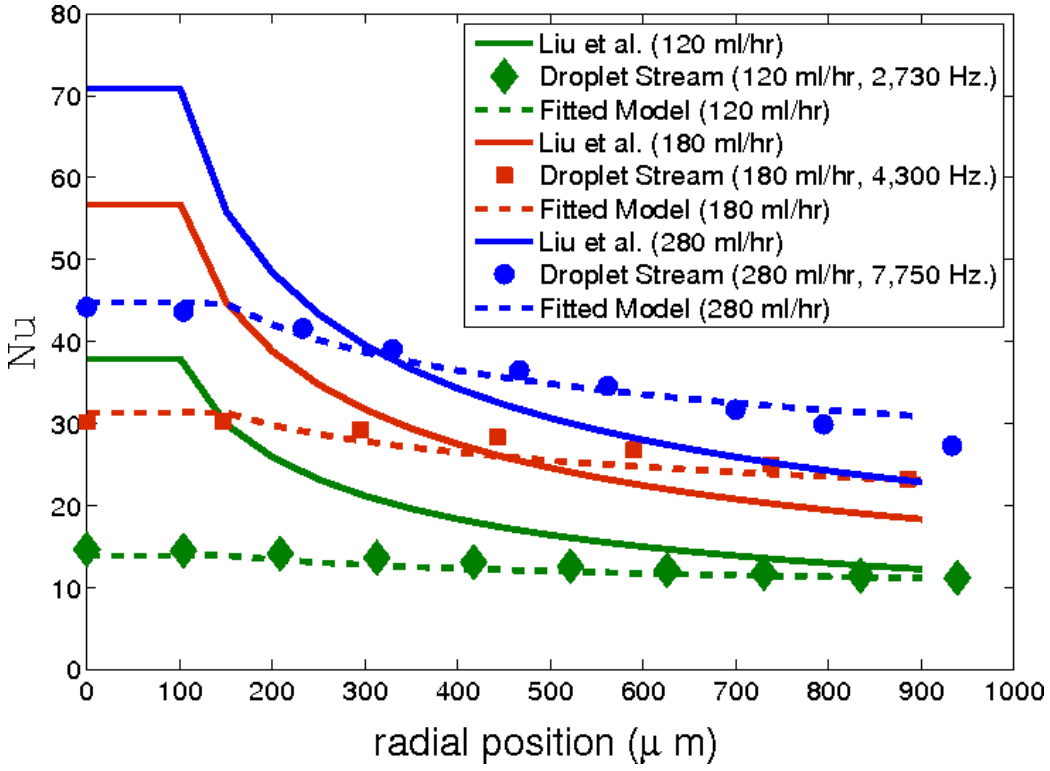

Fig. 49.: Comparison jet impingement to Nusselt number

From Figure 49, jet impingement model alone does not capture well the physics of droplet impingement heat transfer. Basically, the Liu's model overpredicts local Nusselt number on the stagnation zone. In addition, the decay of local Nusselt number on the boundary layer region is overpredicted by the jet impingement model. However, the fitted model predicts well the behavior on the stagnation zone. It is worth noting that constant A and coefficient b of the fitted model increases with increasing flow and with smaller vertical droplet spacing as it approaches the behavior of a continuous jet as shown on Table XIII.

Table XIII.: Local Nusselt number coefficients

Case	Flowrate	Frequency	Velocity	Vertical spacing Droplets	A	b	R^2
	ml/hr	$Hz.$	m/s	μm			
Jet Impingement	NA	NA	NA	NA	0.632	0.5	NA
Droplet Stream	280	7,750	4.42	570	0.503	0.21	0.89
Droplet Stream	180	4,300	2.8	650	0.416	0.17	0.83
Droplet Stream	120	2,730	1.81	663	0.246	0.12	0.83

It is worth noting that the fitted model (4.18) does not capture well the reduction of local Nusselt number on the boundary layer region. It underpredicts the local Nusselt number after the stagnation zone while it overpredicts it before the jump region. It can be inferred that the morphology of the boundary layer during droplet impingement is different to jet impingement since Liu's model (jet impingement model) is based on continuous growth of the boundary layer. From Figure 49, it is evident that Liu's model cannot capture well how Nusselt number changes with radial distance. This suggests that the periodic nature of the impingement process affects the growth

of the film boundary layer in a way that results in higher Nusselt number values at radial distances greater than 300 μm when flowrate is at 280 ml/hr. Periodicity of droplet impingement also results in a lower Nusselt number in the stagnation region because of the intermittent nature of liquid flow, but the periodic disturbances on the boundary layer in the crown region are assumed to improve heat transfer resulting in a more uniform local Nusselt number as discussed previously. Aditionally, there exists a difference in behavior in the cases where spreading and splashing occurs. In the case of spreading, the coefficient b varies from a range of 0.12 to 0.17 as indicated in Table XIII and deviates considerably from the jet impingement model. In all cases of splashing, coefficient b ranges from 0.20 to 0.22 which is closer to the jet impingement case since in the splashing cases, the effect of periodic droplet spreading is disturbed by the break up and impact of secondary droplets in the radial direction. As a result, the boundary layer growth resembles the jet impingement case.

3. Critical Heat Flux Characterization

Critical heat flux (CHF) was characterized for different conditions for single and triple droplet trains. Figure 50 shows CHF behavior for the case of single stream as a function of Weber number. Behavior of CHF differs significantly with the impact regime (i.e. splashing or spreading). In the spreading regime, CHF increases with Weber number and exhibits a more stable behavior. When splashing regime is present, CHF increases with Weber number at a lower rate. Furthermore, the behavior is also more chaotic resulting in a wide variation of Nusselt number when correlated to Weber number.

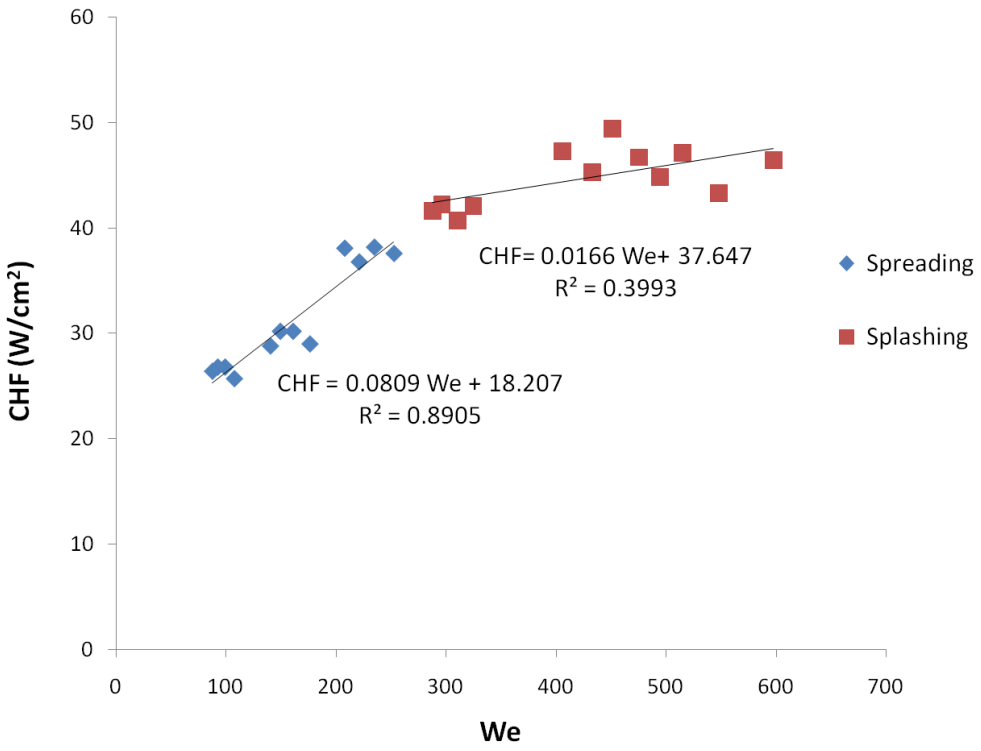

Fig. 50.: Critical heat flux as a function of Weber number

A general equation to correlate critical heat flux (CHF) to other physical parameters was also obtained. A common approach in two phase flow to obtain a nondimensional expresion of the CHF [59, 58] is to use the Kutateladze number (4.19) as follows:

$$K = \frac{q"_c}{v_d h_{fg} \rho_L} \tag{4.19}$$

Other researchers [39] have concluded that a more appropriate approach is to obtain a non-dimensional heat flux expresion based on the surface average mass flow rate ($\dot{m}"$).

The following correlation of critical heat flux (CHF)(4.20) in terms of Weber number, and Strouhal number was obtained using the least square fit method and and the experimental data.

$$\frac{qc''}{\dot{m}'' h_{fg}} = 8.283 We^{-0.1323} St^{-0.0952} \tag{4.20}$$

where:

$$80 < We < 590$$

$$0.43 < St < 0.69$$

The R-squared values of the correlation obtained was 0.67, with a maximum error of 13.4 %. Figure 51 shows the results of the critical heat flux correlation for the single stream cases. As it can been seen, We and St can be used to estimate CHF for monosized droplets impinging on a surface.

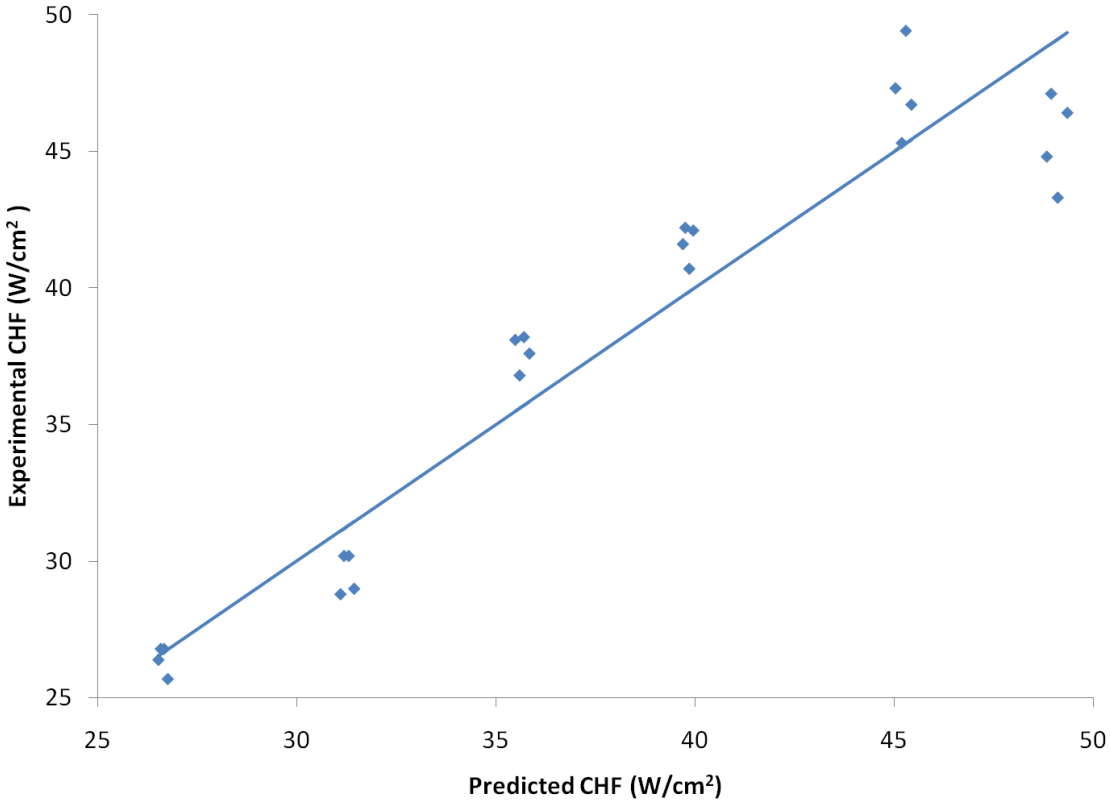

Fig. 51.: Comparison for experimental and predicted critical heat flux for single stream cases

Figure 52 shows the dependance of critical heat flux on dimensionless spacing defined as the ratio of spacing between adjacent streams and droplet diameter for the triple stream cases. From Figure 52, it is clear that critical heat flux depends on horizontal spacing (i.e. distance from impact-to-impact points). The main factor is density of the spray influences the nature of the impact regime with direct consequences on heat transfer behavior. Experimental results indicate that CHF increases with impact-to-droplet spacing ratio. Impact-to-droplet spacing ratio accounts for the density of droplets impinging on a surface which is of vital importance in the design of spray systems. This suggests that each impact crater and impinging pro-

cess should not be destructively interrupted by secondary droplets emanating from splashing events and adjacent impact craters that suppress the inner flow structure of each individual crater.

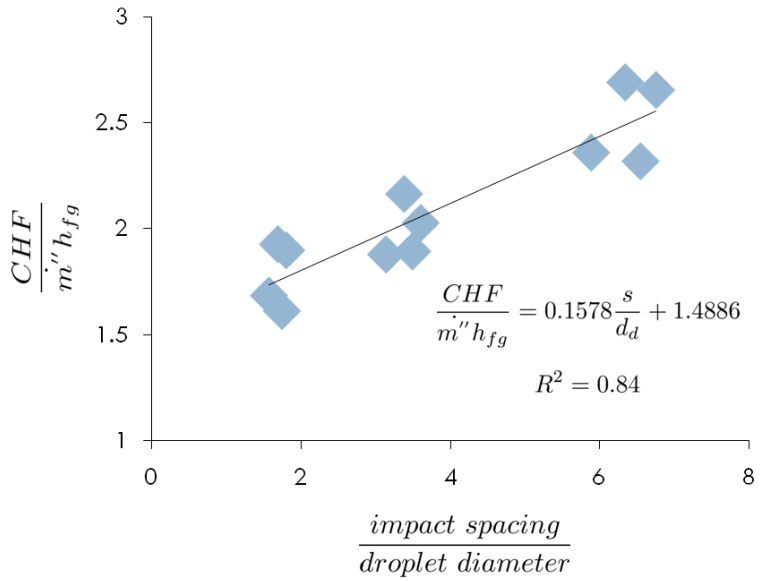

Fig. 52.: Critical heat flux as a function of non-dimensional spacing for triple stream cases

The droplet impingement studies by Healy [59] and Sellers [62] characterizing critical heat flux (CHF) behavior reached different conclusions for similar ranges of Weber and Strouhal numbers (See Equations (2.6) and (2.7)). In both studies, water was used as heat transfer fluid and droplet diameter was the characteristic length used for both Weber and Strouhal numbers definitions. Additionally, Strouhal number was the same for both cases. To allow comparison with the present study, Equations (2.6) and (2.7) were rewritten in the form of Equation (4.21) obtaining coefficients a,b, and

c as presented in Table XIV. Table XIV shows a good agreement between the present research and Seller's [62]. Results of the present work differs with work of Healy et al. [59] on the role of frequency and velocity on critical heat flux. Healy [59] used droplets in the milimetric scale and at low frequencies, which might have produced a different impact regime probably resulting in rather different heat transfer behavior. In summary, our experimental work confirms Sellers [62] work which should be used in the analysis and study of droplet impingement in the future.

$$qc^{''} = Constant * v_d^a * d_d^b * f^c \tag{4.21}$$

Table XIV.: Critical heat flux coefficients

	a	b	c
Healy	-1.6413	-0.2933	0.6883
Sellers	-0.0973	2.737	0.8569
Present work	-0.169	2.772	0.904

CHAPTER V

CONCLUSIONS AND RECOMMENDATIONS

A. Conclusions

The main objective of this study was to gain a better understanding about the physics of droplet impingement cooling as the basis of spray cooling systems. The knowledge generated provides tools for the design and development of spray cooling systems.

The heater used in this research was designed to be transparent on the optical wavelength range to allow visualization studies of the droplet impingement zone, as well as film thickness measurement of the impact zone using non-invasive optical techniques.

The use of infrared imaging allowed temperature measurement with a spatial resolution of 100 μm, and a temporal resolution of 60 Hz. Hence, it was possible to study localized heat transfer behavior inside the droplet crown formation instead of using the classical approach which considers the whole heater area as seen in spray cooling studies. The design of the heater made film thickness measurement possible at a radial location of 300 μm from the point of impact of the droplet train which was always within the boundary layer region of the crown formation.

Heat transfer curves at all flowrates follow a linear behavior consistent with single phase convection as the main heat transfer mechanism. Minimum surface temperatures were below saturation temperature of HFE-7100 for heat fluxes immediately below critical heat flux (CHF) at all flowrates except the cases at 120 ml/hr. Surface temperature inside the crown formation was below saturation temperature at all cases, except for the heat flux immediately below critical heat flux at 120 ml/hr.

Behavior at the impingement zone varied with flow rate, frequency and veloc-

ity of the droplets. Localized droplet impingement heat transfer behavior tends to approximate jet impingement models[105] with increasing flowrate, frequency and velocity of impinging droplets. The largest difference between the Liu's model and the experimental data occurs inside the boundary layer region. This result suggest that a continuous boundary layer growth model as found on jet impingement systems could not capture the periodic behavior of droplet impingement system in which the boundary layer grows and collapses periodically with each droplet impact.

Forced convection was determined to be the main heat transfer mechanism inside the crown formed upon droplet impingement, even at heat fluxes near the critical heat flux (CHF). Nucleate boiling, secondary nucleation only take place outside the crown structure.

Critical heat flux (CHF) findings are in good agreement with results of Sellers [61] in the case of single train impingement. In the case of triple train impingement, the key factor is the horizontal spacing between droplets. Results suggest that density of the spray affects the impact regime resulting in a less than optimal heat transfer behavior.

Film thickness inside the crown formation varies from 10 to 80 μm for all single train cases tested with and without heat flux. Film thickness results are in the same range as experiment conducted using spray cooling systems [92] which ranged from 18 to 80 μm using FC-72 as working fluid. Single-droplet impingment compared well in film thickness terms with Liu's jet impingement model.

Crown formation was characterized and impact of parameters such as heat flux and flow rate were studied. Impact regime was observed and compared with existing models found in the literature [71, 65, 104] mostly developed for fuel injection systems. Good agreement was found with Bai-Gosman and Samenfink models to predict the transition from spreading to splashing. Bai mapping of impact regimes which take

into account surface temperature fits the observed data well. Impact regime was found to play an important role in the local Nusselt number and critical heat flux (CHF) behavior.

A parametric study to quantify the effects of Weber number and Strouhal number on heat transfer and film thickness was conducted. It was found that heat transfer performance deteriorate with Weber number when splashing occurs. Weber number did not play a significant role during droplet impingement while on the spreading mode.

B. Recommendations

As a result of the findings in this research work, the following considerations for additional research are suggested:

The range of droplet velocities, diameters and frequencies should be extended at the same flow rates. This could be achieved by changing the diameter of the orifice plates. The extension of the experimental range could help achieve different impact regimes at the same flow rate, and investigate its effects on heat transfer phenomena. Arrays of droplets of different configurations could be used to investigate effect of staggered and non-staggered arrays with an emphasis on the interaction between adjacent droplets.

A more profound study of the effects of droplet spacing could be performed with the use of an additional droplet generator. A set-up could be built with the capability of continuously changing spacing of two adjacent droplet trains in order to find the optimal spacing between droplets. The effect of impact angle on heat transfer could be investigated by slightly modifying the experimental set-up. Effects of the combination of angle and spacing could be investigated further. Droplet trains whose

momentum direction either approaches, departs from each other could be achieved and investigated with small variations of the experimental set-up.

Adjacent droplet impingement with droplets impinging on phase or out of phase should be investigated by using two generators. The control of droplet phase could be done by modifying the function generator input to each droplet generator head, and with special care of environmental conditions that could disturb the droplet trains. Emphasis should be placed on the interaction region between adjacent droplet impacts with special attention to surface temperature and film thickness at this region.

Novel heat transfer fluids such as ceramic and metallic based nanofluids should be investigated as well. The effects of nanoparticles on surface temperature and critical heat flux should be characterized. Nanostructures on the ITO surface could be manufactured and tested. Its effects on surface temperature, critical heat flux, and film thickness could be investigated with the same experimental techniques used in this research.

An increase of the temporal resolution of the temperature measurement technique should be explored too. Two options are available to achieve this purpose. The first option is the use of a faster infrared camera that would allow to measure temperature fluctuations between droplet impact. The second option is the use of an alternative technique such as deposited thin film thermocouples at discrete locations on the heater. A heater could be designed in which surface temperature is measured with infrared thermography as well as with thin film thermocouples. This approach should result in higher temporal and spatial resolution, as well as a reduction of measurement uncertainty at the thin film thermocouple locations.

Heat transfer coefficients and its corresponding Nusselt numbers were calculated based on initial fluid (before impact) temperature of the working fluid. A technique such as Temperature Oscillating Infrared Thermography (TOIRT)[109, 110] could be

used to measure heat transfer coefficients without the assumption of an initial fluid temperature. The TOIRT method is based on the response of a surface to a known change in applied heat flux. With knowledge of the material properties and transient temperature response, heat transfer coefficients could be calculated.

Velocity field at the boundary layer region could be measured with techniques such as micro Particle Image Velocimetry (μPIV) and contrasted with 3-D numerical simulation. This approach would clarify the physical phenomena occuring at the boundary layer region.

REFERENCES

[1] R. Tummala, *Introduction to System on Package (SOP) : Miniaturization of the Entire System*, New York, McGraw-Hill Professional Publishing, 2008.

[2] G. E. Moore, "Cramming more components onto integrated circuits," *Electronics*, vol. 38, no. 8, pp. 1–4, 1965.

[3] "International technology roadmap for semiconductors 2009," `http://www.itrs.net/Links/2009ITRS/Home2009.htm`, id: 1.

[4] J. Kim, "Spray cooling heat transfer: The state of the art," *International Journal of Heat and Fluid Flow*, vol. 28, no. 4, pp. 753–767, 2007.

[5] I. Mudawar, "Assessment of high-heat-flux thermal management schemes," *IEEE Transactions on Components and Packaging Technologies*, vol. 24, no. 2, pp. 122–141, 2001.

[6] A. Bar-Cohen, M. Arik, and M. Ohadi, "Direct liquid cooling of high flux micro and nano electronic components," *Proceedings of the IEEE*, vol. 94, no. 8, pp. 1549–1570, 2006.

[7] K. A. Estes and I. Mudawar, "Comparison of two-phase electronic cooling using free jets and sprays," *Journal of Electronic Packaging, Transactions of the ASME*, vol. 117, no. 4, pp. 323–332, 1995.

[8] M. Visaria and I. Mudawar, "Application of two-phase spray cooling for thermal management of electronic devices," *IEEE Transactions on Components and Packaging Technologies*, vol. 32, no. 4, pp. 784–793, 2009.

[9] M. S. Sehmbey, L. C. Chow, M. R. Pais, and T. Mahefkey, "High heat flux spray cooling: A review," in *Proceedings of the 1994 International Mechanical Engineering Congress and Exposition*, Chicago, IL, Nov. 6-11, 1994, vol. 301, pp. 39–46, ASME.

[10] B. Agostini, "State of the art of high heat flux cooling technologies," *Heat Transfer Engineering*, vol. 28, no. 4, pp. 258–281, 2007.

[11] J. Garg, M. Arik, S. Weaver, T. Wetzel, and S. Saddoughi, "Meso scale pulsating jets for electronics cooling," *Journal of Electronic Packaging, Transactions of the ASME*, vol. 127, no. 4, pp. 503–511, 2005.

[12] S. Y. Kim, M. H. Lee, and K.-S. Lee, "Heat removal by aluminum-foam heat sinks in a multi-air jet impingement," *IEEE Transactions on Components and Packaging Technologies*, vol. 28, no. 1, pp. 142–148, 2005.

[13] J. S. Bintoro, A. Akbarzadeh, and M. Mochizuki, "A closed-loop electronics cooling by implementing single phase impinging jet and mini channels heat exchanger," *Applied Thermal Engineering*, vol. 25, no. 17-18, pp. 2740–2753, 2005.

[14] H. Sun, C. F. Ma, and Y. C. Chen, "Prandtl number dependence of impingement heat transfer with circular free-surface liquid jets," *International Journal of Heat and Mass Transfer*, vol. 41, no. 10, pp. 1360–1363, 1998.

[15] Y. C. Chen, C. F. Ma, M. Qin, and Y. X. Li, "Theoretical study on impingement heat transfer with single-phase free-surface slot jets," *International Journal of Heat and Mass Transfer*, vol. 48, no. 16, pp. 3381–3386, 2005.

[16] X. Liu, J. H. Lienhard V, and J. S. Lombara, "Convective heat transfer by

impingement of circular liquid jets," *Journal of Heat Transfer*, vol. 113, no. 3, pp. 571–582, 1991.

[17] X. S. Wang, Z. Dagan, and L. M. Jiji, "Heat transfer between a circular free impinging jet and a solid surface with non-uniform wall temperature or wall heat flux. 2. solution for the boundary layer region," *International Journal of Heat and Mass Transfer*, vol. 32, no. 7, pp. 1361–1371, 1989.

[18] H. Fujimoto, H. Takuda, N. Hatta, and R. Viskanta, "Numerical simulation of transient cooling of a hot solid by an impinging free surface jet," *Numerical Heat Transfer; Part A: Applications*, vol. 36, no. 8, pp. 767–780, 1999.

[19] M. M. Rahman, A. J. Bula, and J. E. Leland, "Numerical modeling of conjugate heat transfer during free liquid jet impingement," in *Proc. of the 1998 ASME International Mechanical Engineering Congress and Exposition,*, Anaheim, CA, November 15- 20, 1998, vol. 38, pp. 475–486.

[20] D. M. Schafer, S. Ramadhyani, and F. P. Incropera, "Numerical simulation of laminar convection heat transfer from an in-line array of discrete sources to a confined rectangular jet," *Numerical Heat Transfer; Part A: Applications*, vol. 22, no. 2, pp. 121–141, 1992.

[21] M. R. Overholt, A. McCandless, K. W. Kelly, C. J. Becnel, and S. Motakef, "Micro-jet arrays for cooling of electronic equipment," in *Proc. of the 3rd International Conference on Microchannels and Minichannels, ICMM2005*, June 13, 2005, vol. PART B, pp. 249–252.

[22] M. Fabbri and Vijay K. Dhir, "Optimized heat transfer for high power electronic cooling using arrays of microjets," *Journal of Heat Transfer*, vol. 127, no. 7, pp. 760–769, 2005.

[23] T. Brunschwiler, H. Rothuizen, M. Fabbri, U. Kloter, B. Michel, R. J. Bezama, and G. Natarajan, "Direct liquid jet-impingement cooling with micronsized nozzle array and distributed return architecture," in *Proc. of the 1Oth Intersociety Conference on Thermal and Thermomechanical Phenomena and Emerging Technologies in Electronic Systems, ITherm 2006,*, San Diego, CA, May 13 - June 2 2006, pp. 196–203.

[24] K. Kanokjaruvijit and R. Martinez-Botas, "Jet impingement on a dimpled surface with different crossflow schemes," *International Journal of Heat and Mass Transfer*, vol. 48, no. 1, pp. 161–170, 2005.

[25] G. Natarajan and R. J. Bezama, "Microjet cooler with distributed returns," *Heat Transfer Engineering*, vol. 28, no. 8-9, pp. 779–787, 2007.

[26] S. V. Garimella and R. A. Rice, "Heat transfer in submerged and confined jet impingement," in *Proc. of the 1994 International Mechanical Engineering Congress and Exposition*, Chicago, IL, USA, Nov. 6-11 1994, vol. 301, pp. 59–68.

[27] I. Mudawar and D. C. Wadsworth, "Critical heat flux from a simulated chip to a confined rectangular impinging jet of dielectric liquid," *International Journal of Heat and Mass Transfer*, vol. 34, no. 6, pp. 1465–79, 06 1991.

[28] I. A. Kopchikov, G. I. Voronin, T. A. Kolach, D. A. Labuntsov, and P. D. Lebedev, "Liquid boiling in a thin film," *International Journal of Heat and Mass Transfer*, vol. 12, no. 7, pp. 791–796, 1969.

[29] S. Toda, "Study of mist cooling (1st report: Investigation of mist cooling)," *Heat Transfer - Japanese Research*, vol. 1, no. 3, pp. 39–50, 1972.

[30] S. Toda, "Study of mist cooling 2: Theory of mist cooling and its fundamental experiments," *Heat Transfer - Japanese Research*, vol. 3, no. 1, pp. 1–44, 1974.

[31] C. Bonacina, G. Comini, and S. Del Giudice, "Evaporation of atomized liquids on hot surfaces," *Letters in Heat and Mass Transfer*, vol. 2, no. 5, pp. 401–406, 1975.

[32] C. Bonacina, S. Del Giudice, and G. Comini, "Dropwise evaporation," *Journal of Heat Transfer*, vol. 101, no. 3, pp. 441–446, 1979.

[33] D. E. Tilton, "Spray cooling," Ph.D. dissertation, University of Kentucky, Lexington, KY, 1989.

[34] D. E. Tilton, L. C. Chow, M. R. Pais, and M. J. Morgan, "High-flux spray cooling in a simulated multichip module," in *28th National Heat Transfer Conference and Exhibition,*, San Diego, CA, Aug. 9-12, 1992, vol. 206, pp. 73–79.

[35] M. R. Pais, L. C. Chow, and E. T. Mahefkey, "Surface roughness and its effects on the heat transfer mechanism in spray cooling," in *Winter Annual Meeting of the ASME*, San Francisco, CA, Dec. 10-15, 1989, vol. 119, pp. 51–59.

[36] C. Cho and R. Ponzel, "Experimental study on the spray cooling of a heated solid surface," in *Proc. of the 1997 ASME International Mechanical Engineering Congress and Exposition*, Dallas, TX, Nov. 16-21 1997, vol. 244, pp. 265–272.

[37] J. E. Navedo, "Parametric effects of spray characteristics on spray cooling heat transfer," Ph.D. dissertation, University of Central Florida, Orlando, FL, 2000.

[38] L. Ortiz and J. E. Gonzalez, "Experiments on steady-state high heat fluxes using spray cooling," *Experimental Heat Transfer*, vol. 12, no. 3, pp. 215–233,

1999.

[39] K. A. Estes and I. Mudawar, "Correlation of sauter mean diameter and critical heat flux for spray cooling of small surfaces," *International Journal of Heat and Mass Transfer*, vol. 38, no. 16, pp. 2985–2996, 1995.

[40] S. Hsieh, T. Fan, and H. Tsai, "Spray cooling characteristics of water and r-134a. Part I: Nucleate boiling," *International Journal of Heat and Mass Transfer*, vol. 47, no. 26, pp. 5703–5712, 2004.

[41] M. Monde, "Critical heat flux in the saturated forced convection boiling on a heated disk with impinging droplets," *Heat Transfer - Japanese Research*, vol. 8, no. 2, pp. 54–64, 1979.

[42] J. Yang, L. C. Chow, and M. R. Pais, "Nucleate boiling heat transfer in spray cooling," *Transactions of the ASME Journal of Heat Transfer*, vol. 118, no. 3, pp. 668–671, 1996.

[43] J. Yang, "Spray cooling with an air atomizing nozzle," Ph.D. dissertation, University of Kentucky, Lexington, KY, 1993.

[44] R. Chen, D. S. Tan, K. Lin, L. C. Chow, A. R. Griffin, and D. P. Rini, "Droplet and bubble dynamics in saturated FC-72 spray cooling on a smooth surface," *Journal of Heat Transfer*, vol. 130, no. 10, pp. 101501–1 to 101501–9, 2008.

[45] A. R. Griffin, A. Vijayakumar, R. Chen, K. B. Sundaram, and L. C. Chow, "Development of a transparent heater to measure surface temperature fluctuations for pool boiling and spray cooling," in *Proc. of the ASME/JSME Thermal Engineering Summer Heat Transfer Conference,*, Vancouver, BC, Jul. 8-12 2007, vol. 2, pp. 197–201.

[46] D. P. Rini, R. Chen, and L. C. Chow, "Bubble behavior and nucleate boiling heat transfer in saturated FC-72 spray cooling," *Journal of Heat Transfer*, vol. 124, no. 1, pp. 63–72, 2002.

[47] D. P. Rini, R. Chen, and L. C. Chow, "Bubble behavior and heat transfer mechanism in FC-72 pool boiling," *Experimental Heat Transfer*, vol. 14, no. 1, pp. 27–44, 2001.

[48] D. P. Rini, "Pool boiling and spray cooling with FC-72," Ph.D. dissertation, University of Central Florida, Orlando, FL, 2000.

[49] B. Horacek, K. T. Kiger, and J. Kim, "Single nozzle spray cooling heat transfer mechanisms," *International Journal of Heat and Mass Transfer*, vol. 48, no. 8, pp. 1425–1438, 2005.

[50] A. G. Pautsch and T. A. Shedd, "Spray impingement cooling with single- and multiple-nozzle arrays. Part I: Heat transfer data using FC-72," *International Journal of Heat and Mass Transfer*, vol. 48, no. 15, pp. 3167–3175, 2005.

[51] A. G. Pautsch and T. A. Shedd, "Adiabatic and diabatic measurements of the liquid film thickness during spray cooling with FC-72," *International Journal of Heat and Mass Transfer*, vol. 49, no. 15-16, pp. 2610–2618, 2006.

[52] A. Pautsch, "Mass and energy transport phenomena in the thin film of spray cooling systems," Ph.D. dissertation, University of Wisconsin-Madison, Madison, WI, 2007.

[53] L. H. J. Wachters, L. Smulders, J. R. Vermeulen, and H. C. Kleiweg, "Heat transfer from hot wall to impinging mist droplets in spheroidal state," *Chemical Engineering Science*, vol. 21, no. 12, pp. 1231–1238, 1966.

[54] I. Michiyoshi and K. Makino, "Heat transfer characteristics of evaporation of a liquid droplet on heated surfaces," *International Journal of Heat and Mass Transfer*, vol. 21, no. 5, pp. 605–613, 1978.

[55] W. J. Yang, "Theory on vaporization and combustion of liquid drops of pure substances and binary mixtures on heated surfaces," Tech. Rep., Institute of Space and Aeronautical Science, University of Tokyo, Report, 535, 423-455, 1975.

[56] P. J. Halvorson, R. J. Carson, S. M. Jeter, and S. Abdel-Khalik, "Critical heat flux limits for a heated surface impacted by a stream of liquid droplets," *Journal of Heat Transfer*, vol. 116, no. 3, pp. 679–685, 1994.

[57] P. J. Halvorson, "On the heat transfer characteristics of spray cooling," Ph.D. dissertation, Georgia Institute of Technology, Atlanta, GA, 1993.

[58] M. L. Sawyer, S. M. Jeter, and S. Abdel-Khalik, "Critical heat flux correlation for droplet impact cooling," *International Journal of Heat and Mass Transfer*, vol. 40, no. 9, pp. 2123–2131, 1997.

[59] W. M. Healy, P. J. Halvorson, J. G. Hartley, and S. Abdel-Khalik, "Critical heat flux correlation for droplet impact cooling at low weber numbers and various ambient pressures," *International Journal of Heat and Mass Transfer*, vol. 41, no. 6-7, pp. 975–978, 1998.

[60] R. J. Sheffield, "High heat flux spray cooling," Ph.D. dissertation, Georgia Institute of Techology, Atlanta, GA, 1994.

[61] S. M. Sellers and W. Z. Black, "Boiling heat transfer rates for small precisely placed water droplets on a heated horizontal plate," *Journal of Heat Transfer*,

vol. 130, no. 5, 2008.

[62] S. M. Sellers, "Heat transfer resulting from the evaporation of liquid droplets on a horizontal heated surface," Ph.D. dissertation, Georgia Institute of Technology, Atlanta, GA, 2000.

[63] A. L. N. Moreira, A. S. Moita, and M. R. O. Panao, "Advances and challenges in explaining fuel spray impingement: How much of single droplet impact research is useful?," *Progress in Energy and Combustion Science*, vol. 36, no. 5, pp. 554–580, 2010.

[64] G. E. Cossali, M. Marengo, and M. Santini, "Single-drop empirical models for spray impact on solid walls: A review," *Atomization and Sprays*, vol. 15, no. 6, pp. 699–736, 2005.

[65] C. X. Bai and A. D. Gosman, "Development of a methodology for spray impingement simulation," in *SAE International Congress and Exposition,*, Detroit, MI, Feb. 27 - Mar. 2, 1995, vol. SAE Tech Paper 950283.

[66] R. Rioboo, C. Tropea, and M. Marengo, "Outcomes from a drop impact on solid surfaces," *Atomization and Sprays*, vol. 11, no. 2, pp. 155–165, 2001.

[67] A. S. Moita and A. L. N. Moreira, "Drop impacts onto cold and heated rigid surfaces: Morphological comparisons, disintegration limits and secondary atomization," *International Journal of Heat and Fluid Flow*, vol. 28, no. 4, pp. 735–52, 2007.

[68] M. Rieber and A. Frohn, "A numerical study on the mechanism of splashing," *International Journal of Heat and Fluid Flow*, vol. 20, no. 5, pp. 455–461, 1999.

[69] M. F. Trujillo and C. F. Lee, "Modeling crown formation due to the splashing of a droplet," *Physics of Fluids*, vol. 13, no. 9, pp. 2503–16, 2001.

[70] C. D. Stow and M. G. Hadfield, "An experimental investigation of fluid flow resulting from the impact of a water drop with an unyielding dry surface," *Proceedings of the Royal Society of London, Series A (Mathematical and Physical Sciences)*, vol. 373, no. 1755, pp. 419–41, 1980.

[71] C. Mundo, M. Sommerfeld, and C. Tropea, "Droplet-wall collisions: Experimental studies of the deformation and breakup process," *International Journal of Multiphase Flow*, vol. 21, no. 2, pp. 151–173, 1995.

[72] G. E. Cossali, A. Coghe, and M. Marengo, "Impact of a single drop on a wetted solid surface," *Experiments in Fluids*, vol. 22, no. 6, pp. 463–472, 1997.

[73] I. V. Roisman, K. Horvat, and C. Tropea, "Spray impact: Rim transverse instability initiating fingering and splash, and description of a secondary spray," *Physics of Fluids*, vol. 18, no. 10, pp. 102104–1 to 102104–19, 2006.

[74] C. Tropea and M. Marengo, "Impact of drops on walls and films," *Multiphase Science and Technology*, vol. 11, no. 1, pp. 19–36, 1999.

[75] S. Chandra and C. T. Avedisian, "On the collision of a droplet with a solid surface," *Proc. of the Royal Society of London, Series A (Mathematical and Physical Sciences)*, vol. 432, no. 1884, pp. 13–41, Aug. 1991.

[76] D. Fardad and N. Ladommatos, "Evaporation of hydrocarbon compounds, including gasoline and diesel fuel, on heated metal surfaces," *Proc. of the Institution of Mechanical Engineers.Part D, Journal of Automobile Engineering*, vol. 213, no. D6, pp. 625–645, 1999.

[77] M. H. Shi, "Dynamic behavior and heat transfer of a liquid droplet impinging on a solid surface," *Experimental Thermal and Fluid Science*, vol. 6, no. 2, pp. 202–207, 1993.

[78] S. L. Manzello and J. C. Yang, "An experimental study of high weber number impact of methoxy-nonafluorobutane c4f9och3 (hfe-7100) and n-heptane droplets on a heated solid surface," *International Journal of Heat and Mass Transfer*, vol. 45, no. 19, pp. 3961–3971, 2002.

[79] J. D. Bernardin and I. Mudawar, "The leidenfrost point: Experimental study and assessment of existing models," *Journal of Heat Transfer*, vol. 121, no. 4, pp. 894, 1999.

[80] B. S. Gottfried, C. J. Lee, and K. J. Bell, "The leidenfrost phenomenon: film boiling of liquid droplets on a flat plate," *International Journal of Heat and Mass Transfer*, vol. 9, no. 11, pp. 1167–1188, 1966.

[81] K. Makino and I. Michiyoshi, "Effects of the initial size of water droplet on its evaporation on heated surfaces," *International Journal of Heat and Mass Transfer*, vol. 22, no. 6, pp. 979–81, 1979.

[82] B. M. Patel and K. J. Bell, "Leidenfrost phenomenon for extended liquid masses," *Chemical Engineering Progress Symposium Series*, vol. 62, no. 64, pp. 62–71, 1966.

[83] S. Nishio and M. Hirata, "Direct contact phenomenon between a liquid droplet and high temperature solid surface," in *Proc. of the Sixth International Heat Transfer Conference*, Washington DC., Aug. 7-11, 1978, vol. I, pp. 245–50.

[84] G. P. Celata, M. Cumo, A. Mariani, and G. Zummo, "Visualization of the

impact of water drops on a hot surface: Effect of drop velocity and surface inclination," *Heat and Mass Transfer/Waerme- und Stoffuebertragung*, vol. 42, no. 10, pp. 885–890, 2006.

[85] S.-C. Yao and K. Y. Cai, "Dynamics and leidenfrost temperature of drops impacting on a hot surface at small angles," *Experimental Thermal and Fluid Science*, vol. 1, no. 4, pp. 363–371, 1988.

[86] V. G. Labeish, "Thermohydrodynamic study of a drop impact against a heated surface," *Experimental Thermal and Fluid Science*, vol. 8, no. 3, pp. 181–194, 1994.

[87] H. Chaves, A. M. Kubitzek, and F. Obermeier, "Dynamic processes occurring during the spreading of thin liquid films produced by drop impact on hot walls," *International Journal of Heat and Fluid Flow*, vol. 20, no. 5, pp. 470–476, 1999.

[88] J. D. Bernardin, C. J. Stebbins, and I. Mudawar, "Effects of surface roughness on water droplet impact history and heat transfer regimes," *International Journal of Heat and Mass Transfer*, vol. 40, no. 1, pp. 73–88, 1997.

[89] J. D. Bernardin, C. J. Stebbins, and I. Mudawar, "Mapping of impact and heat transfer regimes of water drops impinging on a polished surface," *International Journal of Heat and Mass Transfer*, vol. 40, no. 2, pp. 247–267, 1997.

[90] M. Rein, *Interactions between drops and hot surfaces*, pp. 185–217, New York, Springer, 2002.

[91] R.-H. Chen, L. C. Chow, and J. E. Navedo, "Effects of spray characteristics on critical heat flux in subcooled water spray cooling," *International Journal of Heat and Mass Transfer*, vol. 45, no. 19, pp. 4033–43, 2002.

[92] A. G. Pautsch, T. A. Shedd, and G. F. Nellis, "Thickness measurements of the thin film in spray evaporative cooling," in *Proc. of Ninth Intersociety Conference on Thermal and Thermomechanical Phenomena in Electronic Systems*, Las Vegas, NV, 2004, vol. 1, pp. 70–76.

[93] T. A. Shedd and T. A. Newell, "Automated optical liquid film thickness measurement method," *Review of Scientific Instruments*, vol. 69, no. 12, pp. 4205–4205, 1998.

[94] H. C. Pumphrey and P. A. Elmore, "Entrainment of bubbles by drop impacts," *Journal of Fluid Mechanics*, vol. 220, pp. 539–567, 1990.

[95] D. Gstoehl, J. F. Roques, P. Crisinel, and J. R. Thome, "Measurement of falling film thickness around a horizontal tube using a laser measurement technique," *Heat Transfer Engineering*, vol. 25, no. 8, pp. 28–34, 2004.

[96] R. G. Driggers, *Encyclopedia of Optical Engineering*, Marcel Dekker, New York, 2003.

[97] A. R. Jha, *Infrared Technology : Applications to Electro-optics, Photonic Devices, and Sensors*, New York, Wiley, 2000.

[98] "Standard test methods for measuring and compensating for emissivity using infrared imaging radiometers," ASTM Standard E1933 - 99a(2005)e1, 2005.

[99] S. J. Kline and F. A. McClintock, "Describing uncertainties in singlesample experiments," *Mechanical Engineering*, vol. 75, no. 1, pp. 38, 1953.

[100] N. R. Lindblad and J. M. Schneider, "Production of uniform-sized liquid droplets," *Journal of Scientific Instruments*, vol. 42, no. 8, pp. 635–638, 1965.

[101] J. M. Schneider and C. D. Hendricks, "Source of uniform-seized liquid droplets," *Review of Scientific Instruments*, vol. 35, no. 10, pp. 1349–1350, 1964.

[102] J. A. Mulholland, R. K. Srivastava, and J. O. L. Wendt, "Influence of droplet spacing on drag coefficient in nonevaporating, monodispersive streams," *AIAA Journal*, vol. 26, no. 10, pp. 1231–1237, 1988.

[103] I. V. Roisman and C. Tropea, "Fluctuating flow in a liquid layer and secondary spray created by an impacting spray," *International Journal of Multiphase Flow*, vol. 31, no. 2, pp. 179–200, 2005.

[104] W. Samenfink, A. Elsacer, K. Dullenkopf, and S. Wittig, "Droplet interaction with shear-driven liquid films: Analysis of deposition and secondary droplet characteristics," *International Journal of Heat and Fluid Flow*, vol. 20, no. 5, pp. 462–469, 1999.

[105] X. Liu, J. H. Lienhard V, and J. S. Lombara, "Convective heat transfer by impingement of circular liquid jets," *Journal of Heat Transfer*, vol. 113, no. 3, pp. 571–582, 1991.

[106] C. F. Ma, "Analytical study on impingement heat transfer with single-phase free-surface circular liquid jets," *Journal of Thermal Science*, vol. 5, no. 4, pp. 271, 1996.

[107] E. J. WATSON, "The radial spread of a liquid jet over a horizontal plane," *Journal of Fluid Mechanics*, vol. 20, no. 3, pp. 481–499, 1964.

[108] Atul Sharan, "Jet-disc boiling : burnout predictions and application to solar receivers," M.S. thesis, University of Houston, Houston, TX, 1984.

[109] S. Freund and S. Kabelac, "Measurement of local convective heat transfer coefficients with temperature oscillation IR thermography and radiant heating," in *Proc. of ASME Summer Heat Transfer Conference*, San Francisco, CA, July 17-22, 2005, vol. 1, pp. 663–669.

[110] S. Freund, A. G. Pautsch, T. A. Shedd, and S. Kabelac, "Local heat transfer coefficients in spray cooling systems measured with temperature oscillation IR thermography," *International Journal of Heat and Mass Transfer*, vol. 50, no. 9-10, pp. 1953–1962, 2007.

APPENDIX A

HFE 7100 FLUID PROPERTIES

Table XV.: HFE-7100 physical properties specified at 25 ℃

Properties	Value
Molecular Weight, g/mol	250.0
Flash Point	None
Freeze Point, ℃	-135
Boiling Point, ℃	61
Critical Temperature, ℃	195.3
Critical Pressure, MPa	2.23
Critical Density, kg/m^3 (estimated)	555
Heat of Vaporization @ B.P., kJ/kg	111.6
Surface Tension, dynes/cm	13.6
Solubility of Water in Fluid, ppm by weight	95
Solubility of Air in Fluid, volume air @ 1 atm per volume fluid	53%
Typical Dielectric Strength (0.1 in. gap), kV (RMS).[1]	28
Dielectric Constant, 100 Hz - 10 MHz	7.39
Volume resistivity, $ohm - cm$	$3.29x10^9$

[1]The dielectric strength of virgin HFE-7100 fluid is specified as 20 kV minimum. As dielectric properties can be degraded by the presence of dissolved plasticizer, particulate or water, when dielectric properties are critical, careful attention should be paid to material compatibility and moisture content.

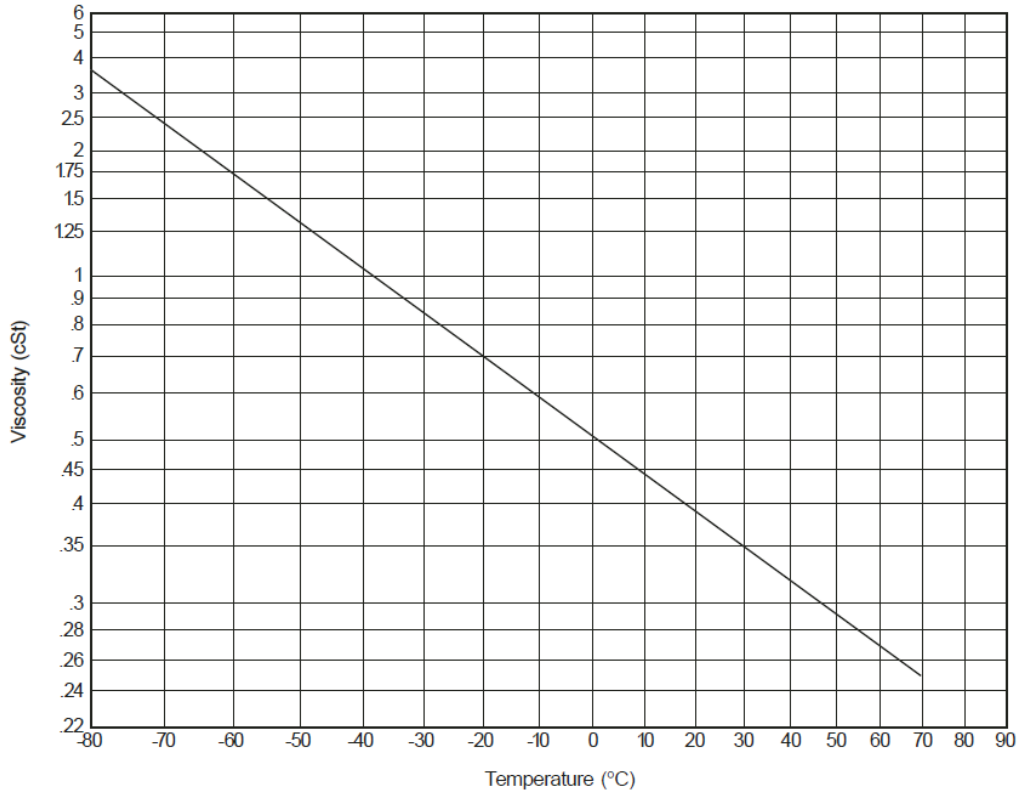

Fig. 53.: Kinematic viscosity of HFE-7100

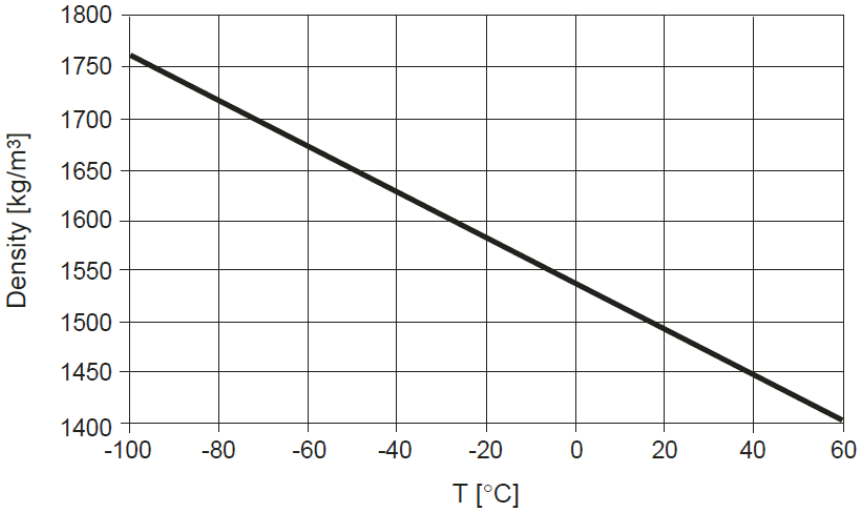

Fig. 54.: Density of HFE-7100

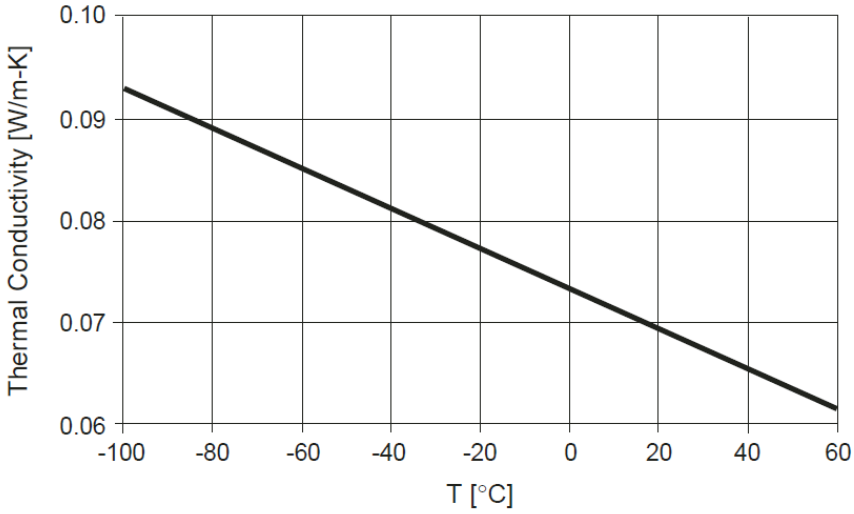

Fig. 55.: Thermal conductivity of HFE-7100

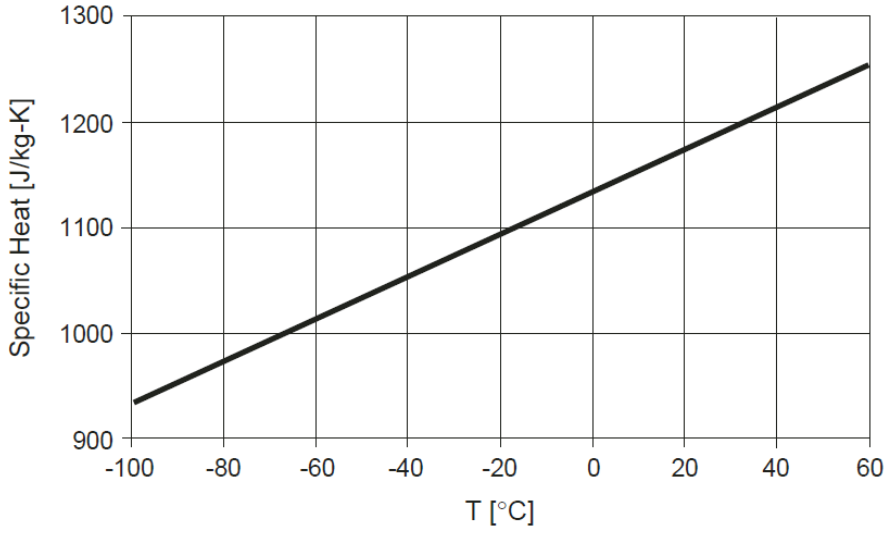

Fig. 56.: Specific heat of HFE-7100

APPENDIX B

SINGLE STREAM CASES

Table XVI.: Results single stream cases

Flow rate ml/hr	Frequency $Hz.$	Droplet Diameter μm	Droplet Velocity m/s	Weber	Strouhal	CHF (W/cm^2)
120	2,730	285.7	1.81	96.5	0.454	25.7
120	3,400	265.5	1.81	89.7	0.525	26.8
120	4,100	249.5	1.80	84.3	0.595	26.8
120	4,720	238.0	1.79	80.4	0.654	26.4
150	3,335	287.9	2.31	165	0.430	29
150	4,300	264.5	2.31	151.6	0.508	30.2
150	5,300	246.7	2.30	141.4	0.584	30.2
150	6,200	232.9	2.29	134.2	0.649	28.8
180	4,300	281.1	2.80	242	0.441	37.6
180	5,300	262.2	2.80	225.7	0.508	38.2
180	6,300	247.5	2.79	213	0.568	36.8
180	7,500	233.5	2.79	201	0.639	38.1
210	6,130	262.9	3.29	315.7	0.498	42.1
210	7,000	251.5	3.28	302	0.544	40.7
210	8,000	240.6	3.28	288.9	0.594	42.2
210	8,700	233.9	3.28	281	0.628	41.6
250	6,850	268.5	3.93	466	0.472	46.7
250	8,000	255.0	3.93	442.5	0.524	49.4
250	9,000	245.2	3.93	425	0.567	45.3
250	10,900	230.0	3.93	399	0.644	47.3
280	7,750	267.6	4.42	588	0.473	46.4
280	10,000	245.8	4.41	540	0.561	43.3
280	12,000	231.3	4.41	508.3	0.634	47.1
280	13,500	222.4	4.41	489	0.685	44.8

APPENDIX C

TRIPLE STREAM CASES

Table XVII.: Results triple stream cases

Flow ml/hr	Frequency Hz	Droplet Diameter μm	Droplet Velocity m/s	Weber	Strouhal	Spacing μm	CHF W/cm^2
540	7,200	236.7	2.79	204	0.621	400	48
540	8,700	222.2	2.78	190	0.705	400	47.3
540	7,200	236.7	2.79	204	0.621	800	53.9
540	8,700	222.2	2.78	190	0.705	800	50.5
540	7,200	236.7	2.79	204	0.621	1,500	67
540	8,700	222.2	2.78	190	0.705	1,500	66.1
750	8,000	255.0	3.93	442.5	0.524	400	58.3
750	11,000	229.3	3.92	398	0.648	400	55.8
750	8,000	255.0	3.93	442.5	0.524	800	65
750	11,000	229.3	3.92	398	0.648	800	65.5
750	8,000	255.0	3.93	442.5	0.524	1,500	81.6
750	11,000	229.3	3.92	398	0.648	1,500	80.2

VITA

Name: Guillermo Enrique Soriano

Address: Thompson Hall
MS: 3367 TAMU
College Station, Texas 77843-3367

Email Address: gsoriano@tamu.edu

Education: B.S., Mechanical Engineering, Escuela Superior Politecnica del Litoral, Guayaquil-Ecuador, 2000

M.S., Industrial Engineering, Georgia Institute of Technology, 2004

Ph.D., Mechanical Engineering, Texas A&M University, 2011

The typist for this dissertation was Guillermo Enrique Soriano.